Evaluation of Roadway Worms/Distortions

Final Report

April 2021

Prepared for:
Florida Department of Transportation
Central Procurement Office
Attn: Jason Tuck
605 Suwannee Street, Mail Station 20
Tallahassee, Florida 32399-0450

Prepared by:
Applied Research Associates, Inc.
430 W 5th Street, Suite #700
Panama City, Florida 32401
850-914-3188 / 850-914-3189 Fax

Authors: Aaron B. Pullen and Hyung S. Lee, Ph.D., P.E.

Contract No. BE491

Disclaimer

The opinions, findings, and conclusions expressed in this publication are those of the authors and not necessarily those of the State of Florida Department of Transportation.

SI (MODERN METRIC) Conversion Factors

SYMBOL	WHEN YOU KNOW	MULTIPLY BY	TO FIND	SYMBOL
Length				
in	inches	25.4	millimeters	mm
ft	feet	0.305	meters	m
yd	yards	0.914	meters	m
mi	miles	1.61	kilometers	km
Area				
in^2	square inches	645.2	square millimeters	mm^2
ft^2	square feet	0.093	square meters	m^2
yd^2	square yard	0.836	square meters	m^2
ac	acres	0.405	hectares	ha
Volume				
fl oz	fluid ounces	29.57	milliliters	mL
gal	gallons	3.785	liters	L
ft^3	cubic feet	0.028	cubic meters	m^3
yd^3	cubic yards	0.765	cubic meters	m^3
NOTE: volumes greater than 1000 L shall be shown in m^3				
Mass				
oz	ounces	28.35	grams	g
lb	pounds	0.454	kilograms	kg
Temperature (exact degrees)				
ºF	Fahrenheit	5 (F-32)/9	ºF	Fahrenheit
or (F-32)/1.8	Celsius	ºC	or (F-32)/1.8	Celsius
Force and Pressure or Stress				
lbf	pound-force	4.45	newtons	N
lbf/in^2	pound-force per square inch	6.89	kilopascals	kPa

Technical Report Documentation Page

1. Report No.	2. Government Accession No.	3. Recipient's Catalog No.

4. Title and Subtitle	5. Report Date
Evaluation of Roadway Worms/Distortions	January 2021
	6. Performing Organization Code
7. Author(s)	8. Performing Organization Report No.
Aaron B. Pullen and Hyung S. Lee, Ph.D., P.E.	
9. Performing Organization Name and Address	10. Work Unit No. (TRAIS)
Applied Research Associates, Inc. 430 W 5th Street, Suite #700 Panama City, Florida 32401	11. Contract or Grant No. BE491
12. Sponsoring Agency Name and Address	13. Type of Report and Period Covered
Florida Department of Transportation 605 Suwannee Street, MS 30 Tallahassee, FL 32399	Draft Final Report November 2017 to January 2021
	14. Sponsoring Agency Code

15. Supplementary Notes

16. Abstract

The Florida Department of Transportation (FDOT) has experienced roadway worms, or blistering of flexible pavements, for several decades. A literature review indicated that the distress (also referred to as ripples and distortions) generally occurs due to moisture or other gas-forming substances trapped in between two layers of asphalt concrete (AC), which may vaporize and expand in volume under hot environments. Forensic investigations were conducted on five Florida roadway sections that exhibited the distress to identify the causes and contributing factors of roadway worms and to assess the impact of the worm distress on pavement performance. Field and laboratory test results indicated worm distresses on each site are associated with deterioration due to the presence of moisture within the AC layers and at the interface of the upper two AC lifts. The deterioration was more pronounced in the dense-graded AC surface course layers and included segregation, excessive air voids, stripping, and interface debonding with underlying AC layers, as confirmed by laboratory test results. Although the modulus degradation was greater for the top lift, it was observed in both the top and the bottom lift AC. Simulation of pavement response and performance showed that the worm-distressed sections exhibit increased level of pavement response (i.e., deflections and strains) and a significant reduction in predicted pavement life (i.e., 62% to 92% reduction under top-down cracking mode). Strategies are recommended for preventing the occurrence of worm distress and rehabilitating pavements with worm distress. The findings of this study do not support any recommended design changes.

17. Key Word	18. Distribution Statement
Asphalt Concrete (AC), roadway worms, blisters, distortions, delamination	No restrictions.

19. Security Classif. (of this report)	20. Security Classif. (of this page)	21. No. of Pages	22. Price
Unclassified.	Unclassified.	133	

Form DOT F 1700.7 (8-72) Reproduction of completed page authorized

Evaluation of Roadway Worms/Distortions Final Report

Executive Summary

FDOT has experienced roadway worms, which become visible at the asphalt concrete (AC) pavement surface as small bubbles or major bulges, for several decades. Several past studies indicated that the roadway worms (also referred to as ripples and blisters) generally occur when moisture or other gas-forming substances are trapped between the two asphalt layers. The subject moisture or gas may vaporize and expand in volume under a hot environment. Nevertheless, no literature was identified that examined the effect of roadway worms on cracking and rutting pavement performance and service life.

The primary objectives of this study were to identify the causes and contributing factors of roadway worms and to assess the impact of the worm distress on pavement performance. To accomplish these objectives, field and laboratory investigations were conducted on five Florida roadway sections that exhibited the particular distress.

The subject investigations were conducted on roadway projects that exhibited both (1) segments of worm distress and (2) segments without worm distress. In each case, roadway sections were continuous projects of the same construction. This approach permitted ideal pairs of test and control sections for comparison in order to identify the mechanism(s) causing worm distress.

Careful observation of the field cores from each site indicated that worm distress is associated with internal deterioration within the AC layers and at the interface of two AC lifts. The deterioration was more pronounced in the dense-graded AC surface course and included segregation, excessive air voids, stripping, and interface debonding with underlying AC layers, as confirmed by laboratory test results. More specifically, laboratory shear test results conducted on field-retrieved cores indicated that the worm sections generally exhibited lower bond strength, although the strength and the degree of bond deterioration varied substantially between projects and within each project. Furthermore, many of the field cores (41%) tested for bond shear did not produce meaningful results due to crumbling and failing within the AC mixture itself (rather than the interface), indicating severe loss of durability, stiffness, and strength of the AC. Significant degradation in AC modulus in worm-distressed areas was confirmed by the backcalculated dynamic modulus from field falling weight deflectometer (FWD) tests as well as laboratory resilient modulus test results.

The field and laboratory investigations suggested that the causes (and contributing factors) of the worm distress may be speculated as the following:

1. Moisture entering the AC layer during construction and getting trapped within the material and/or at the layer interface. The trapped moisture expands due to heat buildup within the AC layer, resulting in severe bulging, stripping, and an increase in air voids of the AC layer (which may have once had adequate air void content). The source of moisture may include the following:
    a. Paving on top of a wet pavement surface (although not completely wet or saturated). The existing moisture may get trapped within or in between impervious AC layers.
    b. Excess moisture from the compaction roller trapped within the AC layer being compacted.

   c. The use of excessively wet aggregate stockpiles or insufficient drying procedures during the production of hot-mix asphalt.

2. Intrusion through cracks at the pavement surface, which then gets trapped due to further compaction of AC by the driving traffic (more pronounced for mixtures having high air void content or segregation). Worm distress was noted in FDOT survey records for three of the five projects; the occurrences were first observed 7 to 8 years after construction.
3. Constructing on top of an AC layer with high air voids or a layer that has already experienced worm distress, as evidenced by the excessive air void content observed on many of the AC lifts directly above the unbound layer.
   a. The increase in temperature within the bottom AC lift may not be as significant as the layer that is exposed to the sun. As such, it is speculated that the higher air voids observed in these lower layers may be due to the worms that occurred before they were overlaid by another lift of AC. The moisture trapped between the AC and unbound base may cause worms.
   b. Once this layer has experienced worms and/or was constructed with higher air voids, it provides more room to store moisture prior to being overlaid.

Regardless of the cause, the consequences of worm distresses can be severe. Although the degradation in worm-distressed pavement AC modulus was more pronounced for the top lift, it was observed in both the top and the bottom AC lifts, with the modulus reduction ranging from 16% to 72% (based on the dynamic modulus obtained at 10 Hz and at 50ºF). In addition, simulation of pavement response and performance showed that the worm-distressed sections exhibited an increased level of pavement response (i.e., deflections and strains). The increase in pavement response, combined with reduced modulus, resulted in a significant reduction in predicted pavement life (i.e., 62% to 92% reduction for the top-down cracking mode of distress).

Table of Contents

1. INTRODUCTION 1
1.1. Background 1
1.2. Research Objectives 1
1.3. Scope 2
2. LITERATURE REVIEW 3
2.1. Overview of Pavement Worms 3
2.1.1. Moisture Vapor Pressure 3
2.1.2. Presence of Soluble Salts 6
2.1.3. Use of Unaged Steel Slag Aggregates 6
2.1.4. Microbial Action 6
2.1.5. Miscellaneous Factors 7
2.2. The Effect of Worm Distress on Pavement Performance 7
2.3. Methods for Assessing Bond between Asphalt Layers 7
3. METHODS AND PROCEDURES 12
3.1. Test Sites 12
3.1.1. Site 1 – FL SR 79 15
3.1.2. Site 2 – FL SR 26 17
3.1.3. Site 3 – FL SR 24 19
3.1.4. Site 4 – FL US 17 20
3.1.5. Site 5 – FL SR 20 22
3.2. Field Test Program 23
3.2.1. Pavement Condition Index (PCI) 25
3.2.2. Falling Weight Deflectometer (FWD) 27
3.2.3. Ground Penetrating Radar (GPR) 27
3.2.4. Portable Seismic Pavement Analyzer (PSPA) 28
3.2.5. Core Samples of AC Pavement 28
3.2.6. Dynamic Cone Penetrometer (DCP) 29
3.2.7. Bulk Samples of Base Aggregate and Subgrade 30
3.3. Laboratory Test Program 30
4. RESULTS AND DISCUSSION 32
4.1. Field Test Results 32
4.1.1. Ground Penetrating Radar (GPR) 32
4.1.2. Pavement Condition Index (PCI) 37
4.1.3. Falling Weight Deflectometer (FWD) 42
4.1.4. Dynamic Cone Penetrometer (DCP) 63
4.1.5. Portable Seismic Pavement Analyzer (PSPA) 64
4.2. AC Field Core Laboratory Test Results 65

4.2.1. Observation of Field Cores 65
4.2.2. Gradation and Binder Content 75
4.2.3. Core Density 81
4.2.4. Permeability 84
4.2.5. Interlayer Bond Strength 86
4.2.6. Indirect Tensile Resilient Modulus Test 98
4.3. Aggregate Base Materials 103
4.4. Subgrade Materials 106
4.5. Embankment Materials 108
4.6. Pavement Service Life Analysis 109
5. SUMMARY OF FINDINGS 118
6. CONCLUSIONS AND RECOMMENDATIONS 120
6.1. Determine Contributing Cause(s) for Roadway Worms 120
6.2. Identify the Impact on Pavement Lifespan of Roadway Worms 120
6.3. Develop Rehabilitation Strategies to Prevent Roadway Worms from Occurring 121
7. REFERENCES 122

List of Figures

Figure 2-1. Cause of the Blistering Phenomenon 4
Figure 2-2. Tensile Pull-Off Tester 8
Figure 2-3. Bond Strength Shear Test Fixture 9
Figure 2-4. Equipment Components of PSPA [23] 10
Figure 2-5. PSPA Dispersion Curves [17] 10
Figure 2-6. Steel Wheel versus Pneumatic Breakdown Roller on IH35-Laredo [26] 11
Figure 3-1. Roadway Worm Test Site Locations 13
Figure 3-2. Test Site Pavement Cross-Section Design 15
Figure 3-3. SR 79 Roadway Overview 16
Figure 3-4. SR 79 Worm Distress 17
Figure 3-5. SR 26 Roadway Overview 18
Figure 3-6. SR 26 Worm Distress 18
Figure 3-7. SR 24 Roadway Overview 19
Figure 3-8. SR 24 Worm Distress 20
Figure 3-9. US 17 Roadway Overview 21
Figure 3-10. US 17 Worm Distress 21
Figure 3-11. SR 20 Roadway Overview 22
Figure 3-12. SR 20 Worm Distress 23
Figure 3-13. Sample Field Data Collection Map (Site 1 – SR 79) 24
Figure 3-14. PCI Cracking Survey Process 25
Figure 3-15. PCI Rutting Survey Process 25
Figure 3-16. Ground-Coupled GPR 27
Figure 3-17. GSSI PaveScan RMD 27
Figure 3-18. Vehicle-Based Air-Coupled GPR 27
Figure 3-19. PSPA Test 28
Figure 3-20. Partial-Depth Wet-Coring and Vacuuming of 12-in Diameter AC Samples Prior to Dry Coring 29
Figure 3-21. Sampling Base, Subgrade, and Embankment Materials 29
Figure 3-22. Manual DCP Test 30
Figure 3-23. Automated DCP Test 30

Figure 4-1. Dielectric Profiles from SR 24 (a) Control and (b) Worm Sections 33
Figure 4-2. Dielectric Profiles from SR 26 (a) Control and (b) Worm Sections 34
Figure 4-3. Dielectric Profiles from US 17 (a) Control and (b) Worm Sections 35
Figure 4-4. Dielectric Profiles from SR 20 (a) Control and (b) Worm Sections 36
Figure 4-5. Dielectric Summaries: (a) Mean and (b) COV 37
Figure 4-6. Overall PCI 38
Figure 4-7. Worm Section Distress Occurrence 39
Figure 4-8. Control Section Distress Occurrence 39
Figure 4-9. Area Weighted L&T Cracking 40
Figure 4-10. Area Weighted Block Cracking 41
Figure 4-11. Area Weighted Alligator Cracking 41
Figure 4-12. Area Weighted Rutting 42
Figure 4-13. (a) Measured and (b) ViscoWave Backcalculated FWD Time Histories from SR 20 Worm Section 44
Figure 4-14. FWD Deflections from SR 79 Control Section 45
Figure 4-15. FWD Deflections from SR 79 Worm Section No. 1 45
Figure 4-16. FWD Deflections from SR 79 Worm Section No. 2 46
Figure 4-17. Average FWD Deflection Basins from SR 79 47
Figure 4-18. FWD Deflections from SR 26 Control Section 48
Figure 4-19. FWD Deflections from SR 26 Worm Section 48
Figure 4-20. Average FWD Deflection Basins from SR 26 49
Figure 4-21. Backcalculated Dynamic Modulus Master Curves for SR 26 Top Lift AC Layer 50
Figure 4-22. Backcalculated Dynamic Modulus Master Curves for SR 26 Bottom Lift AC Layer 50
Figure 4-23. FWD Deflections from SR 24 Control Section 51
Figure 4-24. FWD Deflections from SR 24 Worm Section 51
Figure 4-25. Average FWD Deflection Basins from SR 24 52
Figure 4-26. Backcalculated Dynamic Modulus Master Curves for SR 24 Top Lift AC Layer 53
Figure 4-27. Backcalculated Dynamic Modulus Master Curves for SR 24 Bottom Lift AC Layer 53
Figure 4-28. FWD Deflections from US 17 Control Section 54

Figure 4-29. FWD Deflections from US 17 Worm Section 54
Figure 4-30. Average FWD Deflection Basins from US 17 55
Figure 4-31. Backcalculated Dynamic Modulus Master Curves for US 17 Top Lift AC Layer 56
Figure 4-32. Backcalculated Dynamic Modulus Master Curves for US 17 Bottom Lift AC Layer 56
Figure 4-33. FWD Deflections from SR 20 Control Section 57
Figure 4-34. FWD Deflections from SR 20 Worm Section 57
Figure 4-35. Average FWD Deflection Basins from SR 20 58
Figure 4-36. Backcalculated Dynamic Modulus Master Curves for SR 20 Top Lift AC Layer 59
Figure 4-37. Backcalculated Dynamic Modulus Master Curves for SR 20 Bottom Lift AC Layer 59
Figure 4-38. FWD Backcalculated Dynamic Modulus of Top Lift AC at 50ºF and 10 Hz 60
Figure 4-39. FWD Backcalculated Dynamic Modulus of Bottom Lift AC at 50ºF and 10 Hz 61
Figure 4-40. FWD Backcalculated Interface Bond Modulus 61
Figure 4-41. FWD Backcalculated Base Modulus 62
Figure 4-42. FWD Backcalculated Subgrade Modulus 62
Figure 4-43. Average Base CBR from DCP 63
Figure 4-44. Average Stabilized Subgrade CBR from DCP 63
Figure 4-45. Average Embankment CBR from DCP 64
Figure 4-46. AC PSPA Moduli 65
Figure 4-47. SR 79 MP 0.427 Worm Section Core – Structural AC Layer Delamination 66
Figure 4-48. SR 79 MP 0.391 Control Section Core – Typical Core 66
Figure 4-49. SR 79 MP 0.321 Worm Section Core – Structural AC Layer Delamination and Segregation 66
Figure 4-50. SR 79 MP 0.357 Control Section – Structural AC Layer Delamination and Segregation 66
Figure 4-51. SR 79 AC Field Core Thickness 67
Figure 4-52. SR 26 MP 8.837 Worm Core Cross-Section – Stripping/Voids at Layer Interface 68
Figure 4-53. SR 26 MP 8.809 Control Core Cross-Section – Typical Core 68

Figure 4-54. SR 26 MP 8.879 Worm Section Core – Upper Layer Delamination 68
Figure 4-55. SR 26 MP 8.813 Control Core – Typical Core 68
Figure 4-56. SR 26 AC Field Core Thickness 69
Figure 4-57. SR 24 MP 31.207 Worm Core Cross Section – Paving Lane Joint with Voids at Bottom of Friction Course 70
Figure 4-58. SR 24 MP 22.473 – Typical Control Core Cross-Section 70
Figure 4-59. SR 24 Typical Worm Section Core at MP 31.185 70
Figure 4-60. SR 24 Typical Control Section Core at MP 22.489 70
Figure 4-61. SR 24 AC Field Core Thickness 71
Figure 4-62. US 17 MP 17.762 Worm Distress Cross-Section Showing Crack Pattern in Upper Structural AC Layer 72
Figure 4-63. US 17 Typical Control AC Cross-Sections at (a) 17 MP 17.740 with Partial Depth Crack and (b) MP 17.406 72
Figure 4-64. US 17 Worm Core at MP 17.795 – Layer 2 Segregation 72
Figure 4-65. US 17 Control Core at MP 17.432 – High Air Voids in All Layers 72
Figure 4-66. US 17 AC Field Core Thickness 73
Figure 4-67. SR 20 MP 2.511 Worm Section Paving Lane Joint Cross-Section Showing Large Air Voids in Both AC Layers 74
Figure 4-68. SR 20 MP 2.973 Control Section Paving Lane Joint Cross-Section Showing Top-Down Crack 74
Figure 4-69. SR 20 Worm Section Paving Lane Core with Large Air Voids at MP 2.442 74
Figure 4-70. SR 24 Typical Control Section Core at MP 2.931 74
Figure 4-71. SR 20 AC Field Core Thickness 75
Figure 4-72. AC Binder Content 76
Figure 4-73. SR 79 Layer 2 SP-9.5 Fine-Graded AC Gradations 76
Figure 4-74. SR 79 Layer 3 SP-12.5 Fine-Graded AC Gradations 77
Figure 4-75. SR 26 Layer 1 SP-12.5 Fine-Graded AC Gradations 77
Figure 4-76. SR 26 Layer 2 SP-12.5 Fine-Graded AC Gradations 78
Figure 4-77. SR 24 Layer 1 SP-12.5 mm Fine-Graded AC Gradations 78
Figure 4-78. SR 24 Layer 2 SP-12.5 mm Fine-Graded AC Gradations 79
Figure 4-79. US 17 Layer 2 SP-12.5 mm Fine-Graded AC Gradations 79
Figure 4-80. US 17 Layer 3 SP-9.5 mm Fine-Graded AC Gradations 80

Figure 4-81. SR 20 Layer 1 SP-12.5 mm Fine-Graded AC Gradations 80
Figure 4-82. SR 20 Layer 2 SP-9.5 Coarse- and Fine-Graded AC Gradations 81
Figure 4-83. SR 79 AC Field Core Air Voids 82
Figure 4-84. SR 26 AC Field Core Air Voids 82
Figure 4-85. SR 24 AC Field Core Air Voids 83
Figure 4-86. US 17 AC Field Core Air Voids 83
Figure 4-87. SR 20 AC Field Core Air Voids 84
Figure 4-88. Interlayer Bond Strength Results 87
Figure 4-89. Close-up of Air Voids at US 17 Worm Core Layer Interface 88
Figure 4-90. SR 79 Example AC Layer Interfaces 90
Figure 4-91. SR 26 Example AC Layer Interfaces 91
Figure 4-92. SR 24 Example AC Layer Interfaces 92
Figure 4-93. US 17 Control Section MP 17.403 Bond Test Failure Outside of Interface 93
Figure 4-94. US 17 Control Section MP 17.401 Bond Test Failure Outside of Interface 94
Figure 4-95. US 17 Worm Section MP 31.130 Bond Test Failure Outside of Interface 95
Figure 4-96. US 17 Worm Section MP 31.146 Bond Test Failure Outside of Interface 96
Figure 4-97. SR 20 Example AC Layer Interfaces 97
Figure 4-98. Additional Examples of Failures outside of Interface on Roadway 98
Figure 4-99. Indirect Tensile Test Setup 99
Figure 4-100. Measured and Predicted IDT Horizontal Strain for SP 12.5 at 50ºF 100
Figure 4-101. Measured and Predicted IDT Vertical Strain for SP 12.5 at 50ºF 100
Figure 4-102. Backcalculated Dynamic Modulus Values for SP 12.5 at Three Different Temperatures 101
Figure 4-103. Dynamic Modulus Master Curve for SP 12.5 at a Reference Temperature of 50ºF 102
Figure 4-104. Dynamic Modulus Master Curves for the Top Lift of SR 79 AC (SP 9.5) at a Reference Temperature of 50 ºF 102
Figure 4-105. Dynamic Modulus Master Curves for the Bottom Lift of SR 79 AC (SP 12.5) at a Reference Temperature of 50ºF 103

Figure 4-106. Average Base Thickness 104
Figure 4-107. Base Course Moisture Content Relative to OMC 104
Figure 4-108. Laboratory Base Course LBR Results 105
Figure 4-109. Laboratory Base Course Maximum Density Results 106
Figure 4-110. Average Stabilized Subgrade Thickness 107
Figure 4-111. Subgrade Moisture Content Relative to OMC 107
Figure 4-112. Laboratory Subgrade Maximum Density Results 108
Figure 4-113. Embankment Moisture Content Relative to OMC 109
Figure 4-114. Laboratory Embankment Maximum Density Results 109
Figure 4-115. Illustration of Tensile Cracks in the Debonded Surface Layer [32] 110
Figure 4-116. ViscoWave Simulated SR 24 Deflection at the Bottom of AC 112
Figure 4-117. ViscoWave Simulated SR 24 Longitudinal Strain at the Bottom of AC 112
Figure 4-118. ViscoWave Simulated SR 24 Transverse Strain at the Bottom of AC 113
Figure 4-119. ViscoWave Simulated SR 24 Vertical Strain at the Bottom of AC 113
Figure 4-120. ViscoWave Simulated SR 26 Vertical Strain at Bottom of Top Lift AC 115
Figure 4-121. ViscoWave Simulated SR 26 Transverse Strain at Bottom of Top Lift AC 115
Figure 4-122. Rut Depth Predicted for SR 26 Control Section 116
Figure 4-123. Rut Depth Predicted for SR 26 Worm Section 116

List of Tables

Table 2-1. Asphalt Blister Causes, Symptoms, and Solutions [3]..... 5
Table 3-1. Roadway Characteristics 14
Table 3-2. Roadway Sections 14
Table 3-3. PCI Distress Severity Criteria Summary 26
Table 3-4. Laboratory Tests on AC Materials..... 31
Table 3-5. Laboratory Tests on Geotechnical Materials 31
Table 4-1. PCI Distress Codes..... 39
Table 4-2. SR 79 FWD Deflection Statistics 47
Table 4-3. SR 26 FWD Deflection Statistics 49
Table 4-4. Pavement Surface Temperature during SR 26 FWD Testing 49
Table 4-5. Summary of Backcalculated Modulus from SR 26 FWD Testing..... 50
Table 4-6. SR 24 FWD Deflection Statistics 52
Table 4-7. Pavement Surface Temperature during SR 24 FWD Testing 52
Table 4-8. Summary of Backcalculated Modulus from SR 24 FWD Testing..... 53
Table 4-9. US 17 FWD Deflection Statistics 55
Table 4-10. Pavement Surface Temperature during US 17 FWD Testing 55
Table 4-11. Summary of Backcalculated Modulus from US 17 FWD Testing..... 56
Table 4-12. SR 20 FWD Deflection Statistics 58
Table 4-13. Pavement Surface Temperature during SR 20 FWD Testing 58
Table 4-14. Summary of Backcalculated Modulus from SR 20 FWD Testing..... 59
Table 4-15. SR 79 AC Permeability 84
Table 4-16. SR 26 AC Permeability 85
Table 4-17. SR 24 AC Permeability 85
Table 4-18. US 17 AC Permeability 86
Table 4-19. SR 20 AC Permeability 86
Table 4-20. AASHTO Base Classifications..... 104
Table 4-21. AASHTO Subgrade Classifications..... 107
Table 4-22. AASHTO Embankment Classifications..... 108
Table 4-23. Summary of Allowable Number of Load Repetitions (× 10^6) for Cracking 114

Table 4-24. Summary of Predicted Cracking Life Reduction..... 114
Table 4-25. Summary of Predicted Rutting Life Reduction 117

List of Acronyms and Abbreviations

AADT	annual average daily traffic
AASHTO	American Association of State Highway and Transportation Officials
AC	asphalt concrete
ARA	Applied Research Associates
CBR	California bearing ratio
COV	coefficient of variation
DCP	dynamic cone penetrometer
DGA	dense graded asphalt
FDOT	Florida Department of Transportation
FWD	falling weight deflectometer
GPR	ground penetrating radar
IDT	indirect tensile test
ISS	interlayer shear strength
JULEA	Jacob Ozan Layered Elastic Analysis
L&T	longitudinal and transverse
LBR	lime rock bearing ratio
MEPDG	Mechanistic-Empirical Pavement Design Guide
NDT	nondestructive test
NMAS	nominal maximum aggregate size
OGFC	open-graded friction course
OMC	optimum moisture content
PCC	Portland cement concrete
PCI	pavement condition index
PCS	primary control sieve
PSPA	Portable Seismic Pavement Analyzer
SMO	State Materials Office
TTI	Texas Transportation Institute
USW	ultrasonic surface wave
VMA	voids in the mineral aggregate

1. INTRODUCTION

Blisters on asphalt concrete (AC) pavement surfaces, also referred to as ripples, roadway worms, or distortions, have been recognized for several decades [1]. Blisters generally appear on dense-graded AC surfaces during the hot summer season. They may occur on thin AC overlays over existing AC and portland cement concrete (PCC) and on new AC pavement surfaces.

Blisters are caused by moisture or other gas-forming substances trapped at layer interfaces in AC pavements, typically below a thin surface layer. When this trapped substance is heated, it may vaporize and expand in volume and, under sufficient pressure, cause the AC surface to rise and buckle. Although this mechanism is simple in theory, the phenomenon of AC blisters is rather complex and unpredictable. It can be influenced by a variety of factors, such as pavement type, underlying layer characteristics, mix type and other physical properties of the AC, laydown operation, climatic conditions, etc. [1].

The consequences of AC blisters may be severe. Blisters may result in development of other distresses such as corrugation, shoving, slippage cracking, and tensile cracking. Many literature sources define these and other types of distresses typically found in flexible pavements. However, these documents rarely mention blisters or worms as a particular distress or as a cause for other related distresses [1].

The Florida Department of Transportation (FDOT) has identified blisters and worms on a number of Florida roadways and questioned their impact on long-term pavement life/performance. With a clear understanding of the blister distress, it is believed that FDOT can make appropriate changes to material requirements, mix designs, and construction specifications to remediate the distress and prevent blisters or worms from appearing in new or rehabilitated AC pavements.

1.1. Background

FDOT maintains over 44,000 lane miles of pavements on its total State Highway System [2]. Approximately 96% of these pavements are constructed with an AC surface. Given Florida's relatively hot climate, roadway worms and distortions are encountered throughout the state. Under extreme conditions, these distortions occur over the entire roadway. In addition, distortions occurring in vehicle wheel paths may be compacted by traffic, leaving severe distortions between and outside wheel paths.

Therefore, a need exists to understand the cause of these worms, develop a quantitative assessment of how these distresses affect pavement performance, and update standards or specifications to eliminate future occurrences. To meet this need, FDOT contracted Applied Research Associates (ARA), Inc. to examine the contributing cause(s) for roadway worms and make recommendations for remedial action.

1.2. Research Objectives

The objectives and scope of this research project were as follows:

- Determine the contributing cause(s) for roadway worms.
- Identify the impact on pavement lifespan of roadway worms.
- Develop rehabilitation strategies to prevent roadway worms from occurring.

1.3. Scope

This project included a review of five roadway sites across Florida where worms and blisters exist. Each site was evaluated to assess the cause and impact of blisters, including a visual inspection, nondestructive field testing, and laboratory testing of roadway materials. The FDOT State Materials Office (SMO), in conjunction with personnel from FDOT Districts, obtained pavement cores from each site. Laboratory testing of AC materials was performed by ARA personnel at the FDOT SMO and the U.S. Air Force's pavement materials laboratory at Tyndall Air Force Base, FL. Laboratory testing of bulk samples of granular materials and subgrade was performed by FDOT personnel at the FDOT SMO.

The research consisted of three main efforts:

1) Forensic Evaluation – Determine the cause for roadway worms.
2) Performance Evaluation and Prediction – Identify the impact of worms on pavement lifespan.
3) Mitigation Recommendations and Design Strategies – Recommend correction methods and develop rehabilitation strategies to prevent roadway worms from occurring.

2. LITERATURE REVIEW

2.1. Overview of Pavement Worms

Blisters on pavement surfaces can vary from small bubbles to major bulges measuring several feet. They may occur in isolated spots, or they may be evenly distributed over the pavement surface. The cause of their formation, plus the degree and intensity of these imperfections, determines whether the pavement's performance characteristics have been affected and the possible measures for preventing or correcting these deficiencies. Causes of blistering may be ascribed to the following [3]:

- Moisture vapor pressure.
- Presence of soluble salts.
- Use of unaged steel slag aggregates.
- Microbial action.
- Miscellaneous factors.

2.1.1. Moisture Vapor Pressure

Trapped water, which lies below an impervious AC surface, surface treatment, or tack coat, is the most likely cause of worms and blisters due to the buildup of moisture vapor pressure that is generated in hot conditions [3]. Typically, this type of blister or worm/distortion is cyclical, inflating and deflating according to temperature changes. A relatively impervious pavement surface can cause the blisters to become more permanent, depending on its stiffness. Permanent blisters are prone to splitting and cracking due to traffic applications [3].

The typical situation where blisters occur is a thin and relatively impervious AC overlay placed over an existing AC surface with moisture present. The thin asphalt overlay is bonded to the substratum by a tack coat or similar type of material. Due to poor construction or contamination of the existing pavement surface, areas of inadequate bonding between the overlay and the underlying pavement may develop. Upon heating, the moisture in the unbonded areas expands, causing the AC overlay to form blisters if the expanded gas or vapor is prevented from escaping. If the internal pressure generated in the blister is sufficiently high, the pressure could cause the breakage of the bond between the asphalt overlay and the existing AC surface along the perimeter of the blister, which then grows in size (diameter). Also, cyclic heating and cooling, which results in more inhalation of gas into the blister than exhalation, can cause the blister to increase in height [4]. A diagram illustrating the development of asphalt blistering is provided in Figure 2-1.

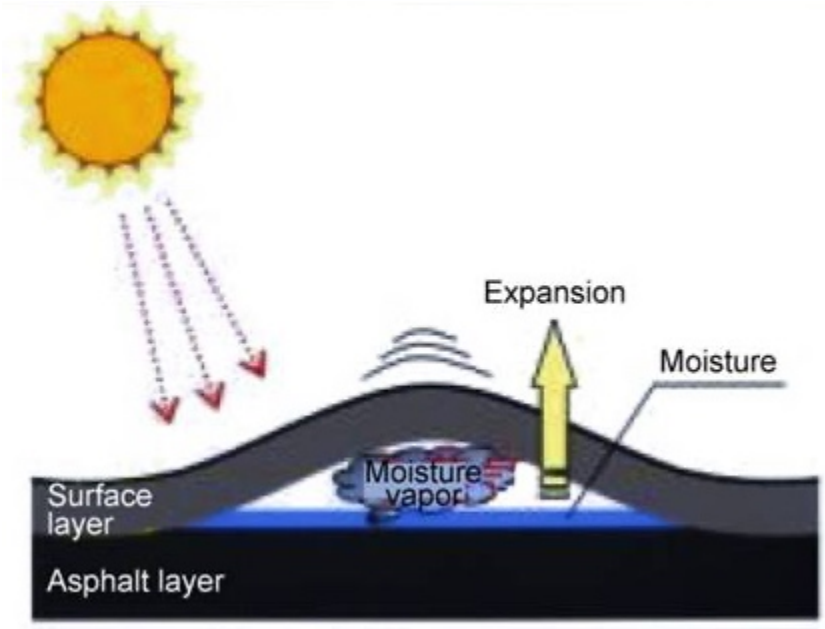

Figure 2-1. Cause of the Blistering Phenomenon

Factors that can contribute to blister formation include:

- Condition of existing AC pavement (cracks, porosity, contamination, etc.) to be overlaid.
- Properties of the AC overlay (gradation, permeability, stability).
- Bonding between existing AC pavement and AC overlay.
- Presence of gas-forming substances (normally water) in the voids.
- Temperature cycles (temperature range of cycles, frequency).

Significant differences in opinions and observations have been reported concerning the effects of these factors on the formation of blisters or worms, even though the basic blister-forming mechanisms are in agreement [4]. The difference of opinions may be due to different conditions and distress mechanisms in the investigations that have been reported.

FDOT has experienced issues with blisters and distortions in the past. Potts [5] reported on an AC overlay in Florida in the summer of 1972 where distortions in the form of random "bubbles" or "blisters" occurred throughout an 11-mile length of a state project. An investigation was conducted to evaluate the underlying issues. The existing pavement consisted of an AC surface over an unbound aggregate base. The moisture content in the existing AC pavement was found to be excessive, ranging from 0.3% to 1.95% for the Type I wearing surface and 1.5% to 1.9% for the binder course. Both the wearing course and the binder course were reported to be porous due to gradation and the asphalt content. Moisture contents in the top 3 to 5 in of base course varied from 9% to 12% and were considered to be within a normal range for base course material. The asphalt mix used in the overlay was found to be rather impervious, with air voids (V_a) at 2.5% to 3.6% and voids in the mineral aggregate (VMA) at 15.4% to 15.8%. The tack coat uniformity was not reported. Chemical analyses were made on the aggregates and bituminous materials used in the project, and the test results indicated nothing in the roadway materials that pointed to gas formation as a cause for the blistering. The upward movement took place during the heat of the day, with greatest movement occurring after the surface temperature was above 125 °F. Potts also reported that a portion of roadway immediately adjacent to the project was overlaid by a different paving contractor, and that section exhibited only a minor amount of blistering [5].

Samples containing blisters were cut from the roadway in 2-ft by 2-ft sections and transported to the laboratory; the sides and bottoms of the samples were enclosed in airtight boxes with provisions for introducing water beneath the sample. Movement of the blisters was monitored over an 18-day period along with surface temperatures. The largest measured upward movement of the samples with water beneath the slab was approximately three times that measured for the dry samples.

Concurrently, the shoulders of the project being investigated were overlaid at the same time as the travel lanes, and no blistering was observed on the shoulders. The shoulder (prior to overlay) consisted of a lime rock base and surface treatment and did not have a binder or surface course. The moisture content of the base materials in the shoulder areas was about 11.5%, in contrast to an approximate 10.5% moisture content of base materials in the traveling lanes. Potts [5] concluded that blisters were caused by excessive moisture in the existing wearing surface/ binder course and the low air void contents and high VMA in the AC overlay. As moisture trapped under the "impermeable" overlay expanded in hot weather, the vapor could not escape upward through the overlay or downward through the existing asphalt pavement, resulting in vapor pressure building up and forming the blister.

Two investigations by the Georgia Department of Transportation (DOT) [3, 4] in the 1980s agreed that the primary cause of blister formations was thermal expansion of trapped moisture and gas between unbonded areas of AC overlays and multiple subsurface types (e.g., over AC pavements, over PCC pavement, and over other types of construction materials such as rubber asphalt overlays and bituthene joint sealing membranes). The affected pavements in Georgia were typically constructed in thin lifts of dense-graded AC with low air voids and often on top of existing concrete pavement. Acott and Crawford [3] stated that Georgia DOT changed from using asphalt emulsion to using AC as a tack coat during this period, assuming trapped residual moisture from asphalt emulsions was causing the blisters.

The authors also indicated other circumstances where water may be introduced into the pavement during construction, including paving an asphalt leveling course over a mix that has received rain. The surface of the pavement may appear to be dry; however, the mix, especially if open-graded, may harbor significant quantities of moisture due to the following:

- Use of very wet aggregate stockpiles or poor aggregate drying techniques.
- Ingress of moisture into pavement structure due to high water table.

Suggested techniques by Acott and Crawford for remediating blisters caused by moisture, along with a summary of causes and symptoms, are provided in Table 2-1.

Table 2-1. Asphalt Blister Causes, Symptoms, and Solutions [3]

Cause	Symptom	Solution
Moisture vapor pressure from trapped water in underlayer.	Punctured surfacing may exhibit a hissing sound as the moisture vapor escapes. A film of moisture may be observed in the blister's interior. Normally associated with thin, impermeable surfacings. Asphalt veining or bleeding sometimes in evidence.	• Exercise caution when using thin impermeable mixtures or heavy tack coats when overlaying porous pavements containing water. • Avoid leaving a porous base or binder course unsurfaced through the winter months or through a rainy season. • Modify grading of AC surfacing to ensure interconnected void structure. • Consider use of vapor pressure relief layer. • Puncture blister with lance and continue rolling. • Can sometimes be broken with a pneumatic roller.

Cause	Symptom	Solution
Moisture vapor pressure from moisture trapped in mix.	Same as above.	• Use correct drying techniques. • Puncture blister with lance and continue rolling. • Modify grading to ensure interconnected void structure.
High water table causing debonding, blistering, and possible formation of ice lenses.	Same as above. Check for poor drainage and/or high water table.	• Improve drainage.

Although moisture vapor has often been cited as the major factor causing blistering in AC overlays, Beijers [6] showed that the presence of water was not necessary for the formation of a blister. To simulate the formation of a blister at the interface between a mastic asphalt overlay and a concrete bridge deck, two concrete slabs (one dry and one wet) were overlaid with three layers of waterproofing asphalt mastic. The center portion of the slab was not bonded to the asphalt mastic, and the entire area surrounding the 1-ft diameter center portion was primed with asphalt to provide good adhesion between the asphalt mastic and the concrete slab. The slabs were heated with infrared radiators. It was reported that this heating pattern gave the quickest results to produce a blister on the unbonded area.

2.1.2. Presence of Soluble Salts

A study of pavement blisters and cracks performed by Netterberg and Bennet [7] observed damage due to the crystallization of common salt (NaCl) between a 13-mm cape seal (chip seal covered with a slurry) and a gravel base course. The gravel base was determined to have an average salt content of 2.2% under areas with blisters, but only 1.5% under areas without blisters. The source of the salt was believed to be salt water used during compaction of the subbase and lower layers. Salt water was used for compaction due to limited availability of potable water. Steps were adopted (1) to rapidly construct the pavement surface and thus prevent migration of salt and (2) to seal the surface with a salt-resistant coating. Neither of these steps were effective, and testing showed the surface to be unusually permeable. Funds were not available for rehabilitation, but the runway was successfully kept in service for over 7 years by periodically rolling the blisters with a staggered wheel pneumatic roller and by patching any damaged areas.

2.1.3. Use of Unaged Steel Slag Aggregates

Unaged steel slag used as aggregate in pavement mixtures can produce crystalline growth when exposed to rainwater, resulting in an expansive reaction. Steel slag is composed primarily of calcium silicates, calcium oxide-ferrous oxide solid solutions, oxides (CaO and MgO), and free lime [8, 9]. The volume changes are initially due to the hydrated unslaked lime, whereas, the long-term expansion is due to the hydration of magnesium oxide. It should be noted that the unaged steel slag that causes expansion is not the air-cooled blast furnace slag obtained from the separation of the iron from the ore. Since Florida does not have a steel manufacturing facility, and the majority of the slag in the state is ground, granulated blast furnace slag, this should not be an issue in Florida.

2.1.4. Microbial Action

The literature contains a number of reports that describe the action of bacteria on asphalt cement and other petroleum-based products [10, 11, 12, 13]. Most AC pavements are unaffected by microbial attack because the effects are so slow that it is considered insignificant compared to other distresses [14]. However, Brown and Darnell [15] found that the presence of

specific inorganic materials in aggregates can promote bacterial action in AC overlays, thus causing blisters. Their study found that the growth of microscopic organisms can produce carbon dioxide and methane gases. A chemical analysis of the aggregate sources used in the AC mix design showed inorganic nitrogen and inorganic phosphorus to be present. These materials were sufficient enough to supply the nutrients needed by the bacteria and generate gases. The study concluded that incorporating 0.5% hydrated lime into the mix design would prevent aerobic and anaerobic growth and gas generation.

2.1.5. Miscellaneous Factors

Another potential cause of blisters and worms was proposed by Croll [16]. Due to the alternation of rapid temperature fluctuations and changes in visco-plastic creep and relaxation phenomena, sufficiently large cycles of tension and compression stress result in the propagation of thermal uplift/buckling mechanisms. Starting with an imperfect, but unstressed, sheet of asphalt at time $t = 0$ and suddenly increasing temperature T, there would be enough elastic deformation to cause a lift-off, but not enough to induce a dynamic snap buckle. Because of the nonlinear elastic-plastic nature of the asphalt, a prediction based on a quasi-linear-elastic material property suggests an uplift lower than that actually produced. If this temperature is maintained for a length of time $t = t_T$, there may be additional growth of uplift; however, the stress resultant is reduced as a result of visco-plastic creep relaxation. When the temperature is decreased, an instantaneous elasti-plastic recovery occurs. At this lower temperature, the visco-plastic stiffness of the asphalt is higher than at elevated temperatures; the time dependent recovery of deformation being lower than that occurring at the previous elevated temperature. The deformation, even over a long recovery period, will unlikely regain the level at which it started the thermal cycle. In this way, there will be a small, incremental uplift after each cycle of temperature. Unless the temperature increase is very high, and over a sustained period, it is likely that the cyclic increments in residual uplift will be very small. Nevertheless, many repetitive thermal cycles have resulted in discernible buildup of permanent uplift.

2.2. The Effect of Worm Distress on Pavement Performance

The literature review did not reveal any insight into the direct effect of roadway worms on pavement performance and reduction in service life. However, as discussed above, the primary cause of blistering in AC overlays as reported in the literature is entrapped moisture vapor in delaminated areas between AC lifts/layers. This lack or partial lack of bonding between these interlayers may cause a premature occurrence of distresses, prominent cracking, premature rutting, slippage, and distortions, which may lead to reduced fatigue life of the pavement structure and increased roughness [17, 18]. As an example, Jaskula and Rys [18] reported that a 30% reduction in interlayer bond from a fully bonded condition may result in a 50% reduction in pavement fatigue life.

2.3. Methods for Assessing Bond between Asphalt Layers

Most pavement design and evaluation techniques assume that adjacent AC layers are fully bonded. The bond between layers ensures that those layers work together as a composite structure to withstand traffic and environmental (e.g., temperature-induced) stresses at the interfaces. However, full bonding is not always achieved, and a number of pavement failures linked to poor bond conditions have been reported [19]. Because full bonding is not always achieved, a theoretical evaluation to investigate the effects of interlayer bond condition on pavement performance is necessary.

Two test approaches are used to quantify the mechanical properties of the interface between pavement layers:

- Destructive testing carried out in-situ or in the laboratory.
- Nondestructive tests carried out on existing pavements.

2.3.1.1. Destructive Tests

Given where the test is performed, destructive testing can be categorized as in-situ destructive testing or laboratory destructive testing. The in-situ destructive testing is usually performed by partially coring or cutting the pavement structure, followed by in-situ testing. Whereas the laboratory destructive testing is usually performed on samples from the pavement structure or laboratory-fabricated specimens, followed by laboratory testing [19].

One commonly used method to determine the tensile bond strength in-situ is the tensile bond test. The tensile pull-off test is performed in accordance with ASTM C1583 and is shown in Figure 2-2 [20]. The tensile pull-off test can be performed either in the laboratory or in-situ. The laboratory version of the test is typically performed on cores or slabs from the pavement structure or laboratory-manufactured specimens. Metal plates are glued to the top and bottom surfaces of the specimens. A test machine then applies tensile force in the axial direction to pull the specimen apart. Testing at different temperatures can be performed by conditioning the specimens in a temperature-controlled chamber prior to testing [21].

Figure 2-2. Tensile Pull-Off Tester

In-situ bond tests can be performed with the tensile pull-off tester. A core or saw cut is made to a depth just below the interface of interest. A metal plate is glued on top of the pavement surface and attached to the tensile pull-off tester. The top lift/layer of AC is then pulled-off in the axial (upward) direction to measure bond strength. This in-situ test is typically limited to the interface between the surface lift/layer and the layer below.

A direct shear test device, shown in Figure 2-3, can also be used to measure bond strength in the laboratory. The reference test method for the debonding test is American Association of

State Highway and Transportation Officials (AASHTO) TP 114, “Standard Method of Test for Determining the Interlayer Shear Strength (ISS) of Asphalt Pavement Layers.”

Figure 2-3. Bond Strength Shear Test Fixture

The interlayer shear strength test can be performed with or without a normal force load being applied to the sample. The normal force load is applied to simulate wheel loads being applied on the AC pavement. The interlayer shear strength test can also be performed in an environmental chamber to investigate the performance of the bond at different temperatures [19].

2.3.1.2. Nondestructive Tests

A number of nondestructive test (NDT) procedures are available for assessing the presence and extent of delamination of AC in the field. Technologies identified in a 2010 asphalt bond study [22] as having high potential for detecting delamination include seismic, impulse, and electromagnetic NDT test methods.

2.3.1.2.1. Portable Seismic Pavement Analyzer (PSPA)

The PSPA, shown in Figure 2-4, uses the principle of ultrasonic surface wave velocity to identify transitions between asphalt lifts and changes in modulus with depth. The PSPA consists of an electric solenoid source and two accelerometers packaged as a hand-portable unit. In operation, the PSPA load creates stress waves that propagate to the accelerometers. The measurements are reduced in laptop software to determine seismic moduli and layer thickness. Resulting modulus values and dispersion curve shapes provide an indication of whether layer interfaces are intact or damaged. The fairly uniform PSPA dispersion curve presented in Figure 2-5a indicates an intact layer structure. The sharp decrease in modulus that occurs at approximately 3 in. depth in Figure 2-5b indicates a damage point. The average moduli of the damaged layer is approximately 25% less than the intact core [17, 23].

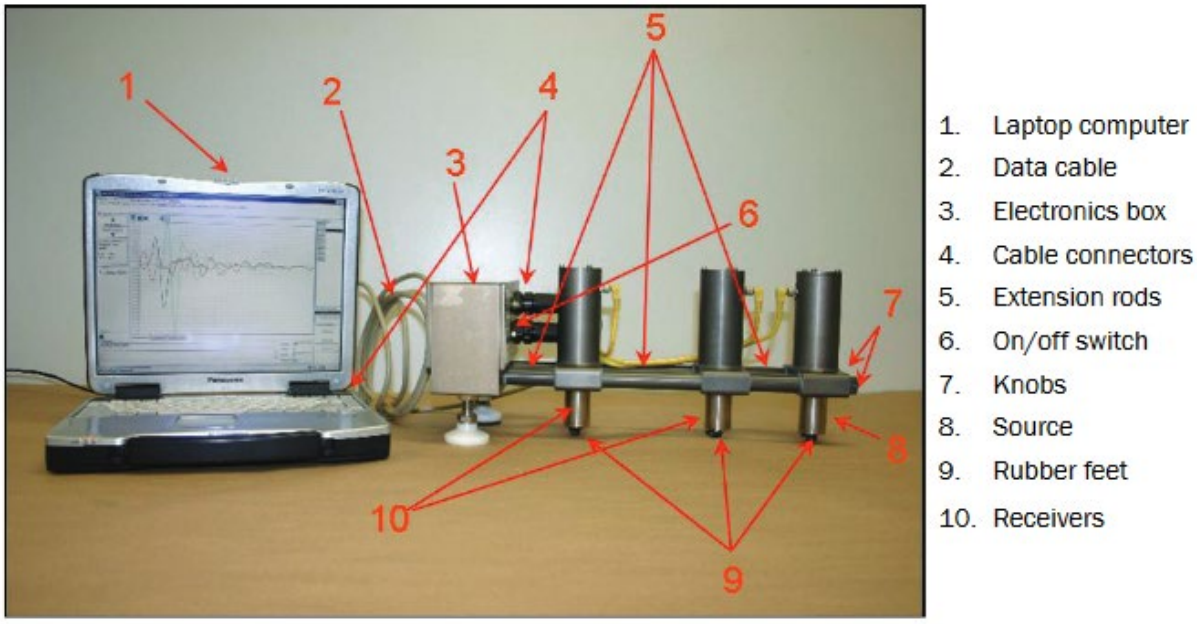

Figure 2-4. Equipment Components of PSPA [23]

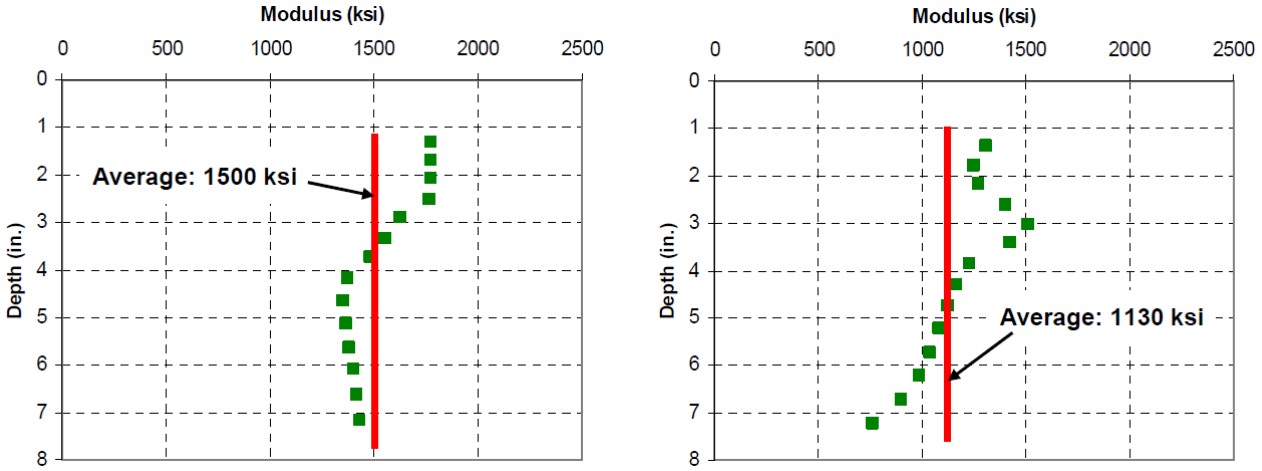

(a) Interlayer intact ***(b) Severe interlayer debonding***

Figure 2-5. PSPA Dispersion Curves [17]

2.3.1.2.2. Ground Penetrating Radar (GPR)

GPR is a demonstrated [24] method for identifying different layers within a layer pavement system. GPR systems direct short radio pulses of electromagnetic energy into the ground or pavement using an antenna capable of transmitting and receiving signals. When this pulse of energy is transmitted through a layered structure and encounters materials of significantly different electromagnetic properties, a portion of the signal is reflected back to the antenna while the rest continues penetrating into the next layer. The amount of energy that reflects back or continues penetrating is a function of the contrasting electromagnetic properties of the

materials. Material interfaces with greater contrasting electromagnetic properties produce reflections of higher amplitude.

The effective depth of penetration [25] of the radar energy is primarily a function of (1) the electrical properties of the material that the signal is transmitted through, (2) frequency of transmitted radar signal, and (3) overall system characteristics, such as power output and receiver sensitivity. Lower frequencies achieve greater penetration depths but decrease vertical resolution.

More recently, the Texas Transportation Institute (TTI) [26] utilized GPR on new AC pavement construction to ascertain the differences between a steel wheel roller and pneumatic wheel roller for breakdown rolling. TTI determined there were serious subsurface anomalies and density variation in the AC layers using GPR. An example of the information gathered is represented in Figure 2-6. Later cores were taken from the different sections to validate debonding of layers and were evaluated using an X-ray computed tomography (CT) scanner to determine uniformity and air voids.

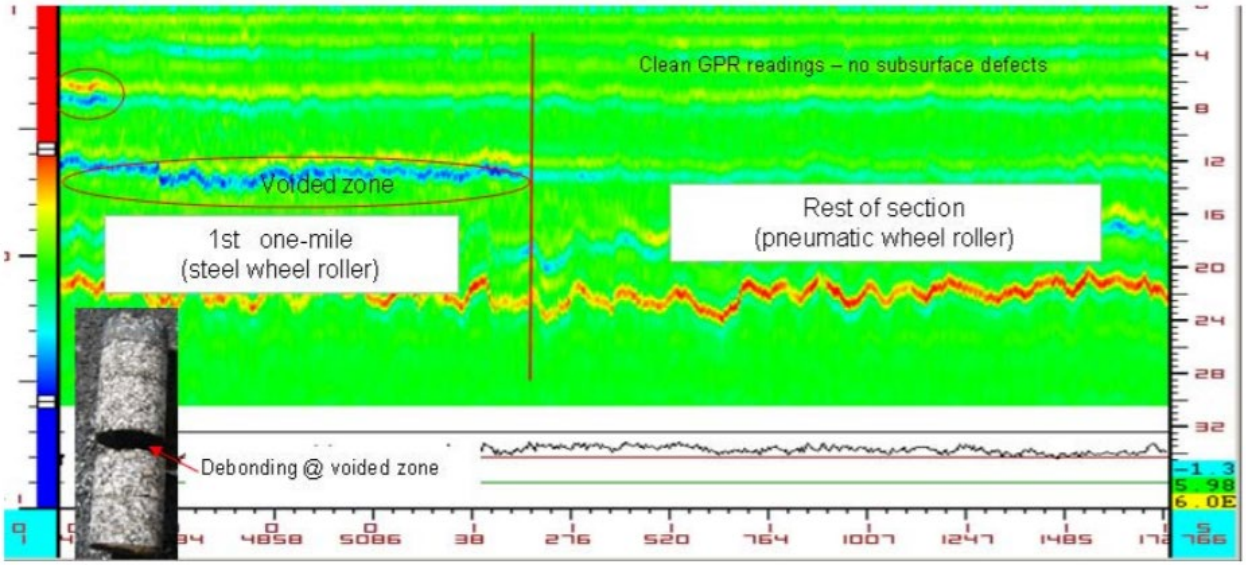

Figure 2-6. Steel Wheel versus Pneumatic Breakdown Roller on IH35-Laredo [26]

2.3.1.2.3. Falling Weight Deflectometer (FWD)

Al Hakim et al. [27] used the FWD deflection bowls for predicting the bond condition between AC pavement layers. A simple backcalculation method was developed using static analysis with the pavement modeled as a linear elastic system. The stiffnesses of the AC, subbase, and subgrade layers, in addition to the bonding stiffness between the AC layers, are backcalculated from the deflection bowls. The surface deflection bowls under the FWD loading, pavement material types, layer thicknesses, and Poisson's ratios have to be known for the analyzed pavement. The FWD may not be able to distinguish debonding of thin upper layers but may be able to determine if a structural change has occurred, possibly due to debonding.

3. METHODS AND PROCEDURES

The technical approach for this study included a field and laboratory investigation of five Florida roadways exhibiting worm distress. The investigations were conducted on roadway projects that exhibited both (1) segments of worm distress and (2) segments without worm distress. In each case, roadway sections were continuous projects of the same construction. This approach permits ideal pairs of test and control sections for comparison in order to identify the mechanism(s) causing worm distress.

3.1. Test Sites

A list of candidate test sites was provided by FDOT along with relevant site information as to location, traffic levels, and maintenance history. Sites were selected to be representative of conditions throughout the state that contain the worm distress. The FDOT District offices for each site were contacted to obtain historical data.

Suitable test areas were selected based on several criteria:

- Historical data available.
- Representative of overall conditions throughout the state of Florida.
- Pavement surface type and age.
- Value and extent of available data.
- Ease of collecting samples (traffic control, accessibility, etc.).

Roadway characteristics of the five sites investigated are presented in Table 3-1, with their geographic locations shown in Figure 3-1. FDOT project numbers and associated milepost limits for worm-distressed and control sections are presented in Table 3-2.

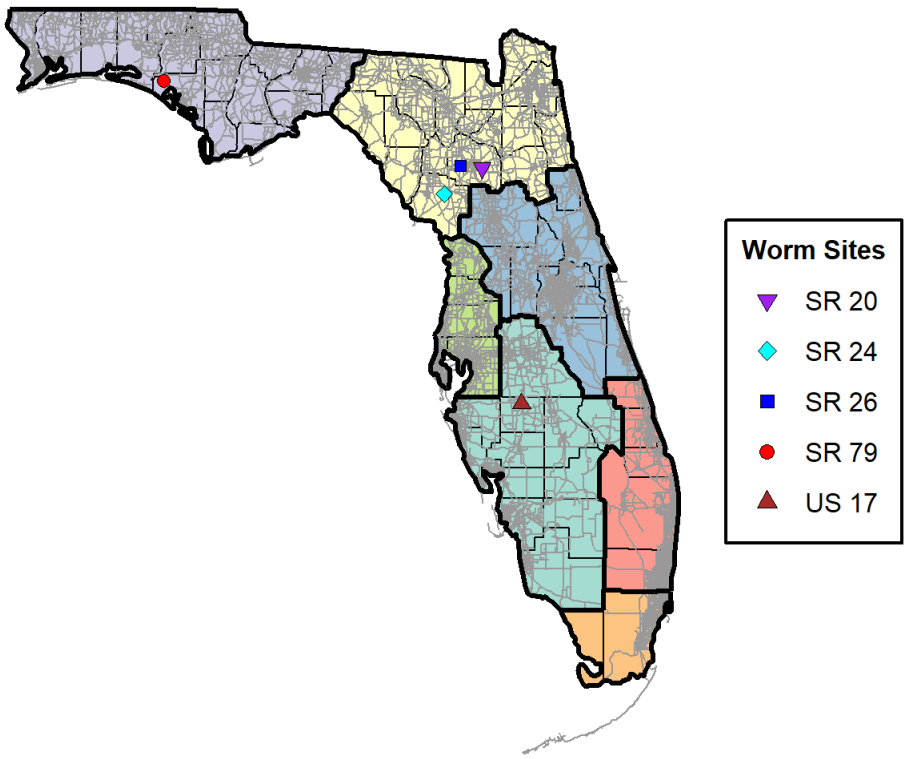

Figure 3-1. Roadway Worm Test Site Locations

The five Florida roadways evaluated in this study represent:

- Pavements from FDOT Districts 1, 2, and 3.
- Two- and four-lane systems.
- Ages from 4- to 18-years from last major rehabilitation.
- Traffic levels ranging from 1,400 annual average daily traffic (AADT) to 23,400 AADT in the opening year after construction/rehabilitation.

Sections were nominally 581 ft long; however, lengths were adjusted depending on road conditions and presence of worm distress. Design cross sections for each roadway were compiled from FDOT construction records and are provided in Figure 3-2. Both nondestructive and destructive tests were conducted at each test site.

Table 3-1. Roadway Characteristics

Roadway	FDOT District	County	Surface Type	Posted Speed Limit (mph)	Traffic Lanes	Lanes Evaluated	Age Since Last Major Maintenance & Rehabilitation (yr)	Design AADT[1]
SR 79	3	Washington	OGFC[2]	65	4	L1	7	5,250
SR 26	2	Alachua	DGA[3]	50	4	R1	18	15,100
SR 24	2	Levy	DGA	45 - 60	2	L1	4	1,400
US 17	1	Hardee	OGFC	65	4	R1	9	23,400
SR 20	2	Alachua	DGA	65	4	R1	17	NA[4]

[1]Opening year estimate
[2]Open-graded friction course
[3]Dense-graded asphalt
[4]Data not available

Table 3-2. Roadway Sections

Roadway	Project ID	Roadway ID	Control Section Mileposts		Worm Section Mileposts		Test Section Length (ft)	Control Section Length (ft)
			Start	End	Start	End		
SR 79	217911-652-01	61040000	0.336	0.396	0.396 (T1)	0.442 (T1)	720[1]	321
					0.305 (T2)	0.336 (T2)		
SR 26	207758-1-52-01	26070000	8.768	8.815	8.815	8.912	581	250
SR 24	430548-1-52-01	34070000	22.405	22.556	31.114	31.224	581	797
US 17	194028-2-52-01	06010000	17.346	17.456	17.713	17.823	581	581
SR 20	2017816-1	26080000	2.899	2.998	2.418	2.579	581	525

[1]Combined Length of Worm Section T1 and T2; Control Section of SR 79 was in between T1 and T2

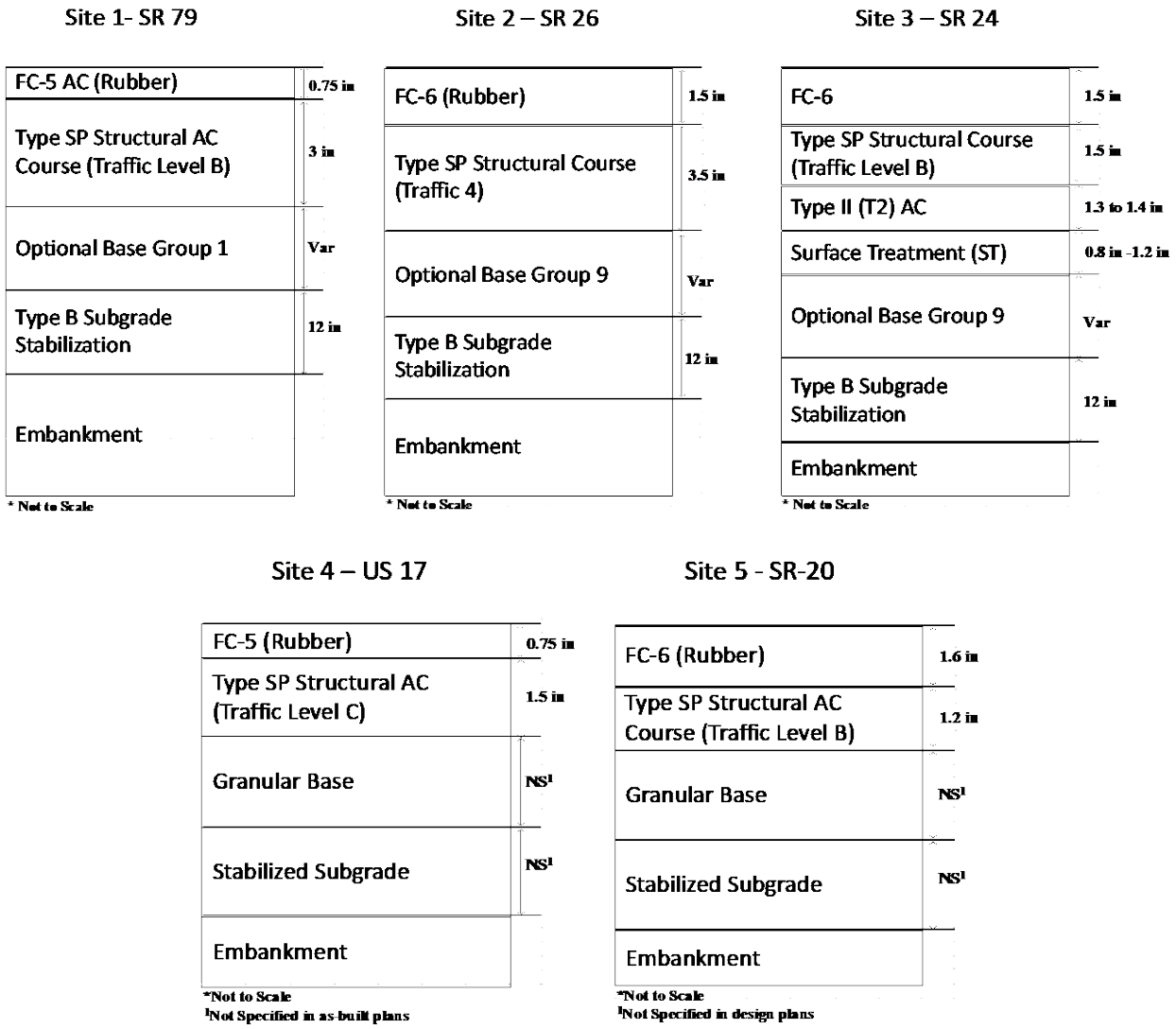

Figure 3-2. Test Site Pavement Cross-Section Design

Descriptions of each project are provided in the following sections.

3.1.1. Site 1 – FL SR 79

The SR 79 project location is in Washington County inside FDOT District 3. This pavement is a four-lane roadway constructed in 2009. Worm distress was first noted in FDOT pavement survey records 7 years after construction, just months prior to this study. It is likely the worm distresses were present before seven years age; however, it is unknown when the distresses first occurred. Figure 3-3 shows an overview of the SR 79 worm section. The worm-distressed test section includes approximately 721 ft of the southbound left lane of SR 79. The southern boundary of the test section begins approximately 1.25 mi south of the intersection of SR 20 and SR 79 and continues approximately 720 ft south to the intersection of SR 79 and

Environmental Road, terminating short of the northern boundary of Bay County. The north and south boundaries of the test section also coincide with the beginning and end of a turn lane.

Figure 3-3. SR 79 Roadway Overview

No separate, discrete area was available for a control section. The selected control section with no visible surface worm distress was limited to a 310-ft segment that begins 243 ft south of the northern test section boundary and ends 553-ft south of the northern test section boundary. The worm distresses are prominent in magnitude and density, occurring as both round and roughly rectangular in shape (Figure 3-4). The roadway surface is an open-graded friction course (OGFC). The worm distresses ranged in height from approximately 0.25 to 0.5 in. The area of the project studied is composed of a superelevated section of roadway where worm distresses increase in density with lanes at lower elevation. The most severe worm distresses were observed in the turning lane at the lowest elevation point. No standing water or drainage issues were observed.

Figure 3-4. SR 79 Worm Distress

3.1.2. Site 2 – FL SR 26

The SR 26 project location is in Alachua County inside FDOT District 2. This pavement is a four-lane roadway constructed in 2002. Worm distress was first noted in FDOT survey records eight years after construction. The eastern boundary of the 250-ft control section is located 190 ft west of the intersection of SW 161 Terrace and SR 26. The worm-distressed test section is 457 ft long and shares its eastern boundary with the control section. An overview of the SR 26 project is provided in Figure 3-5.

Worms are present in un-trafficked areas of the lane but primarily between the wheel paths. A greater density of the worm distress is present where the longitudinal crack component of block cracking occurs (Figure 3-6). The research team originally assumed the presence of cracking would provide relief for the mechanism causing worms; however, this does not appear to be the case. Worms occur on the site despite there being a substantial amount of age-related cracking on the pavement surface. The roadway consists of 12-ft lanes and a divided median. Curb and gutter are present throughout. A cross-slope drains water from the inside lanes to the outside lanes. The cross-slope ranges from 1.3% to 2.3% in the worm section and 0.8% to 2.9% in the control section. No standing water or drainage issues were observed.

Figure 3-5. SR 26 Roadway Overview

Figure 3-6. SR 26 Worm Distress

3.1.3. Site 3 – FL SR 24

The SR 24 project location is in Levy County inside FDOT District 2. This pavement is a two-lane roadway last resurfaced in 2015. The worm section is 797 ft long, and the control section is 581 ft long. The two sections are separated by approximately 8.6 mi. Of the five projects evaluated in this study, this is the greatest distance between sections. The eastern boundary of the worm section is located 1.7 mi west of the intersection of US 27 and SR 24. The eastern boundary of the control section is located 0.97 mi west of the intersection of US 98 and SR 24. An overview of the SR 24 project is provided in Figure 3-7.

The worm distress uplift height observed on SR 24 was approximately 0.25 in. The majority of the worm distress did not accompany cracking and was difficult to photograph. Figure 3-8 presents a worm occurrence that caused a fracture in the wearing course. The worm distresses occurring on the test section are relatively small in size (footprint), low in frequency of occurrence, and low in severity (height), making them difficult to detect visually on the ground. The distresses are more easily detected in early morning/late evening lighting conditions or by driving the road in an automobile to feel intermittent roughness that occurs due to worms between wheel paths. The roadway consists of two 12-ft lanes. The centerline is crowned. The longitudinal paving joint at the crown of the roadway has opened to form a crack for approximately 50% of the length of the worm section; however, the control section did not have cracking at the paving joint. Cross slopes range from 1.4% to 2.4% in the worm section and 1.9% to 2.0% in the control section. No standing water or drainage issues were observed.

Figure 3-7. SR 24 Roadway Overview

Figure 3-8. SR 24 Worm Distress

3.1.4. Site 4 – FL US 17

The US 17 project location is in Hardee County inside FDOT District 1. This pavement is a four-lane roadway last resurfaced in 2011. Worm distress was first noted in FDOT pavement survey records 6 years after construction. Both the worm section and control sections are 581 ft long and separated by 0.389 mi. The southern boundary of the worm section is located 0.1 mi south of the intersection of US 17 and FL-62. The southern boundary of the control section begins at the intersection of Maxwell Dr. and US 17. An overview of the US 17 project is provided in Figure 3-10.

The worm distresses occur both as round and roughly rectangular in shape (Figure 3-10). The roadway surface is an OGFC. The worm distresses ranged in height from approximately 0.25 to 0.5 in. The control section is at a higher elevation on a vertical curve. The severity of worm distress increases in areas of lower elevation. The roadway consists of two 12-ft lanes. The centerline is crowned. Cross slopes range from 1.1% to 3.1% in the worm section and 1.2% to 2.6% in the control section. No standing water or drainage issues were observed.

Figure 3-9. US 17 Roadway Overview

Figure 3-10. US 17 Worm Distress

3.1.5. Site 5 – FL SR 20

The SR 20 project location is in Alachua County inside FDOT District 2. An overview of the site is shown in Figure 3-11. The worm-distressed test section includes approximately 581 ft of the eastbound left lane of SR 20. This pavement section was last resurfaced in 2003. Worm distress was first noted in FDOT survey records seven years after construction. The western boundary of the test section begins 170 ft west of the intersection of SR 20 and SE 39th Terrace and continues approximately 581 ft west. The end of the test section also coincides with the start of a left turn lane, which was constructed as a widening to the mainline in 2003. The control section is 525 ft long, and its eastern boundary is the intersection of SR 20 and SE 46th Terrace.

This roadway features two different dense-graded asphalt (DGA) surface mixes. Both lanes exhibit worm distresses, indicating worm distress may not necessarily be being associated with factors related to the top AC lift. Worm distresses are not considerably severe (< 0.25 in tall) and occur infrequently. No worm distresses were observed over 390 ft of the 581-ft test section. Figure 3-12 presents a close-up of a worm distortion on the left edge of the worm section. The roadway consists of 12-ft travel lanes, with a 5-ft gore area separating the mainline from a 6-ft parking lane. Curb and gutter are present throughout. A cross-slope drains water from the inside lanes to the outside lanes. The cross-slope ranges from 1.6% to 2.7% in the worm section and 1.9% to 2.8% in the control section. No standing water or drainage issues were observed.

Figure 3-11. SR 20 Roadway Overview

Figure 3-12. SR 20 Worm Distress

3.2. Field Test Program

Site assessments were made at each project to evaluate conditions such as terrain, surface drainage, drainage structures, embankments, and vegetation. Photographs were collected to document site conditions and the appearance of the distresses at each site. Each sample unit was mapped to document the locations of worms that may exist in addition to all other distresses that might impact pavement performance and affect the research analysis. The size, density, and severity of worms within the sample unit was measured—horizontal dimensions as well as height. Field testing and materials sampling were performed on the projects between September 2018 and January 2020. The following NDT data were collected at each site in this study:

1) Pavement Condition Index (PCI)
2) Falling Weight Deflectometer (FWD)
3) Ground Penetrating Radar (GPR)
4) Portable Seismic Pavement Analyzer (PSPA)
5) Dynamic Cone Penetrometer (DCP)

The following materials were sampled from each site:

1) Six-inch diameter AC cores
2) Twelve-inch diameter AC cores
3) Base
4) Subgrade
5) Embankment

An example map of NDT test and core sampling locations for the first test site is provided in Figure 3-13. Sections 3.2.1 through 3.2.7 describe NDT testing and materials sampling. Cores were

collected from the lane center for laboratory testing. Some offsets were adjusted in the field to avoid coring over distresses on the pavement. Additional cores were collected from the pavement edge and wheel paths for observation.

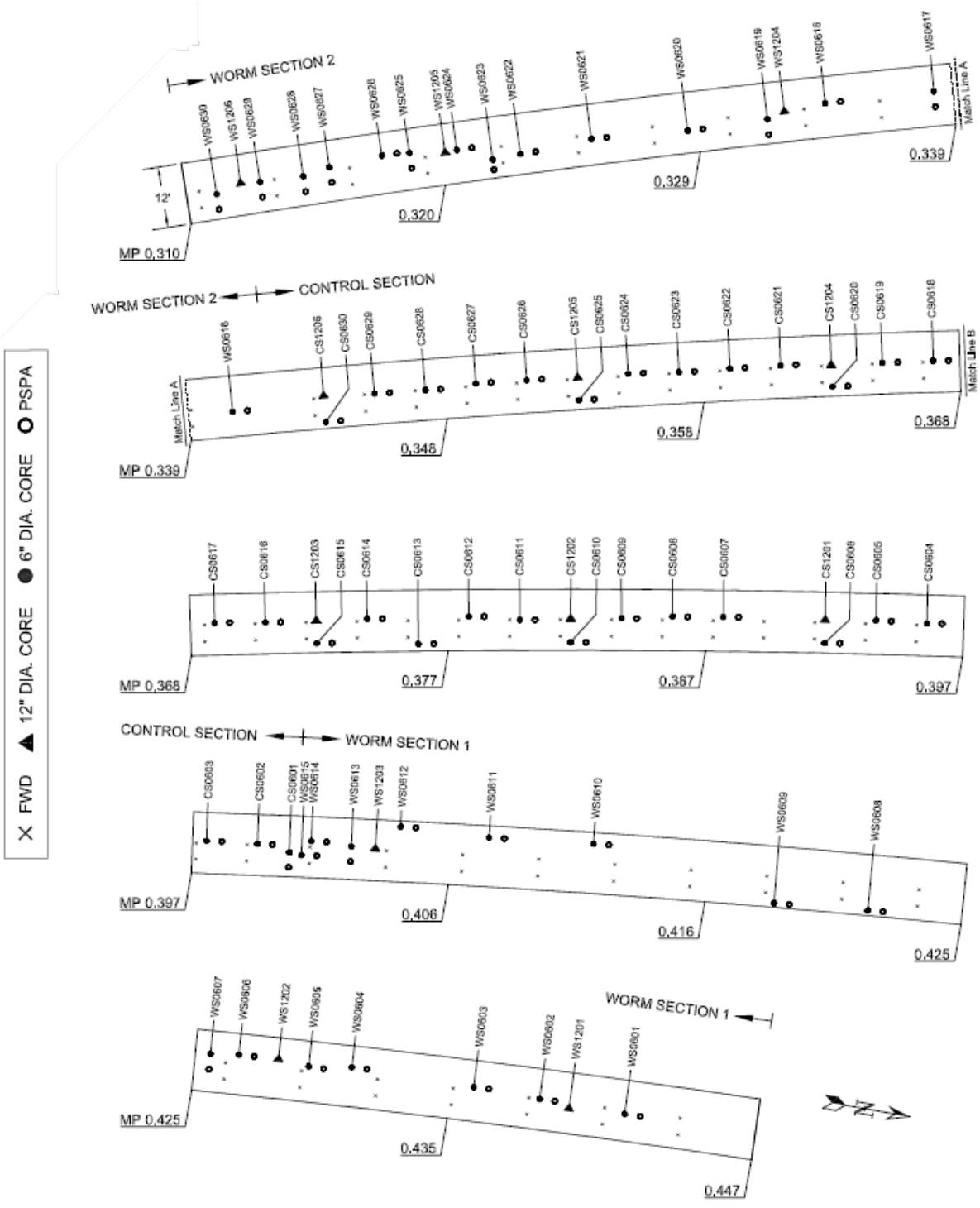

Figure 3-13. Sample Field Data Collection Map (Site 1 – SR 79)

3.2.1. Pavement Condition Index (PCI)

PCI surveys were conducted over the entirety (100% sampling rate) of test and control section pavement surfaces. Each sample unit was mapped to document the locations of worms that may exist in addition to all other distresses that might impact pavement performance and affect the research analysis. The size, density, and severity of worms within the sample unit was measured—horizontal dimensions as well as height. Other distresses within the sample unit were recorded. The cracking and rutting assessments performed during the course of the PCI survey are presented in Figure 3-14 and Figure 3-15, respectively.

Figure 3-14. PCI Cracking Survey Process

Figure 3-15. PCI Rutting Survey Process

Four distress types were observed across all the projects: alligator cracking, block cracking, longitudinal and transverse (L&T) cracking, and rutting. A summary of each PCI distress is provided below, and Table 3-3 presents a summary of the PCI distress severity criteria.

1. Alligator Cracking: Alligator or fatigue cracking is a series of interconnecting cracks caused by fatigue failure of the AC surface under repeated traffic loading. Cracking begins at the bottom of the asphalt surface, or stabilized base, where tensile stress and strain are highest under a wheel load. The cracks propagate to the surface initially as a series of parallel longitudinal cracks. After repeated traffic loading, the cracks connect, forming many sided, sharp-angled pieces that develop a pattern resembling chicken wire or the skin of an alligator. The pieces are generally less than 1.5 ft on the longest side. Alligator cracking occurs only in areas subjected to repeated traffic loading, such as wheelpaths. Pattern-type cracking that occurs of an entire area not subjected to loading is called “block cracking,” which is not a load-associated distress.
2. Block Cracking: Interconnected cracks that divide the pavement into approximately rectangular pieces. The blocks may range in size from approximately 1 to by 1 ft to 10 by 10 ft. Block cracking is caused mainly by shrinkage of the AC and daily temperature cycling, which results in daily stress/strain cycling. The distress is not load-associated. Block cracking usually indicates the asphalt has hardened significantly. Block cracking normally occurs over a large portion of the pavement area, but sometimes will occur only in nontraffic areas. This type of distress differs from alligator cracking in that alligator cracks form smaller, many sided pieces with sharp angles. Also, unlike block, alligator cracks are caused by repeated traffic loadings, and therefore, are found only in traffic areas, that is, wheel paths.

3. Longitudinal and Transverse (L&T) Cracking: Longitudinal cracks are parallel to the pavement's centerline or laydown direction. They may be caused by: (1) a poorly constructed paving lane joint, (2) shrinkage of the AC surface due to low temperatures or hardening of the asphalt, or daily temperature cycling or both; (3) a reflective crack caused by cracking beneath the surface course, including cracks in PCC slabs but not PCC joints; or (4) transverse cracks extending across the pavement at approximately right angles to the pavement centerline or directions of laydown. These types of cracks are not usually load associated.
4. Rutting: A surface depression in the wheel paths. Pavement uplift may occur along the sides of the rut, but, in many instances, ruts are noticeable only after rainfall when the paths are filled with water. Rutting stems from a permanent deformation in any of the pavement layers or subgrades, usually caused by consolidated or lateral movement of the materials due to traffic load.

Table 3-3. PCI Distress Severity Criteria Summary

PCI Distress	Low Severity (L)	Medium Severity (M)	High Severity (H)
Alligator Cracking	Longitudinal hairline cracks with few or no interconnecting cracks.	Further development of light alligator into a pattern or network of cracks that may be lightly spalled.	Network or pattern of cracks where pieces are well defined and spalled on edges, some pieces rock under traffic.
Block Cracking	Blocks are defined by cracks with < 3/8-in. width (non-filled). Filled cracks are in good condition.	Blocks are defined by medium severity L&T (3/8 in to 3 in) non-filled. Filled cracks of any width surrounded by light random cracking.	Blocks are defined by any crack filled or non-filled which is surrounded by medium or high severity random cracking, or non-filled cracks > 3 in or any width crack where the 4 in of pavement around the crack is broken.
Longitudinal and Transverse (L&T) Cracking	Cracks with <3/8 in width (non-filled). Filled cracks are in good condition.	Cracks are 3/8 in to 3 in non-filled. Filled cracks of any width surrounded by light secondary cracking.	Any crack filled or non-filled which is surrounded by medium or high severity secondary cracking, or non-filled cracks >3 in, or any width crack where the 4 in of pavement around the crack is broken.
Rutting	A wheel path surface depression 1/4 in to 1/2 in depth.	A wheel path surface depression 1/2 in to 1 in depth.	A wheel path surface depression with a depth > 1 in.

3.2.2. Falling Weight Deflectometer (FWD)

FWD deflection basins and time histories were collected at a spacing of 10 ft to 20 ft, depending on the length of the section. The goal was to collect the FWD data from at least 30 drop locations within each section. The use of FWD data is discussed in more detail in Section 4.1.3. Accurate layer thickness is important for backcalculation of layer modulus values, so it was decided to confirm the layer thickness and material type through coring of the AC. All FWD measurements were obtained prior to any AC coring.

3.2.3. Ground Penetrating Radar (GPR)

GPR data were collected using ground-coupled, air-launched, and PaveScan systems. These systems are shown in Figure 3-16 through Figure 3-18. All GPR measurements were collected prior to any AC coring being performed. The GPR data were assessed to determine the areas where material deterioration/moisture damage (stripping) might have occurred. GPR can also provide layer thickness and help identify larger void areas. Nevertheless, the data from ground-coupled and air-launched GPR systems did not provide any insight into potential voids, delamination, or other anomalies that may have contributed to blisters. As such, only the PaveScan results are discussed in Section 4.1.1.

Figure 3-16. Ground-Coupled GPR

Figure 3-17. GSSI PaveScan RMD

Figure 3-18. Vehicle-Based Air-Coupled GPR

3.2.4. Portable Seismic Pavement Analyzer (PSPA)

A minimum of five PSPA measurements were collected over five evenly spaced locations in the center of each lane of each test section (control and worms). The PSPA was used to determine modulus values for the AC, identify transitions between AC layers/lifts, and identify changes in modulus depth. The PSPA collects data that is affected more by local conditions in a small area. Figure 3-19 shows a PSPA test being conducted.

Figure 3-19. PSPA Test

3.2.5. Core Samples of AC Pavement

AC core samples (for full depth of AC pavement) were obtained to provide understanding of the characteristics and causes of blisters/worms. Cores were mapped, labeled (coded to reflect test site, sample unit, and location within sample unit), and photographed. Interfaces between lifts were measured and recorded. All cores were taken from one lane of the road to minimize disruption to traffic. A minimum of 30, 6-inch cores were taken from each sample unit to provide a statistically valid result in terms of core thickness, density, air voids, aggregate gradation, and permeability. This number of 6-inch cores is also required for testing at least five replicate samples in water permeability, interlayer shear strength, and resilient modulus laboratory tests. The number of cores also provides for contingency samples in the event that some of the cores are damaged prior to testing.

An additional six 12-in cores were taken in evenly spaced intervals along the center of the lanes to permit bulk sampling of base, subgrade, and embankment materials for laboratory testing. Coring operations over these areas were performed wet until the core barrel reached approximately 0.25-in to 0.5-in distance above the bottom of the asphalt structure. A portable wet-vacuum was used to remove as much water as possible from the coring operations, then the remaining depth of the AC was cored without water to mitigate moisture from entering the road base (Figure 3-20 and Figure 3-21).

Figure 3-20. Partial-Depth Wet-Coring and Vacuuming of 12-in Diameter AC Samples Prior to Dry Coring

Figure 3-21. Sampling Base, Subgrade, and Embankment Materials

3.2.6. Dynamic Cone Penetrometer (DCP)

DCP tests were conducted to measure the in-situ resistance of roadbed foundation layers to penetration. These data were correlated to California bearing ratio (CBR) and permitted comparison between the granular material shear strength of worm-distressed and control test sections. DCP tests were performed on the surface of the road base after 12-in diameter AC

cores were drilled and removed. The DCP was performed through the base, subgrade, and embankment materials. Tests were performed in accordance with *ASTM D6951 – Standard Method for Use of The Dynamic Cone Penetrometer in Shallow Pavement Applications* [28]. CBR was calculated as

$$CBR = \frac{292}{PR^{1.12}} \quad \textbf{(1)}$$

Where PR is the DCP penetration rate in millimeters per blow.

On layers where a DCP refusal was encountered, those materials were manually removed and the DCP test was reinitiated on the underlying layer. Layer thicknesses were measured in the field with a steel tape measure. These thicknesses were used in the identification of discrete layers for data analysis. Manual DCP tests were performed on SR 79 (Figure 3-22). Automated DCP tests were conducted on the remaining roadway test sites (Figure 3-23).

Figure 3-22. Manual DCP Test

Figure 3-23. Automated DCP Test

3.2.7. Bulk Samples of Base Aggregate and Subgrade

Bulk samples of granular base and subgrade were obtained in accordance with FDOT standard FM 1 T-002 and transported to the laboratory. Bulk samples were placed in heavy plastic bags and 5-gal buckets with gasketed lids to prevent changes in moisture content.

3.3. Laboratory Test Program

The primary goals of the laboratory testing were (1) to identify the pavement material characteristics that may have contributed to the worm distress and (2) to assess the impact of worm distress on pavement deterioration. In addition to a suite of AC materials characterization and performance tests, physical properties of the underlying geotechnical materials were characterized to assess potential variation between worm- and control-group sampled materials. Table 3-4 provides a list of tests performed on AC core samples, while Table 3-5 provides the list of tests performed on unbound materials (i.e., base, subgrade, and embankment).

Table 3-4. Laboratory Tests on AC Materials

Test Type/Result	Test Name/Description	Reference Standard
Extraction/Binder Content	Standard Test Methods for Quantitative Extraction of Bitumen from Bituminous Paving Mixtures	ASTM D2172
Maximum Gravity	Theoretical Maximum Specific Gravity and Density of Bituminous Paving Mixtures	FDOT FM 1-T 209
Field Core Density	Bulk Specific Gravity of Compacted Bituminous Mixtures using Saturated Surface-Dry Specimens	FDOT FM 1-T 166
AC Modulus	Determining the Resilient Modulus of Bituminous Mixtures by Indirect Tensile Test (IDT)	ASTM D7369
Aggregate Particle Size	Mechanical Size Analysis of Extracted Aggregate	FDOT FM 1-T 030
AC Permeability	Measurement of Water Permeability of Compacted Asphalt Paving Mixtures	FDOT FM 5-565
Interlayer Bond Strength	Determining the Interface Interlayer Bond Strength between Asphalt Pavement Layers	FDOT FM 5-599

Table 3-5. Laboratory Tests on Geotechnical Materials

Pavement Layer	Test Type/Result	Test Name/Description	Reference Standard
Base	Base Particle Size	Standard Method of Test for Particle Size Analysis of Soils	AASHTO T 88
Base	Atterberg Limits	Standard Method of Test for Determining the Plastic Limit and Plasticity Index of Soils	AASHTO T 90
Base	Optimum Moisture Content	Standard Method of Test for Moisture-Density Relations of Soils using a 10-lb Rammer and 18-in Drop	AASHTO T 180
Base	Lime Rock Bearing Ratio (LBR)	Florida Method of Test for LBR	FM 5-515
Subgrade	Subgrade Particle Size	Standard Method of Test for Particle Size Analysis of Soils	AASHTO T 88
Subgrade	Atterberg Limits	Standard Method of Test for Determining the Plastic Limit and Plasticity Index of Soils	AASHTO T 90
Subgrade	Optimum Moisture Content	Standard Method of Test for Moisture-Density Relations of Soils using a 5.5-lb Rammer and 12-in Drop	AASHTO T 99
Embankment	Soil Particle Size	Standard Method of test for Particle Size Analysis of Soils	AASHTO T 88
Embankment	Atterberg Limits	Standard Method of Test for Determining the Plastic Limit and Plasticity Index of Soils	AASHTO T 90
Embankment	Optimum Moisture Content	Standard Method of Test for Moisture-Density Relations of Soils using a 5.5-lb Rammer and 12-in Drop	AASHTO T 99

4. RESULTS AND DISCUSSION

Test results and observations from the field-testing program are provided in the following sections.

4.1. Field Test Results

4.1.1. Ground Penetrating Radar (GPR)

With the exception of SR 79, the PaveScan GPR data was collected from both the control and the worm sections of all field sites. The PaveScan data was collected with a total of three GPR antennas located at both wheel paths (outside antennas were positioned four feet from pavement edge lines) and at the lane center. Figure 4-1 through Figure 4-4 show the dielectric profiles collected from the respective sections using PaveScan. These figures clearly show that the dielectrics from worm sections exhibit higher variability (i.e., inconsistency) compared to the control sections. Moreover, these figures generally indicate that the highest variability within the worm sections is observed from the lane center. This indicates that the wheel paths of worm sections may have been compacted by the driving traffic, leaving more inconsistency in the lane center where lower density may exist. The variability or inconsistency in the SR 20 worm section was less pronounced than the other three roadways; however, this observation was consistent across all sites.

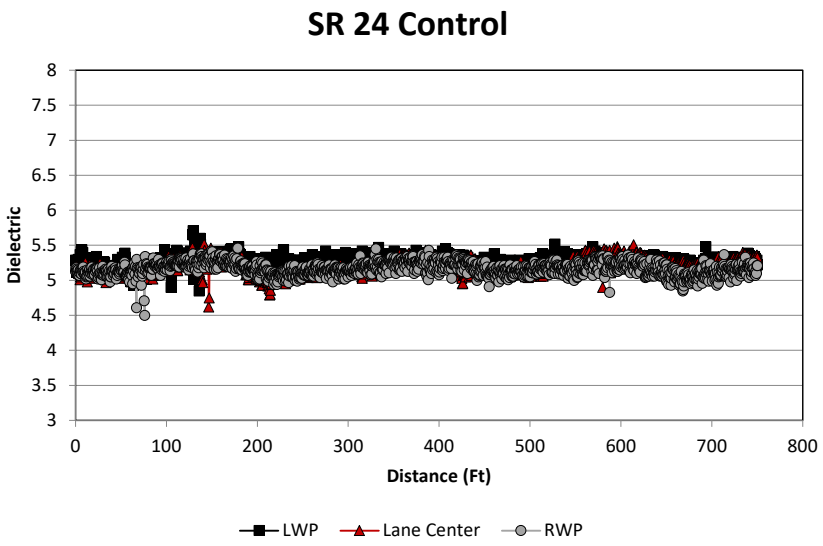

(a)

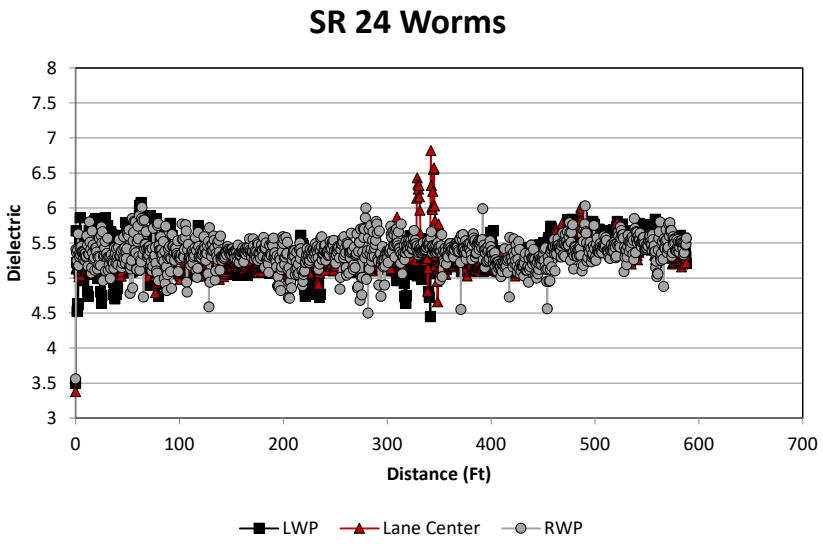

(b)

Figure 4-1. Dielectric Profiles from SR 24 (a) Control and (b) Worm Sections

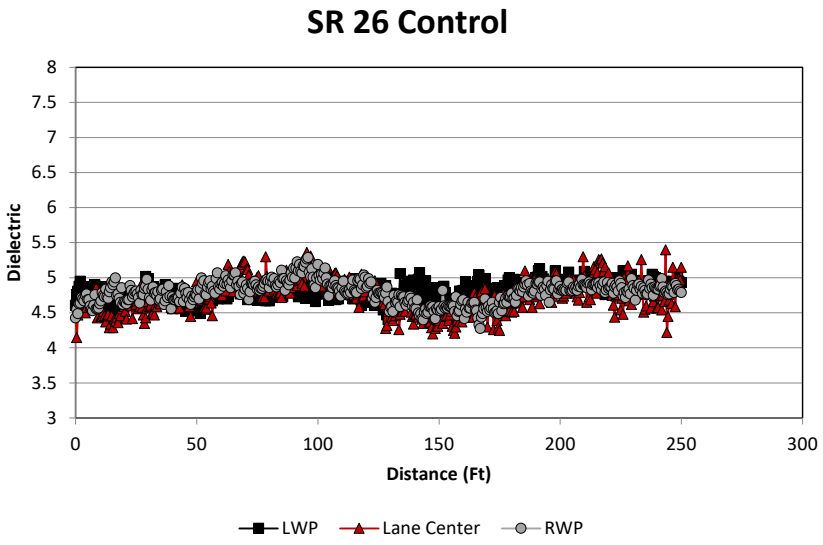

(a)

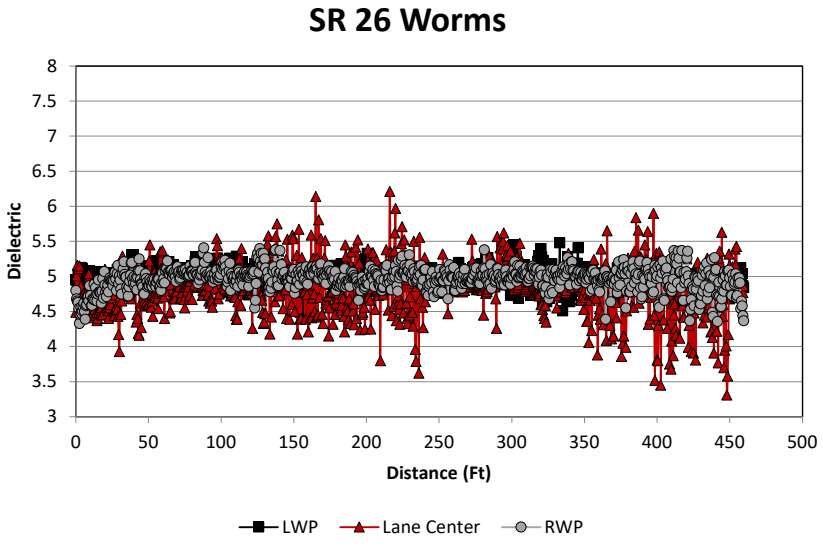

(b)

Figure 4-2. Dielectric Profiles from SR 26 (a) Control and (b) Worm Sections

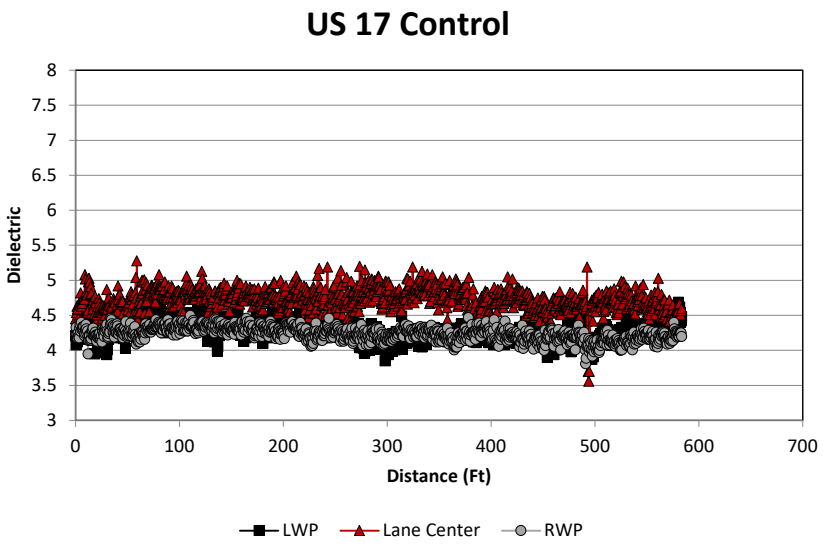

(a)

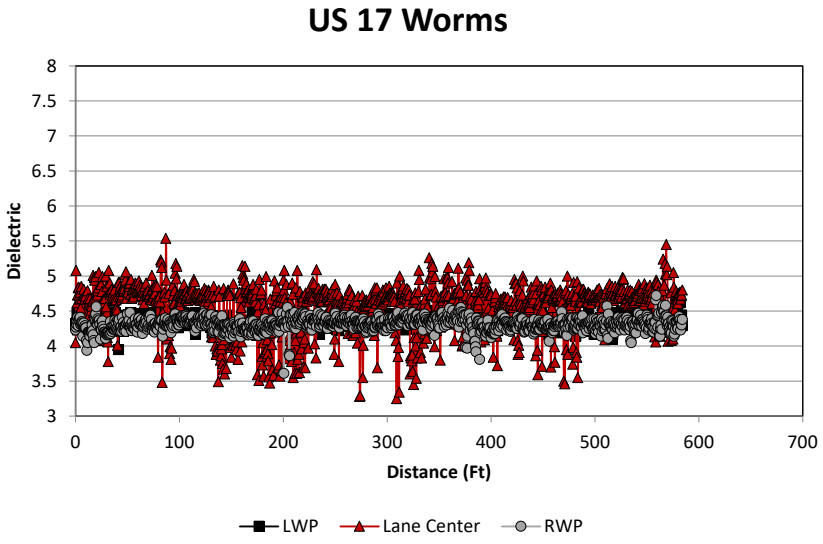

(b)

Figure 4-3. Dielectric Profiles from US 17 (a) Control and (b) Worm Sections

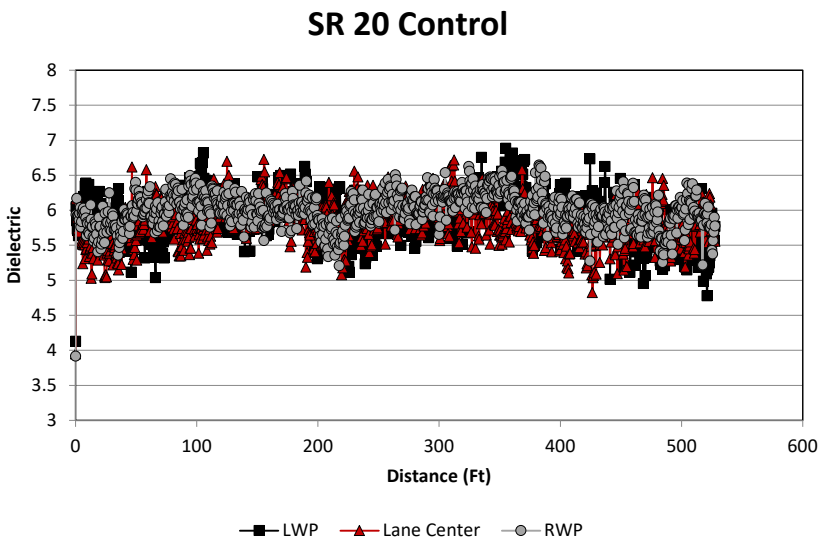

(a)

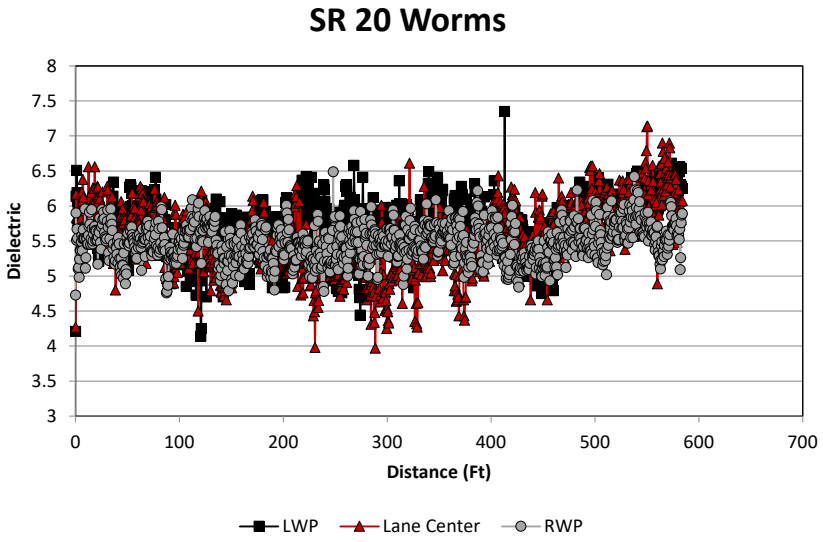

(b)

Figure 4-4. Dielectric Profiles from SR 20 (a) Control and (b) Worm Sections

Figure 4-5 shows a summary (i.e., mean and coefficient of variation [COV]) of the dielectrics obtained from the respective field sites. Figure 4-5(a) shows that higher mean dielectric values are seen in the worm sections of SR 24 and SR 26, while the trend is reversed for US 17 and SR 20. As such, the trend of the mean dielectric values is not quite conclusive. However, Figure 4-5(b) clearly shows that the worm sections generally exhibit higher variability, especially within the lane center where the asphalt was not compacted by traffic.

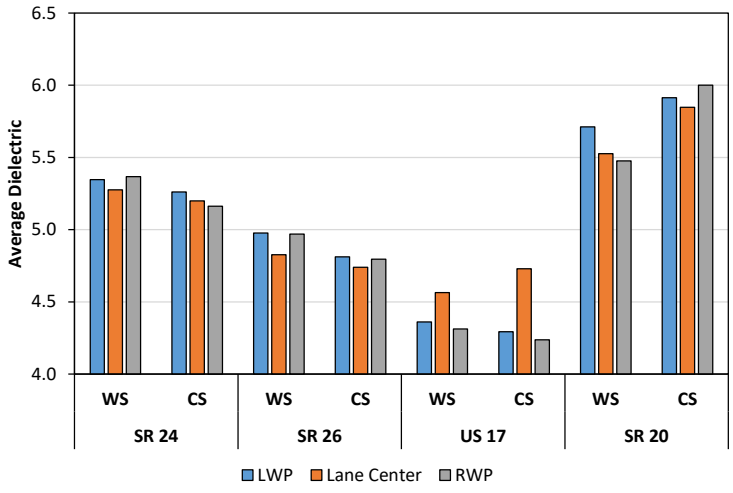

(a)

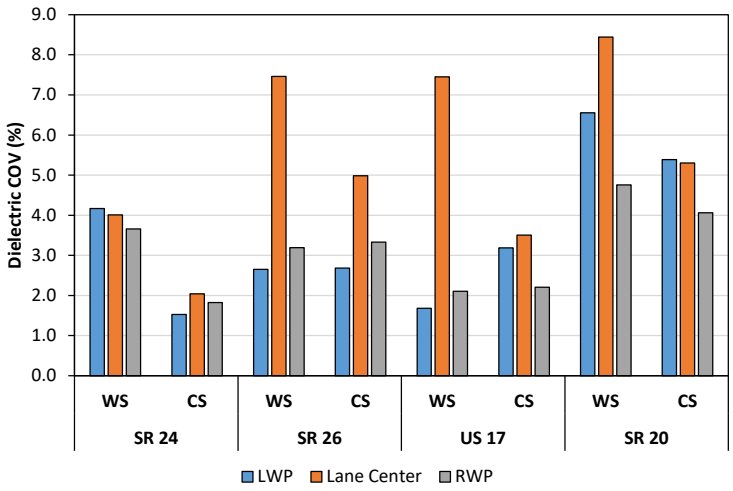

(b)

Figure 4-5. Dielectric Summaries: (a) Mean and (b) COV

4.1.2. Pavement Condition Index (PCI)

The overall PCI values for the five roadway sections evaluated in this study are presented in Figure 4-6 and range from 29 to 100. Contrary to expectations, three of the five worm sections (SR 79, US 17, and SR 20) exhibited higher PCI values than the control sections. The difference in PCI between worm and control sections was minimal and ranged from 1 to 5 PCI points on SR 79, SR 26, US 17 and SR 20. The largest difference in condition was observed between worm and control sections of SR 24, where the control section carried a PCI of 11 points greater than the worm section. The SR 24 roadway was also in the best overall condition of the five projects, according to PCI. The only distress observed in the SR 24 control section was 16 ft of low-severity longitudinal and transverse (L&T) cracking. In contrast, there was 375-ft of L&T cracking in the worm section. A total of four distress types were observed across all the projects: L&T cracking, alligator cracking, rutting, and block cracking. All block cracking and rutting observed was of low severity. Low-severity and medium-severity L&T cracking and

alligator cracking were also observed on each roadway. Histograms provided in Figure 4-7 and Figure 4-8 show the occurrence of distress types and severity over worm and control sections, respectively. Low, medium and high distress severities are indicated by “L”, “M”, and “H” designations on the x-axis. Table 4-1 provides a key for referencing distress codes. These data show that the same distresses generally occurred in both worm and control sections. Two exceptions were the occurrence of low-severity block cracking in the SR 26 worm section, where the control section did not exhibit block cracking, and the occurrence of medium-severity L&T cracking in worm sections on SR 24 and US 17, where the control sections only exhibited low-severity L&T cracks.

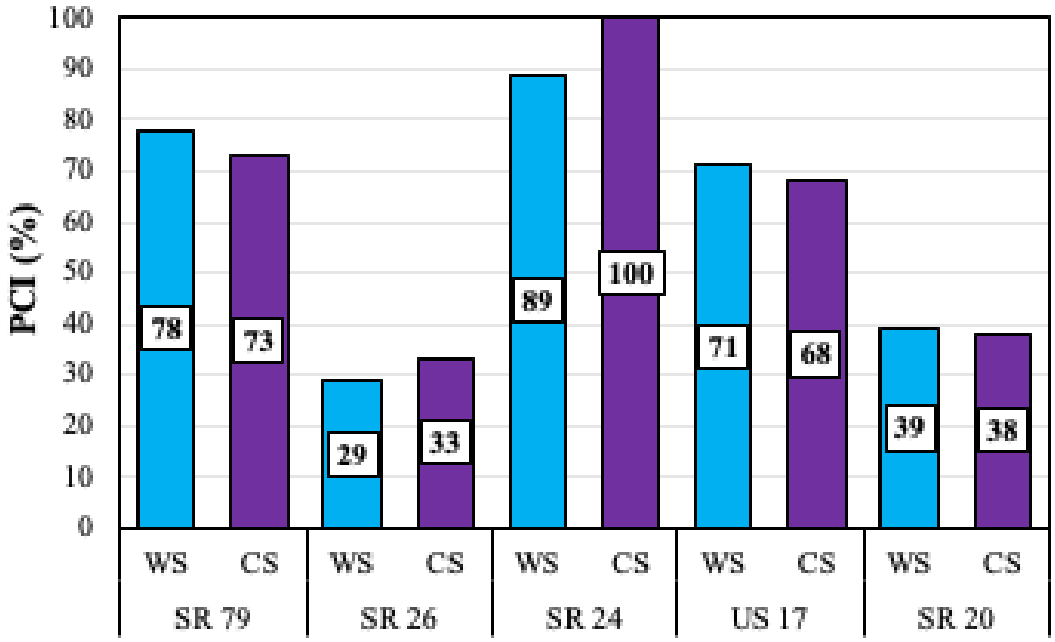

Figure 4-6. Overall PCI

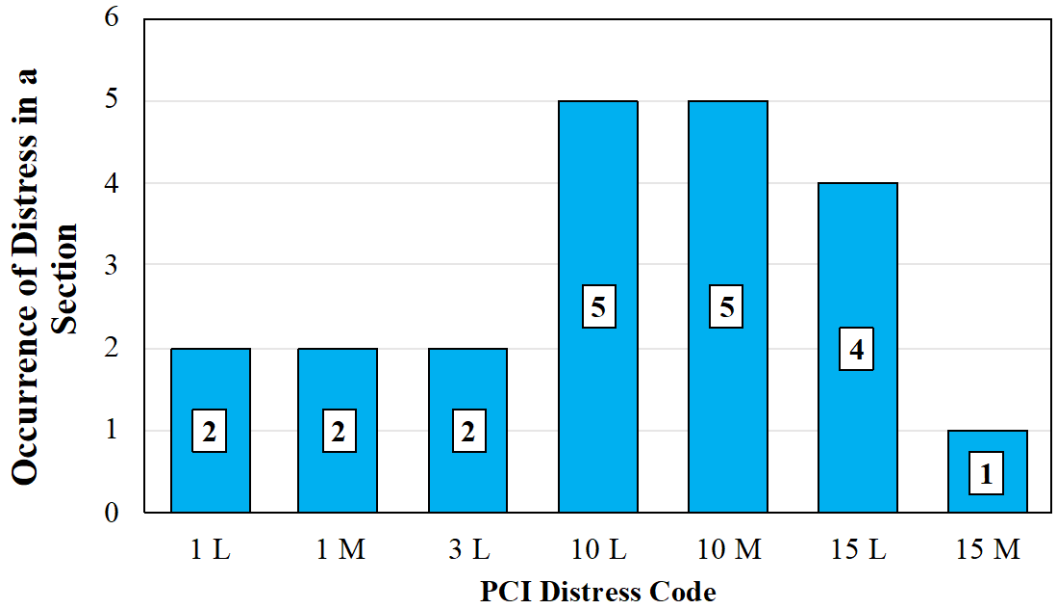

Figure 4-7. Worm Section Distress Occurrence

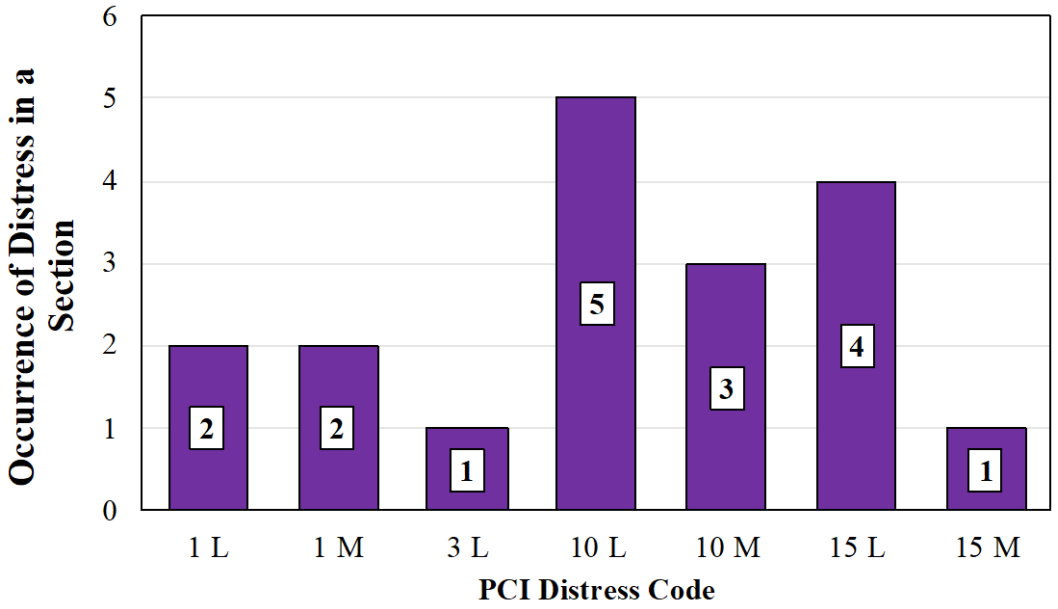

Figure 4-8. Control Section Distress Occurrence

Table 4-1. PCI Distress Codes

Code	Distress
1	Alligator Cracking
3	Block Cracking
10	L&T cracking
15	Rutting

Area weighted quantities of L&T cracking, alligator cracking, rutting, and block cracking were computed and compared to assess possible association between the occurrence of individual distress types and worm distress. Conglomerations of surface cracking distress may indicate whether worm or control pavements are more subject to water intrusion through cracks, thus potentially creating a greater opportunity for the development of worm distress. The area weighted L&T cracking was computed by taking the quotient of the total linear feet of cracking measured on a section and the section area. The area weighted averages for block cracking and alligator cracking were computed the same way; however, the numerator of each quotient was the area of distress observed in each section.

Area weighted averages for L&T cracking, block cracking, and alligator cracking are provided in Figure 4-9, Figure 4-10, and Figure 4-11, respectively. Low- and medium-severity distress quantities were combined for these computations. These figures show the occurrence of block cracking and alligator cracking was not consistent across each site and may not be a major contributing factor to the occurrence of worm distress. The rate of L&T cracking observed on the control sections of SR 24 and US 17 was considerably minimal. Taken together, the absence of worm distress in the control sections of SR 24 and US 17 may have an association with the absence of surface cracking. A possible interpretation of this finding is that cracking may be a prerequisite for the mechanism(s) causing worm distress. Control sections for SR 79, SR 26, and SR 20 all exhibit as much or more cracking than the worm sections; therefore, L&T cracking is not sufficient to cause blistering but may be necessary.

Rutting was also computed as an area weighted average and is provided in Figure 4-12. No rutting occurred on SR 24. Rutting was considerably greater in the control section of SR 20, which is supported by higher air voids measured and presented in Section 4.2.3. Rutting was not consistently higher or lower in worm sections on the remaining three projects and does not appear to be associated with worm distress.

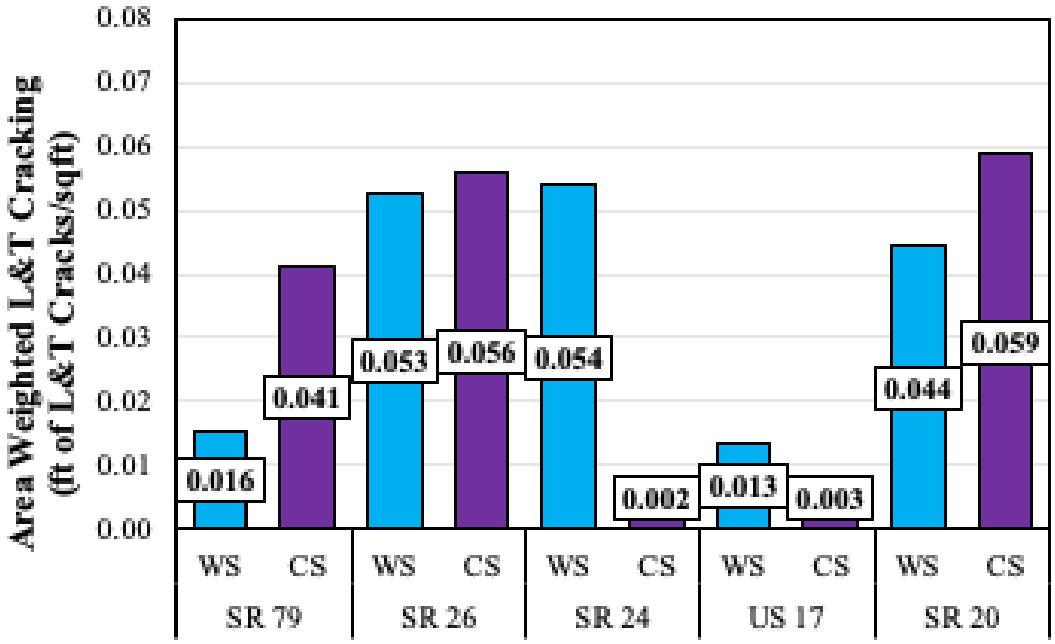

Figure 4-9. Area Weighted L&T Cracking

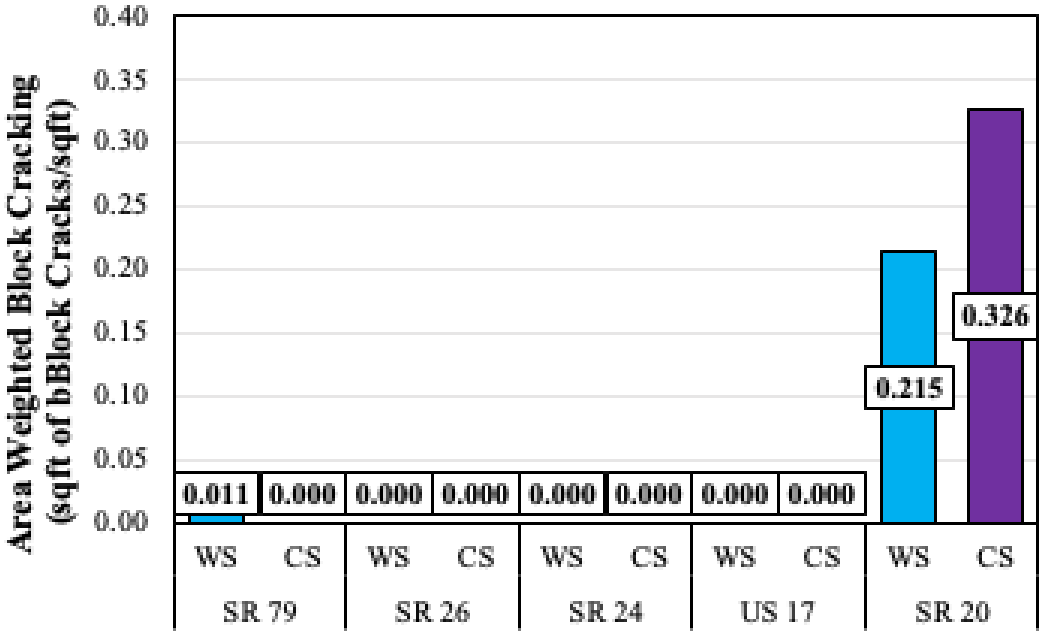

Figure 4-10. Area Weighted Block Cracking

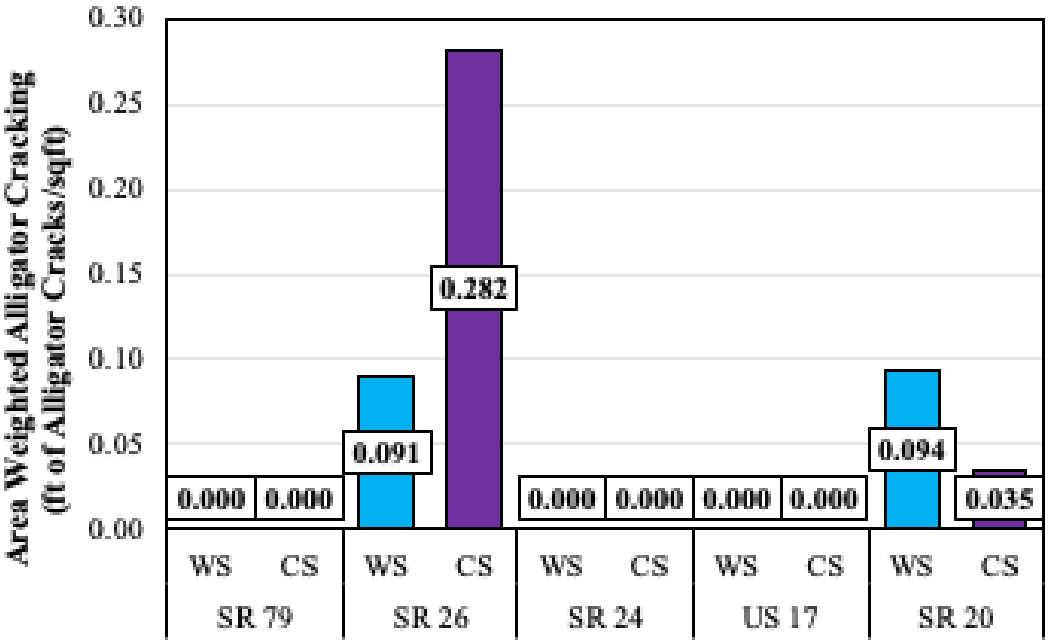

Figure 4-11. Area Weighted Alligator Cracking

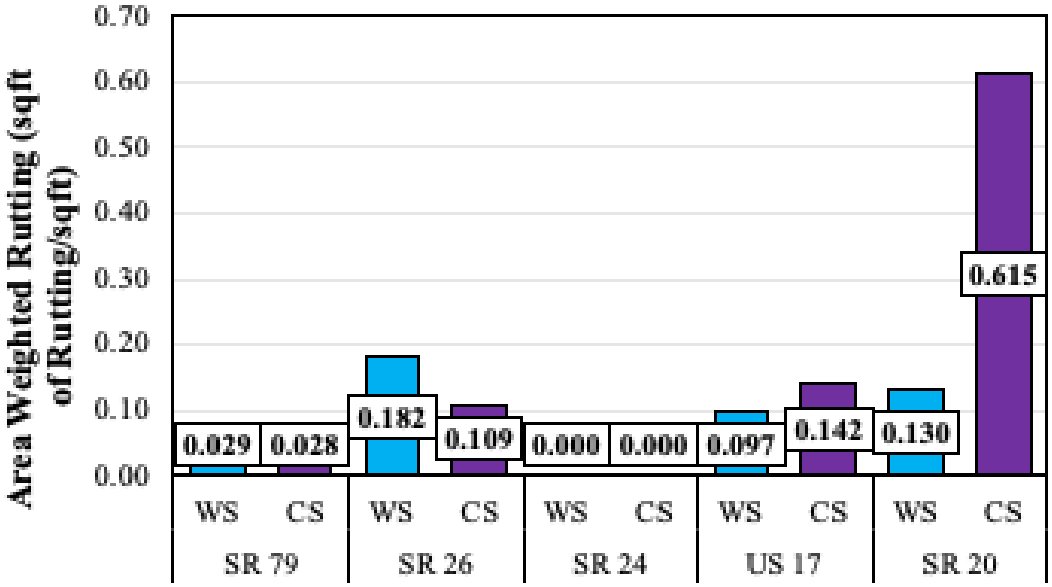

Figure 4-12. Area Weighted Rutting

4.1.3. Falling Weight Deflectometer (FWD)

The primary purpose of the FWD testing was to back calculate the modulus of AC, base, and subgrade layers. Back calculation was carried out using ViscoWave [29], which is a finite layer model capable of simulating the dynamic (i.e., time- or frequency-dependent) response of a flexible pavement. It models the AC layers as an elastic material or a viscoelastic material whose properties depend on time (or frequency) of loading and temperature of the material.

For back calculation purposes, each pavement was modeled as a structure consisting of the following five layers:

1. Top lift AC whose thickness was obtained as the average thickness from the field cores. This layer was modeled as a viscoelastic layer (i.e., frequency dependent). A constant Poisson's ratio 0.35 and a constant unit weight of 145 pcf were used for all sections analyzed. The dynamic modulus of this layer was backcalculated using ViscoWave.
2. An interface layer having a thickness of 0.01 in., a Poisson's ratio of 0.0, and a unit weight of 10 pcf was introduced to simulate the bond between the two AC layers. This layer was introduced to simulate the bond stiffness between the top and the bottom AC layers. This layer was modeled as a linear elastic layer (i.e., frequency independent), whose modulus was backcalculated from ViscoWave.
3. Bottom lift AC whose thickness was obtained as the average thickness from the field cores. This layer was modeled as a viscoelastic layer (i.e., frequency dependent). A constant Poisson's ratio 0.35 and a constant unit weight of 145 pcf were used for all sections analyzed. The dynamic modulus of this layer was backcalculated using ViscoWave.
4. Unbound base layer whose thickness was obtained as the average thickness from cross-section measurements obtained in 12-in diameter field core hole excavations. This layer was modeled as a linear elastic layer (i.e., frequency independent). A constant Poisson's ratio 0.4 and a constant unit weight of 125 pcf were used for all sections analyzed. The elastic modulus of this layer was backcalculated using ViscoWave.

5. Subgrade layer which was modeled as a linear elastic layer (i.e., frequency independent). A constant Poisson's ratio 0.45 and a constant unit weight of 110 pcf were used for all sections analyzed. The elastic modulus of this layer was backcalculated using ViscoWave.

One of the primary differences between ViscoWave and other traditional, static backcalculation programs (e.g., Modulus, EverCalc, etc.) is that ViscoWave uses the entire FWD load and deflection time histories for backcalculation (as opposed to peak load and peak deflections used in static programs). As an example, Figure 4-13 shows the load and deflection time histories measured by the FWD from the worm section of SR 20. The figure also shows the deflection time histories from ViscoWave at the completion of backcalculation, which shows good agreement with the measured deflection time histories.

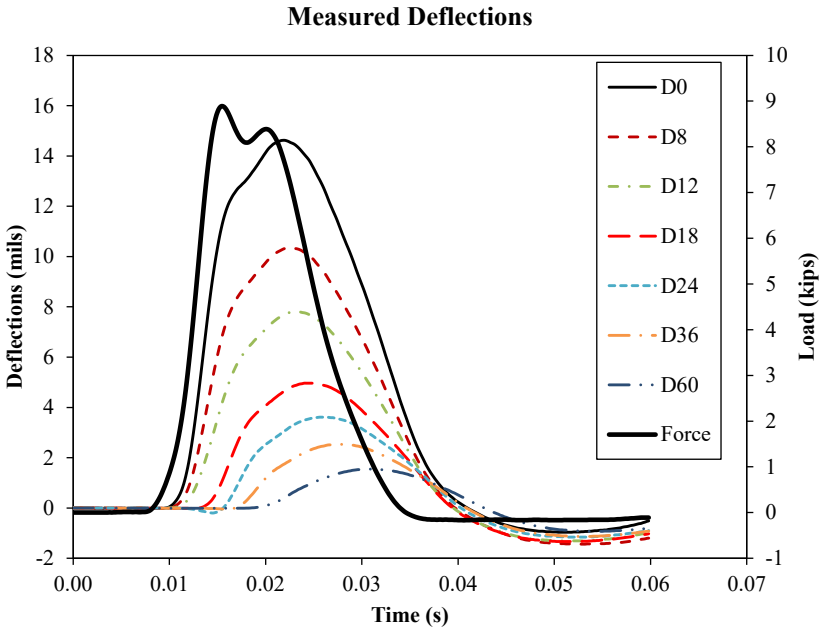

(a)

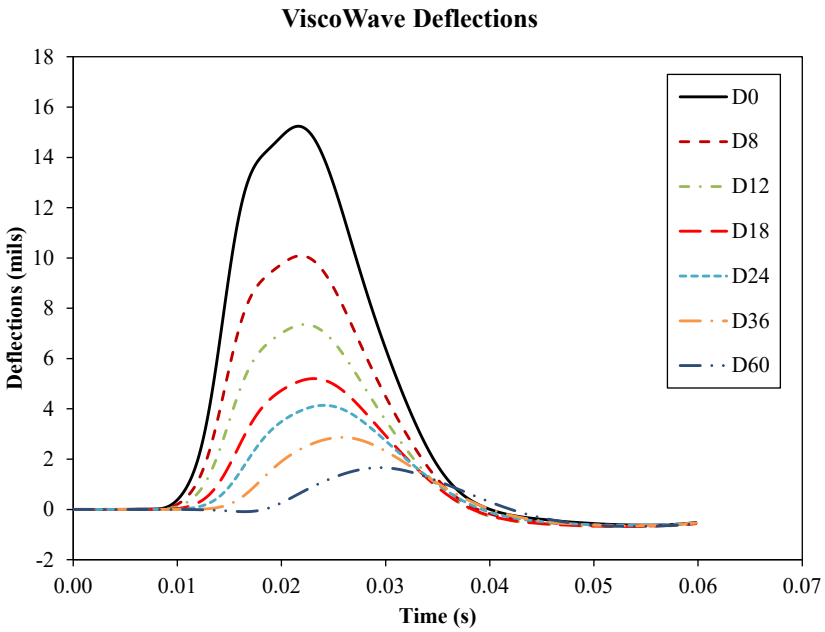

(b)

Figure 4-13. (a) Measured and (b) ViscoWave Backcalculated FWD Time Histories from SR 20 Worm Section

This section of the report presents the FWD data gathered from five test sections as well as the results from backcalculation.

4.1.3.1. Site 1 – FL SR 79

Figure 4-14, Figure 4-15, and Figure 4-16 show the raw FWD deflections under the 9,000-lb target load, collected from the control, worm section no. 1, and worm section no. 2, respectively. These figures generally show the deflections follow relatively consistent trends within each section, indicating that no subsurface anomalies (or an abrupt pavement change) exist within these sections.

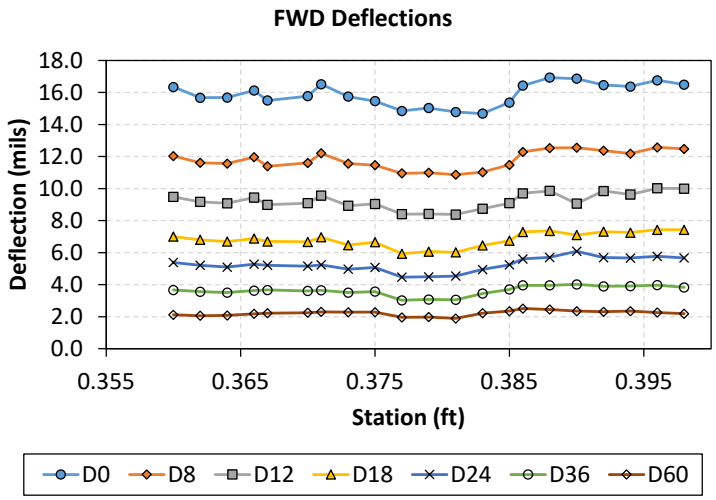

Figure 4-14. FWD Deflections from SR 79 Control Section

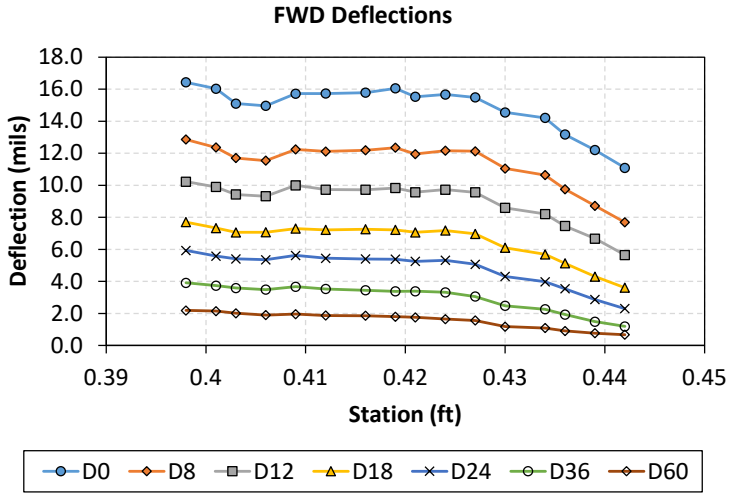

Figure 4-15. FWD Deflections from SR 79 Worm Section No. 1

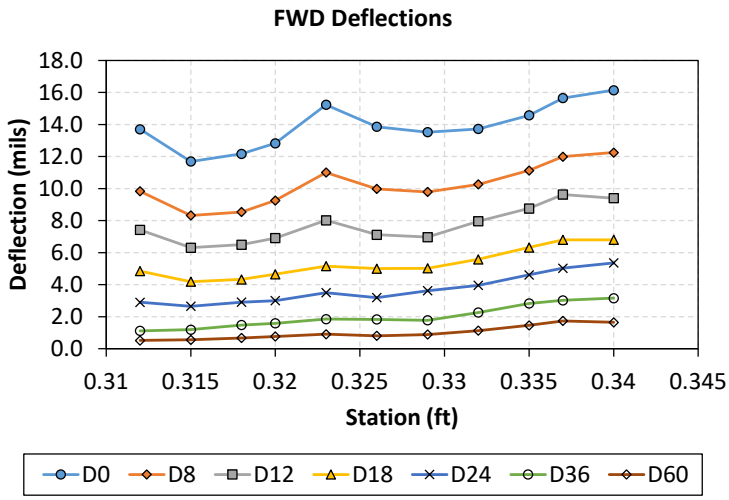

Figure 4-16. FWD Deflections from SR 79 Worm Section No. 2

Figure 4-17 shows the average deflection basins obtained from each section, with the summary statistics of the deflections, provided in Table 4-2. The figure shows that the shape of the deflection basins is relatively consistent among all three sections. Table 4-2 shows that despite the comparable average deflection basins, both worm sections exhibit higher variability as indicated by the standard deviation and COV. Worm section no. 2 showing the lowest average deflections may be attributed to a stiffer subgrade or embankment material below this particular section.

The control section also shows the highest deflections, especially for the FWD sensor directly below the load plate (D0). While such higher D0 may be attributed to a weaker AC layer, it is also possible that the pavement temperature in the control section was higher than the worm sections during the FWD testing. Higher D0 within the control section may also be attributed to weaker foundation layers (i.e., base and subgrade). Although backcalculating the dynamic modulus master curve of the AC layer and shifting the master curve to a reference temperature may allow for a fair assessment of the AC modulus, the FWD temperature sensor malfunctioned at the time of FWD testing on SR 79 and, hence, backcalculation was not conducted for the FWD data from SR 79. Instead, the AC dynamic modulus needed for the pavement performance assessment was obtained from laboratory testing of field-retrieved cores.

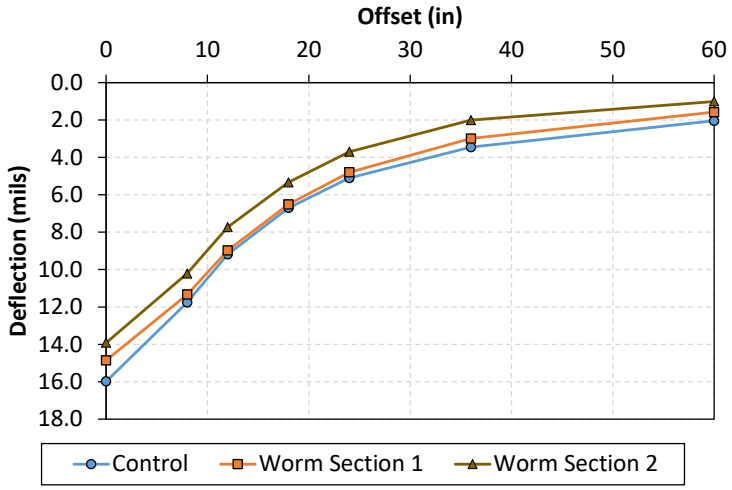

Figure 4-17. Average FWD Deflection Basins from SR 79

Table 4-2. SR 79 FWD Deflection Statistics

FWD Sensor	Control Section			Worm Sections					
				Worm Section 1			Worm Section 2		
	Avg. (mils)	Std. Dev. (mils)	COV (%)	Avg. (mils)	Std. Dev. (mils)	COV (%)	Avg. (mils)	Std. Dev. (mils)	COV (%)
D0	16.0	0.6	4.0	14.9	1.5	10.1	13.9	1.4	10.0
D8	11.8	0.5	4.4	11.3	1.5	12.8	10.2	1.3	12.6
D12	9.2	0.5	5.2	9.0	1.3	14.8	7.7	1.1	14.7
D18	6.7	0.4	6.6	6.5	1.2	18.6	5.3	0.9	17.4
D24	5.1	0.5	8.9	4.8	1.1	22.4	3.7	0.9	25.0
D36	3.5	0.4	10.9	3.0	0.8	28.4	2.0	0.7	35.6
D60	2.0	0.3	14.8	1.6	0.5	31.4	1.0	0.4	42.5

4.1.3.2. Site 2 – FL SR 26

Figure 4-18 and Figure 4-19 show the raw FWD deflections under the 9,000-lb target load, collected from the control and worm sections of SR 26, respectively. Figure 4-20 shows the average deflection basins, with the summary statistics of the deflections provided in Table 4-3. Figure 4-20 and Table 4-3 show that the average deflections from the control and the worm sections were comparable, with the worm section showing slightly higher deflections. The deflections from the worm section also show slightly higher variability (Table 4-3).

Table 4-4 summarizes the pavement surface temperature during FWD testing. The average temperatures were relatively close (i.e., a difference of only 3.0 ºF).

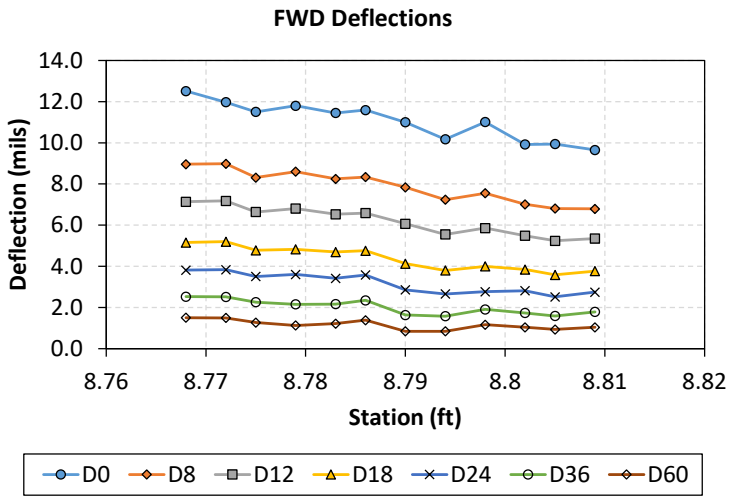

Figure 4-18. FWD Deflections from SR 26 Control Section

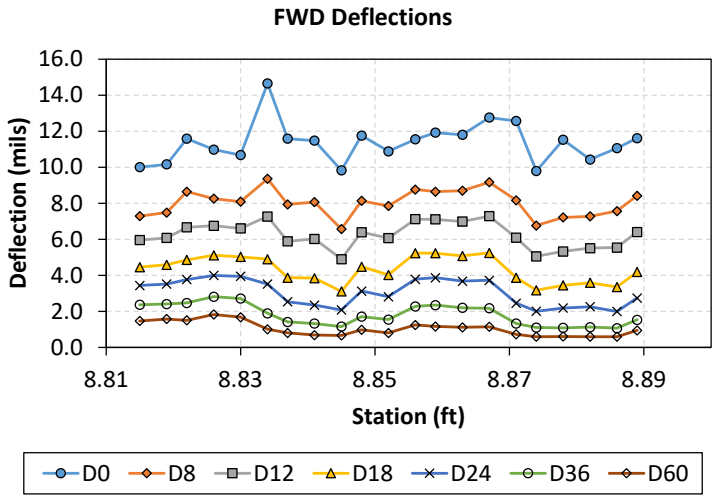

Figure 4-19. FWD Deflections from SR 26 Worm Section

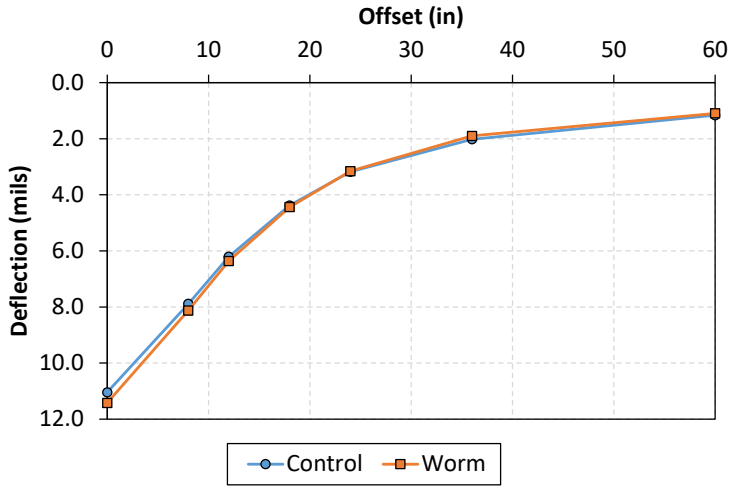

Figure 4-20. Average FWD Deflection Basins from SR 26

Table 4-3. SR 26 FWD Deflection Statistics

FWD Sensor	Control Section			Worm Section		
	Avg. (mils)	Std. Dev. (mils)	COV (%)	Avg. (mils)	Std. Dev. (mils)	COV (%)
D0	11.0	0.9	8.4	11.4	1.1	9.8
D8	7.9	0.8	10.1	8.1	0.8	9.7
D12	6.2	0.7	11.3	6.4	0.8	12.3
D18	4.4	0.6	13.3	4.4	0.8	18.0
D24	3.2	0.5	15.4	3.2	0.8	25.1
D36	2.0	0.4	17.6	1.9	0.6	33.1
D60	1.2	0.2	19.8	1.1	0.4	38.1

Table 4-4. Pavement Surface Temperature during SR 26 FWD Testing

Control Section			Worm Section		
Avg. (ºF)	Std. Dev. (ºF)	COV (%)	Avg. (ºF)	Std. Dev. (ºF)	COV (%)
76.7	0.9	1.1	79.7	5.2	6.5

Figure 4-21 and Figure 4-22 show the backcalculated AC dynamic modulus master curve shifted to a reference temperature of 50 ºF (10 ºC) for the top and the bottom AC lifts, respectively. The backcalculated dynamic modulus values of the AC layer at 10 Hz as well as the backcalculated modulus of the interface bond and the unbound layers (i.e., base and subgrade) are summarized in Table 4-5. The table clearly shows that when the AC modulus was shifted to a common reference temperature, the top AC lift within the worm section showed significantly lower modulus compared to the control section. This trend is reversed for the lower AC lift. The table also shows that the control section has a slightly stronger bond between the top and the bottom AC lifts.

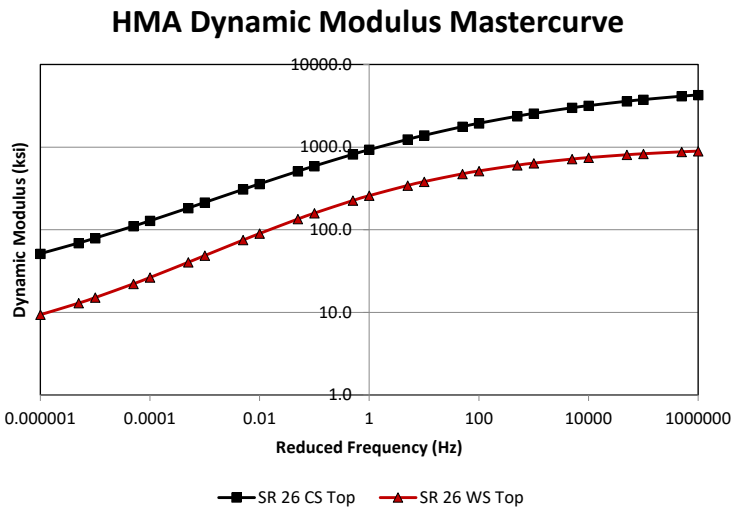

Figure 4-21. Backcalculated Dynamic Modulus Master Curves for SR 26 Top Lift AC Layer

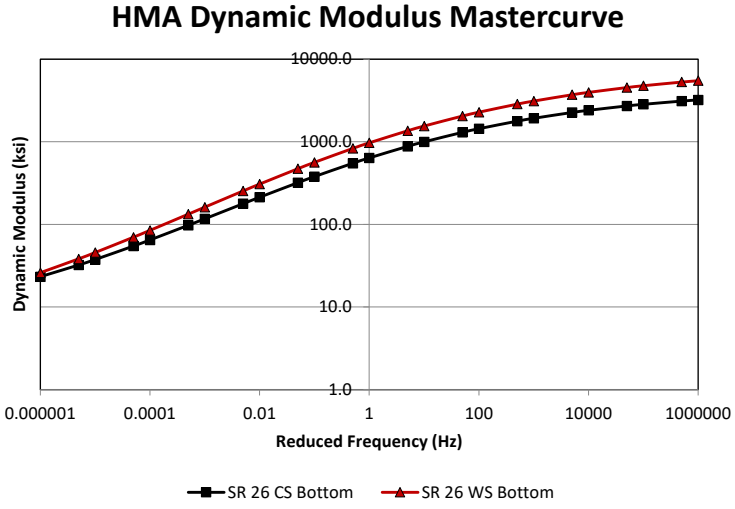

Figure 4-22. Backcalculated Dynamic Modulus Master Curves for SR 26 Bottom Lift AC Layer

Table 4-5. Summary of Backcalculated Modulus from SR 26 FWD Testing

Section	AC Modulus @ 10 Hz (ksi)				Interface Bond Modulus (ksi)	Base (ksi)	Subgrade (ksi)
	Avg. Test Temp.		Reference Temperature (50 ºF)				
	Top	Bottom	Top	Bottom			
Control	659.7	428.2	1387.0	995.9	4.2	51.8	25.3
Worms	154.9	459.1	381.8	1548.1	3.6	44.9	26.3

4.1.3.3. Site 3 – FL SR 24

Figure 4-23 and Figure 4-24 show the raw FWD deflections under the 9,000-lb target load, collected from the control and worm sections of SR 24, respectively. Figure 4-25 shows the average deflection basins, with the summary statistics of the deflections provided in Table 4-6. Figure 4-25 and Table 4-6 indicate that the worm section shows not only higher deflections, but also higher variability within the measured deflections.

Table 4-7 summarizes the pavement surface temperature during FWD testing. As seen from the table, the control section temperature was significantly higher (i.e., approximately 24 ºF higher) than the worm section temperature. In other words, the worm section showed higher deflections, despite the lower temperature. This indicates that the AC layer in the worm section may show significantly lower modulus when the AC dynamic modulus from both sections are evaluated at the same temperature.

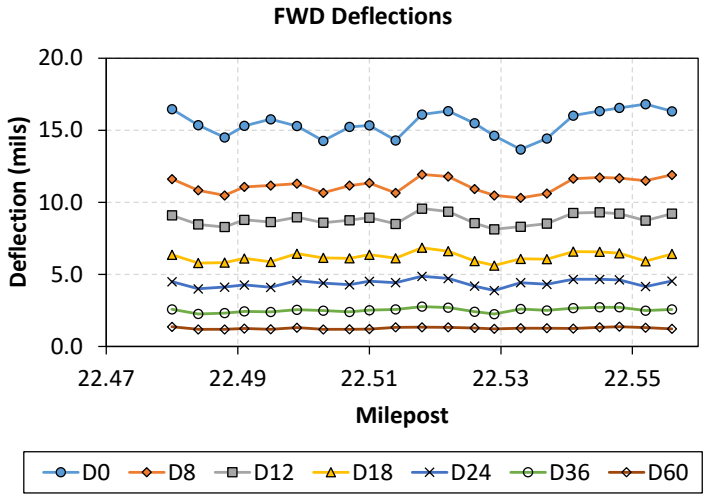

Figure 4-23. FWD Deflections from SR 24 Control Section

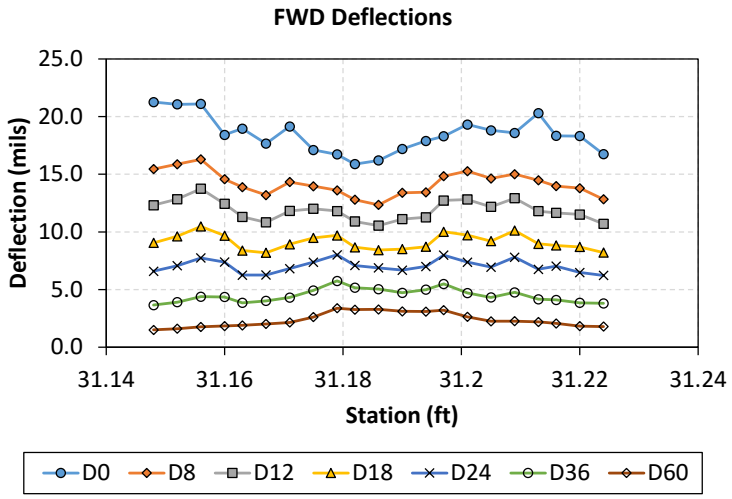

Figure 4-24. FWD Deflections from SR 24 Worm Section

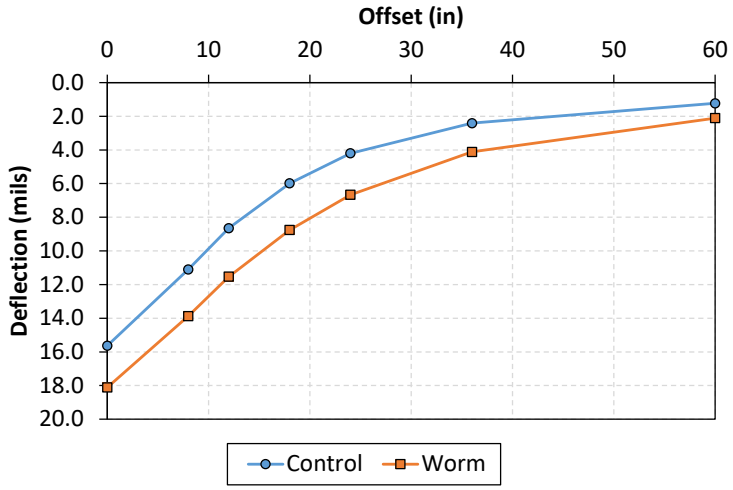

Figure 4-25. Average FWD Deflection Basins from SR 24

Table 4-6. SR 24 FWD Deflection Statistics

FWD Sensor	Control Section			Worm Section		
	Avg. (mils)	Std. Dev. (mils)	COV (%)	Avg. (mils)	Std. Dev. (mils)	COV (%)
D0	15.6	0.8	5.4	18.1	2.4	13.3
D8	11.1	0.5	4.7	13.9	1.6	11.3
D12	8.6	0.4	5.1	11.5	1.2	10.8
D18	6.0	0.4	6.4	8.8	1.0	11.3
D24	4.2	0.3	7.4	6.7	0.9	12.8
D36	2.4	0.2	7.4	4.1	0.8	19.7
D60	1.2	0.1	6.3	2.1	0.7	32.6

Table 4-7. Pavement Surface Temperature during SR 24 FWD Testing

Control Section			Worm Section		
Avg. (ºF)	Std. Dev. (ºF)	COV (%)	Avg. (ºF)	Std. Dev. (ºF)	COV (%)
104.2	1.5	1.4	80.1	0.8	1.1

Figure 4-26 and Figure 4-27 show the backcalculated AC dynamic modulus master curve shifted to a reference temperature of 50 ºF (10 ºC) for the top and the bottom AC lifts, respectively. The backcalculated dynamic modulus values of the AC layer at 10 Hz as well as the backcalculated modulus of the interface bond and the unbound layers (i.e., base and subgrade) are summarized in Table 4-8. The table clearly shows that at the respective FWD testing temperature, the AC within the worm section showed higher modulus. Nonetheless, when the AC modulus was shifted to a common reference temperature, the AC within the worm section showed significantly lower modulus. The table also shows that the control section has a significantly stronger bond between the top and the bottom AC lifts.

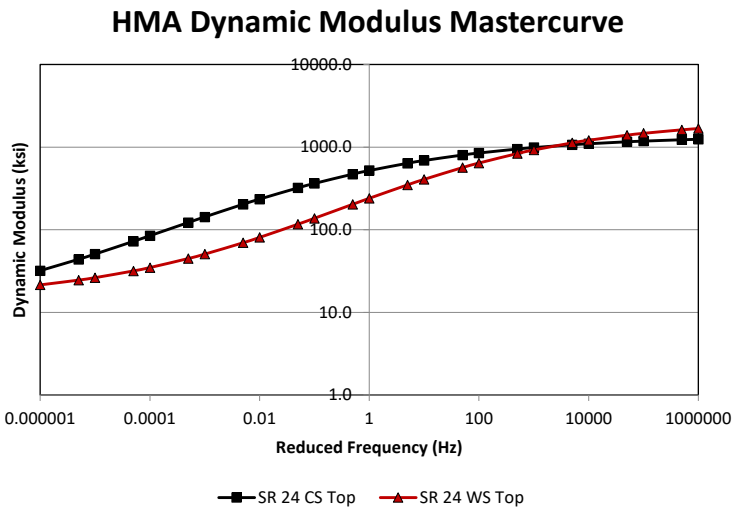

Figure 4-26. Backcalculated Dynamic Modulus Master Curves for SR 24 Top Lift AC Layer

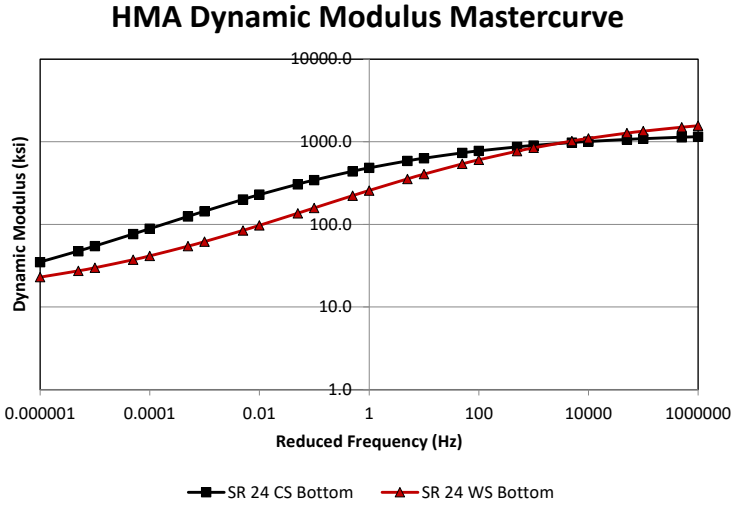

Figure 4-27. Backcalculated Dynamic Modulus Master Curves for SR 24 Bottom Lift AC Layer

Table 4-8. Summary of Backcalculated Modulus from SR 24 FWD Testing

Section	AC Modulus @ 10 Hz (ksi)				Interface Bond Modulus (ksi)	Base (ksi)	Subgrade (ksi)
	Avg. Test Temp.		Reference Temperature (50 ºF)				
	Top	Bottom	Top	Bottom			
Control	87.5	93.1	689.8	632.6	49.0	29.6	19.6
Worms	131.3	151.4	407.7	406.1	2.1	36.6	9.8

4.1.3.4. Site 4 – FL US 17

Figure 4-28 and Figure 4-29 show the raw FWD deflections under the 9,000-lb target load collected from the control and worm sections of US 17, respectively. Figure 4-30 shows the average deflection basins, with the summary statistics of the deflections provided in Table 4-9. Figure 4-30 and Table 4-9 show that the average deflections from the control and the worm sections were comparable, with the worm section showing higher variability within the deflections.

Table 4-4 summarizes the pavement surface temperature during FWD testing. The average temperatures were relatively close to each other (i.e., a difference of only 5.7 ºF).

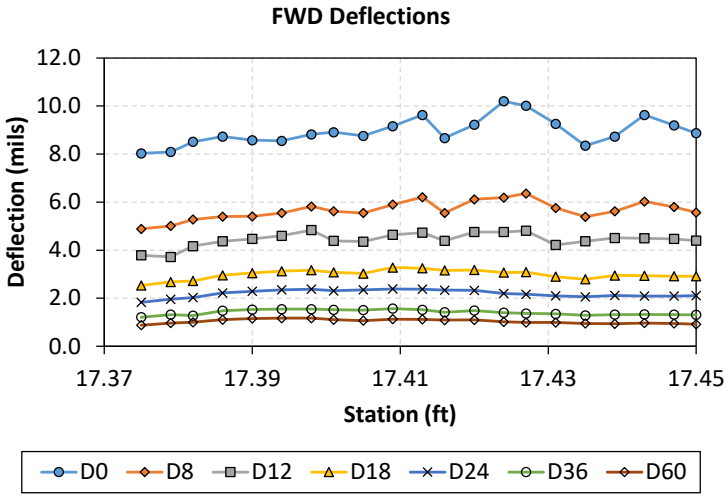

Figure 4-28. FWD Deflections from US 17 Control Section

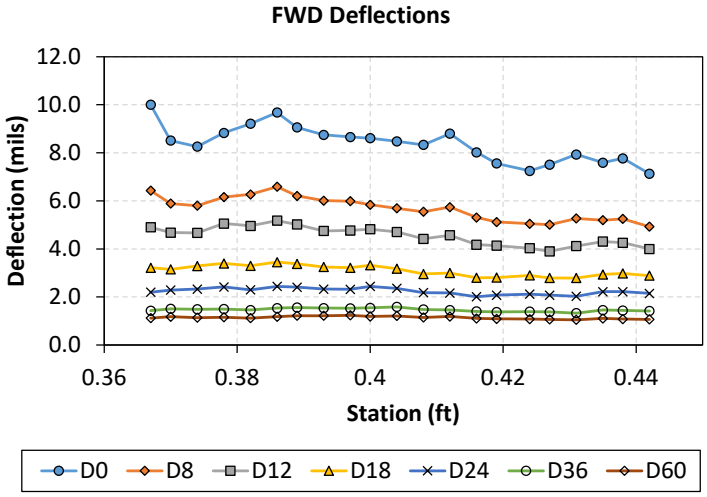

Figure 4-29. FWD Deflections from US 17 Worm Section

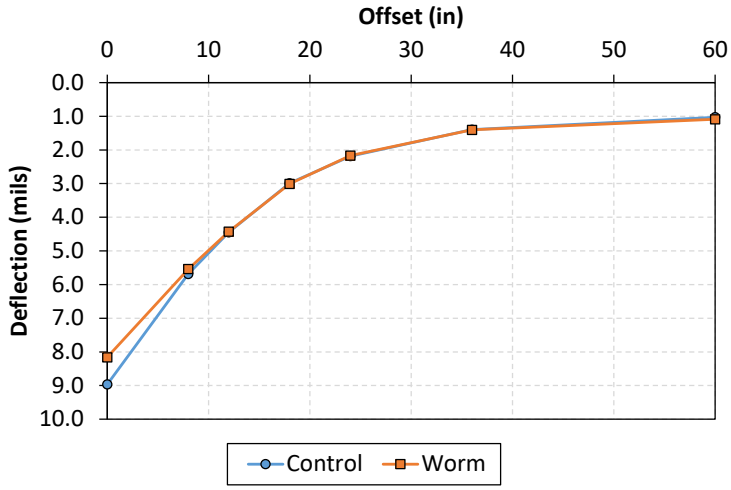

Figure 4-30. Average FWD Deflection Basins from US 17

Table 4-9. US 17 FWD Deflection Statistics

FWD Sensor	Control Section			Worm Section		
	Avg. (mils)	Std. Dev. (mils)	COV (%)	Avg. (mils)	Std. Dev. (mils)	COV (%)
D0	9.0	0.5	5.8	8.2	0.8	10.4
D8	5.7	0.3	6.1	5.5	0.6	10.2
D12	4.4	0.3	5.9	4.4	0.4	10.1
D18	3.0	0.2	5.7	3.0	0.3	10.1
D24	2.2	0.1	6.5	2.2	0.2	11.2
D36	1.4	0.1	7.3	1.4	0.2	13.0
D60	1.0	0.1	8.1	1.1	0.1	12.7

Table 4-10. Pavement Surface Temperature during US 17 FWD Testing

Control Section			Worm Section		
Avg. (ºF)	Std. Dev. (ºF)	COV (%)	Avg. (ºF)	Std. Dev. (ºF)	COV (%)
76.1	0.7	0.9	81.8	0.7	0.8

Figure 4-31 and Figure 4-32 show the backcalculated AC dynamic modulus master curve shifted to a reference temperature of 50 ºF (10 ºC) for the top and the bottom AC lifts, respectively. The backcalculated dynamic modulus values of the AC layer at 10 Hz as well as the backcalculated modulus of the interface bond and the unbound layers (i.e., base and subgrade) are summarized in Table 4-11. The table clearly shows that when the AC modulus was shifted to a common reference temperature, both the top and bottom AC lifts within the worm section showed lower modulus compared to the control section. The modulus of the interface bond and the unbound layers were comparable to each other.

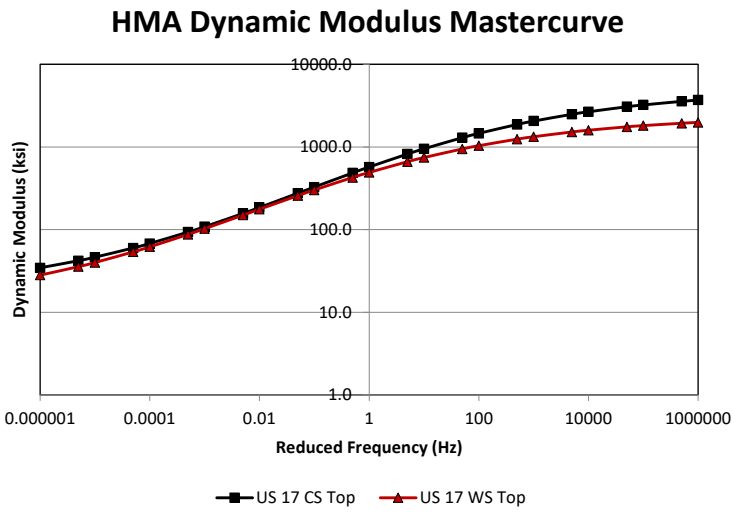

Figure 4-31. Backcalculated Dynamic Modulus Master Curves for US 17 Top Lift AC Layer

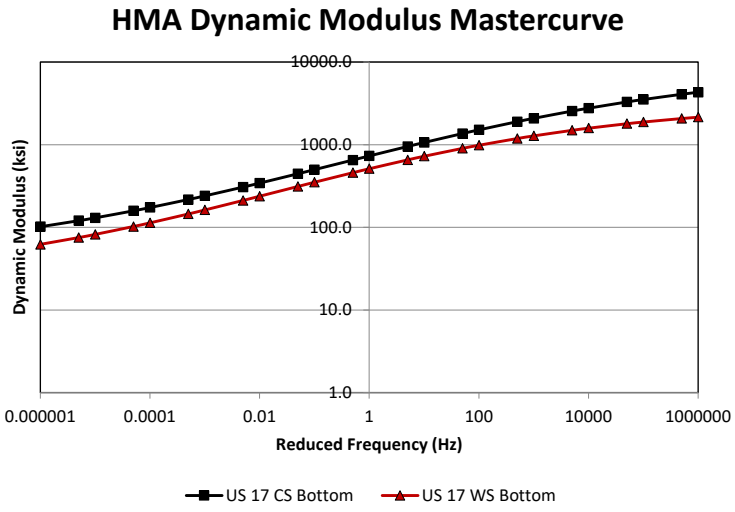

Figure 4-32. Backcalculated Dynamic Modulus Master Curves for US 17 Bottom Lift AC Layer

Table 4-11. Summary of Backcalculated Modulus from US 17 FWD Testing

Section	AC Modulus @ 10 Hz (ksi)				Interface Bond Modulus (ksi)	Base (ksi)	Subgrade (ksi)
	Avg. Test Temp.		Reference Temperature (50 ºF)				
	Top	Bottom	Top	Bottom			
Control	386.0	553.3	952.5	1062.7	2.1	69.9	36.2
Worms	263.3	318.7	744.7	725.7	2.0	70.6	36.0

4.1.3.5. Site 5 – FL SR 20

Figure 4-33 and Figure 4-34 show the raw FWD deflections under the 9,000-lb target load, collected from the control and worm sections of SR 20, respectively. Figure 4-35 shows the average deflection basins, with the summary statistics of the deflections provided in Table 4-12. Figure 4-35 and Table 4-12 indicate that the worm section shows not only higher deflections, but also higher variability within the measured deflections.

Table 4-13 summarizes the pavement surface temperature during FWD testing. As seen from the table, the control section was under higher temperature (i.e., approximately 12 ºF higher) than the worm section. In other words, the worm section showed higher deflections, despite the lower temperature. This indicates that the AC layer in the worm section may show significantly lower modulus when the AC dynamic modulus from both sections are evaluated at the same temperature.

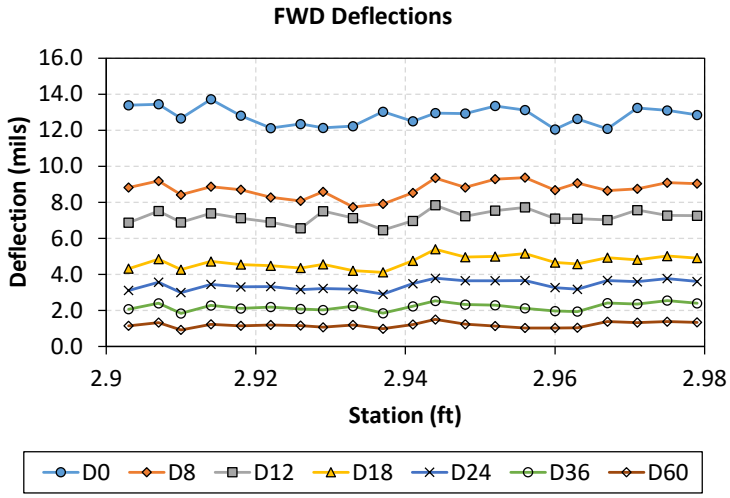

Figure 4-33. FWD Deflections from SR 20 Control Section

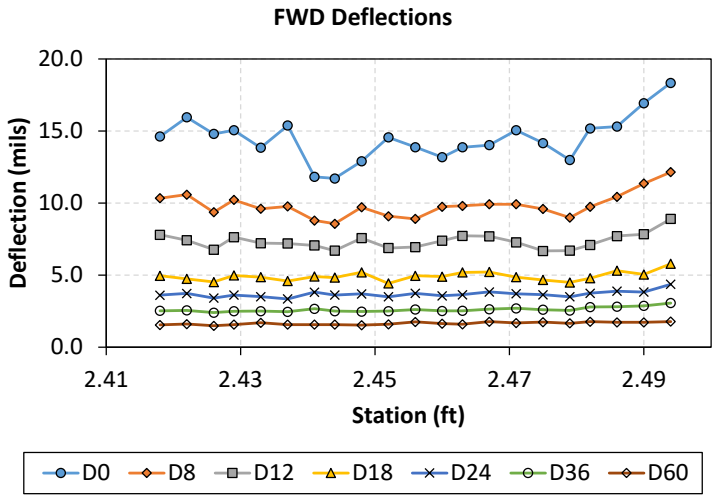

Figure 4-34. FWD Deflections from SR 20 Worm Section

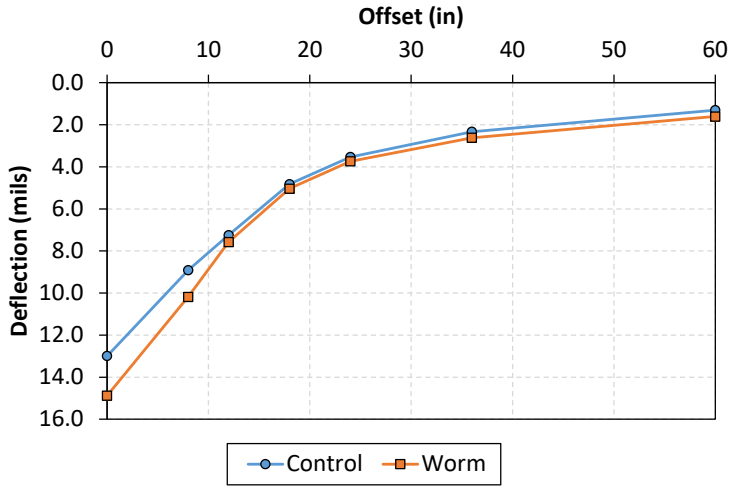

Figure 4-35. Average FWD Deflection Basins from SR 20

Table 4-12. SR 20 FWD Deflection Statistics

FWD Sensor	Control Section			Worm Section		
	Avg. (mils)	Std. Dev. (mils)	COV (%)	Avg. (mils)	Std. Dev. (mils)	COV (%)
D0	13.0	0.7	5.4	14.9	1.7	11.3
D8	8.9	0.6	7.0	10.2	1.1	10.5
D12	7.2	0.4	5.3	7.6	0.7	8.8
D18	4.8	0.4	8.9	5.0	0.4	7.6
D24	3.5	0.4	10.9	3.7	0.2	6.6
D36	2.3	0.3	14.9	2.6	0.2	5.8
D60	1.3	0.3	22.0	1.6	0.1	7.1

Table 4-13. Pavement Surface Temperature during SR 20 FWD Testing

Control Section			Worm Section		
Avg. (ºF)	Std. Dev. (ºF)	COV (%)	Avg. (ºF)	Std. Dev. (ºF)	COV (%)
65.3	1.8	2.7	53.4	1.6	3.0

Figure 4-36 and Figure 4-37 show the backcalculated AC dynamic modulus master curve shifted to a reference temperature of 50 ºF (10 ºC) for the top and the bottom AC lifts, respectively. The backcalculated dynamic modulus values of the AC layer at 10 Hz as well as the backcalculated modulus of the interface bond and the unbound layers (i.e., base and subgrade) are summarized in Table 4-14. The table clearly shows that at the respective FWD testing temperature, the modulus of the AC was comparable between the control and the worm section. Nonetheless, when the AC modulus was shifted to a common reference temperature, the AC within the worm section showed significantly lower modulus for the top lift.

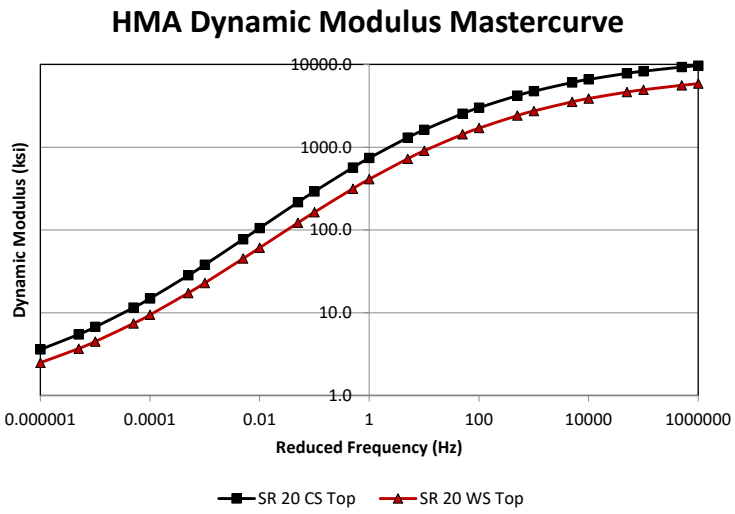

Figure 4-36. Backcalculated Dynamic Modulus Master Curves for SR 20 Top Lift AC Layer

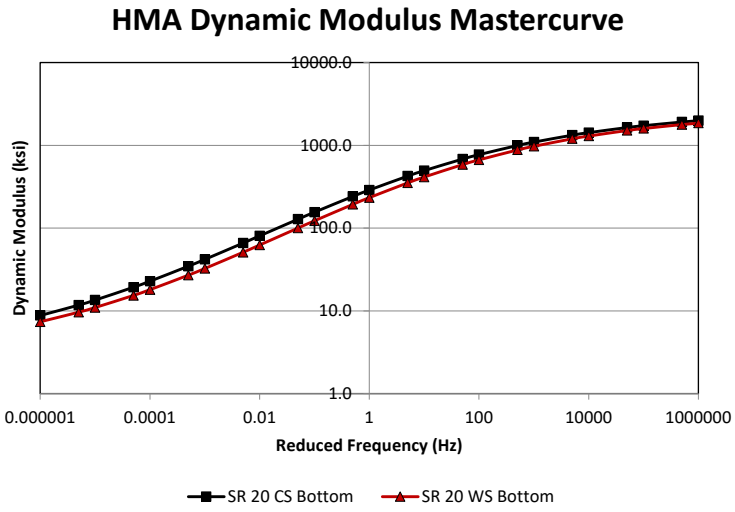

Figure 4-37. Backcalculated Dynamic Modulus Master Curves for SR 20 Bottom Lift AC Layer

Table 4-14. Summary of Backcalculated Modulus from SR 20 FWD Testing

Section	AC Modulus @ 10 Hz (ksi)				Interface Bond Modulus (ksi)	Base (ksi)	Subgrade (ksi)
	Avg. Test Temp.		Reference Temperature (50 ºF)				
	Top	Bottom	Top	Bottom			
Control	842.0	315.9	1623.1	495.8	0.8	52.2	19.5
Worms	810.7	382.0	904.6	414.6	0.2	55.9	18.0

4.1.3.6. FWD Backcalculation Summary

Figure 4-38 shows the average backcalculated dynamic modulus of the top lift AC for all sections. Note that these dynamic modulus values correspond to 10 Hz at a reference temperature of 50 ºF. Although the modulus values span a wide range, the figure clearly shows that the worm sections exhibit lower modulus compared to their control counterparts. The reduction in modulus ranges from 21.8% (from US 17) to 72.5% (from SR 26).

Similarly, Figure 4-39 shows the average backcalculated dynamic modulus (at 10 Hz and at 50 ºF) of the bottom lift AC for all sections. With the exception of SR 26, the worm sections showed lower dynamic modulus compared to the control sections, with the reduction ranging from 16.4% (from SR 20) to 35.8% (from SR 24).

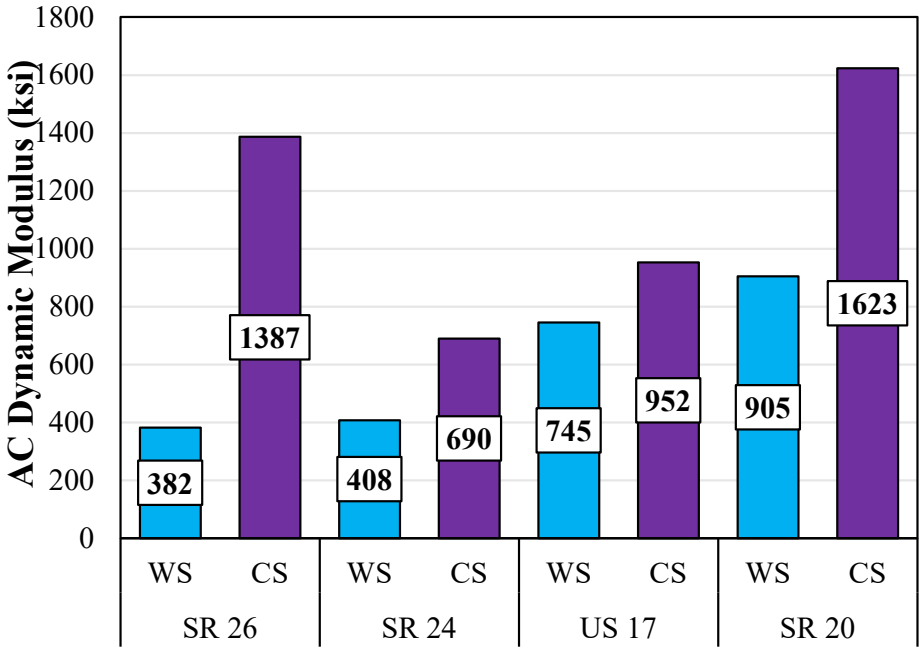

Figure 4-38. FWD Backcalculated Dynamic Modulus of Top Lift AC at 50ºF and 10 Hz

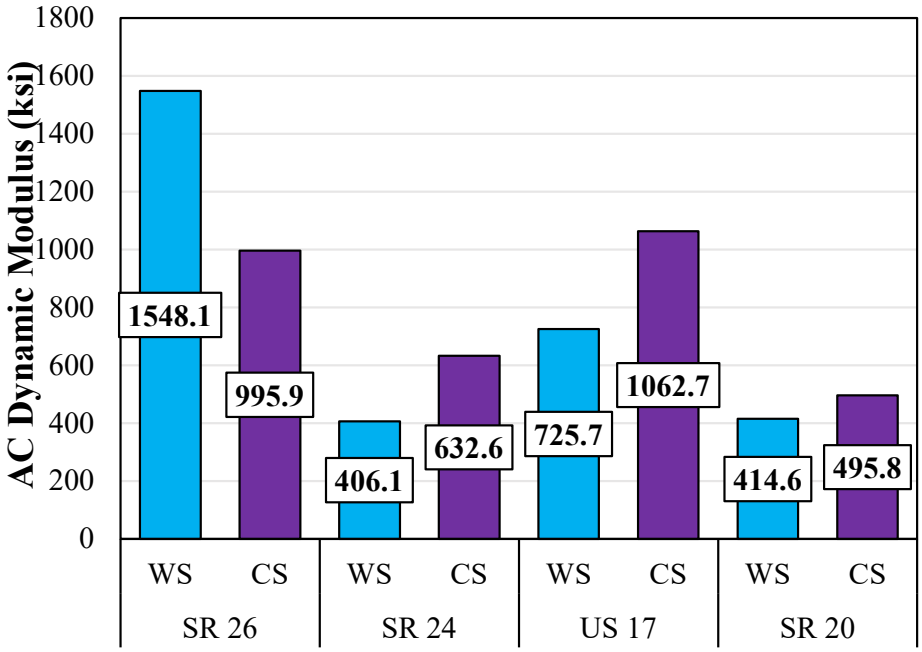

Figure 4-39. FWD Backcalculated Dynamic Modulus of Bottom Lift AC at 50ºF and 10 Hz

The interface bond moduli backcalculated from the FWD data are summarized in Figure 4-40. The figure clearly shows that with the exception of SR 24, the worm sections generally exhibit lower bond modulus, although the difference is believed to be negligible. Additional characterization of the SR 24 layer interface is further discussed in Section 4.2.1.5 and Section 4.2.5.

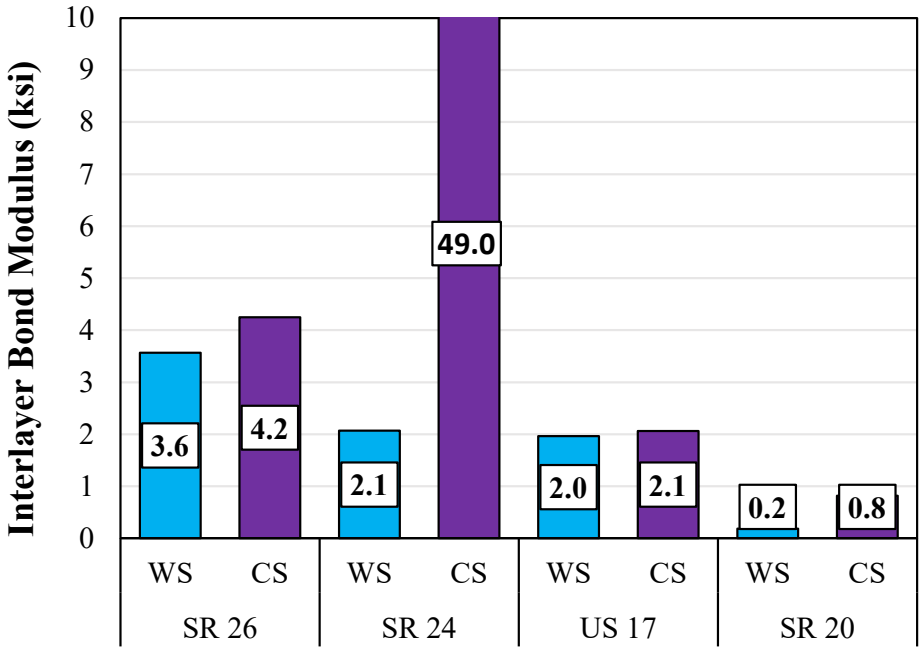

Figure 4-40. FWD Backcalculated Interface Bond Modulus

Figure 4-41 and Figure 4-42 show the backcalculated modulus of the base and subgrade layers, respectively. In general, these results indicate that the unbound layers within each site are relatively consistent.

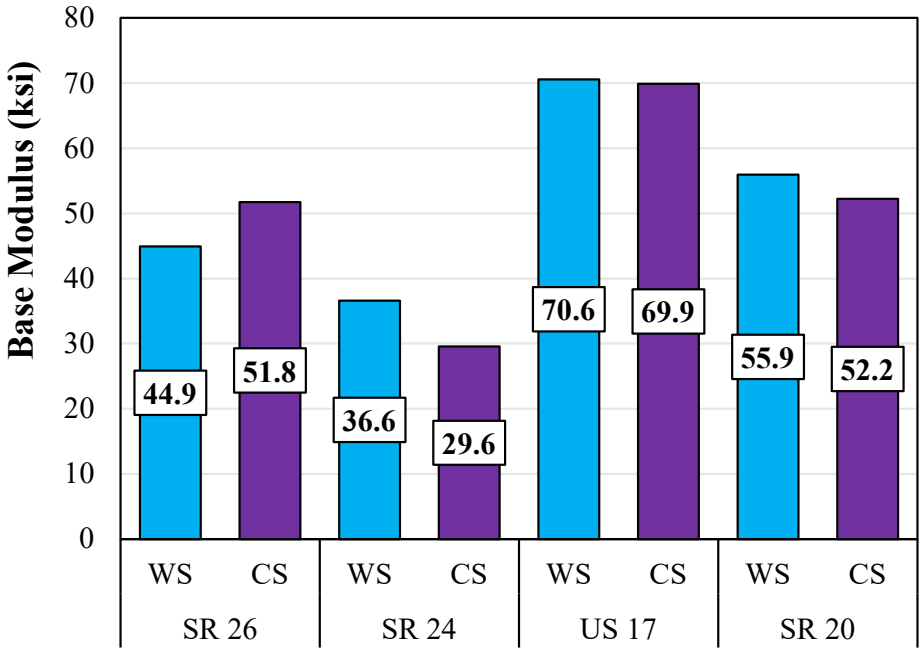

Figure 4-41. FWD Backcalculated Base Modulus

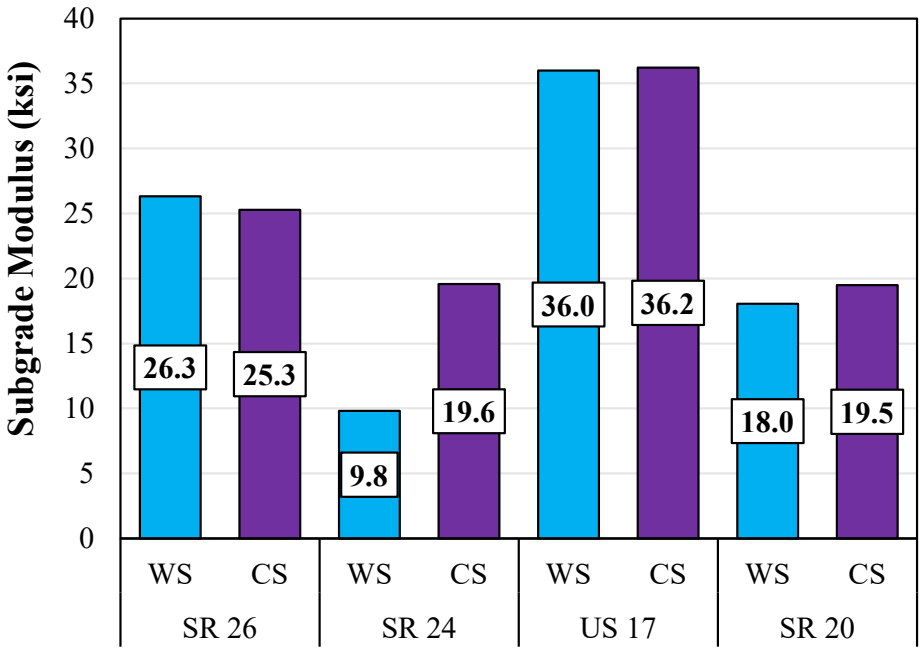

Figure 4-42. FWD Backcalculated Subgrade Modulus

4.1.4. Dynamic Cone Penetrometer (DCP)

Figure 4-43 through Figure 4-45 show the CBR values obtained from DCP testing for base, subgrade, and embankment layers, respectively. A cursory comparison between Figure 4-43 and Figure 4-41 shows that the FWD backcalculated base moduli are in good agreement with the CBR values derived from DCP testing. More specifically, both results indicated that US 17 exhibited the strongest base, while SR 24 exhibited the weakest base. The CBR derived from DCP testing (Figure 4-44) were in good agreement with the FWD backcalculated subgrade modulus (Figure 4-42).

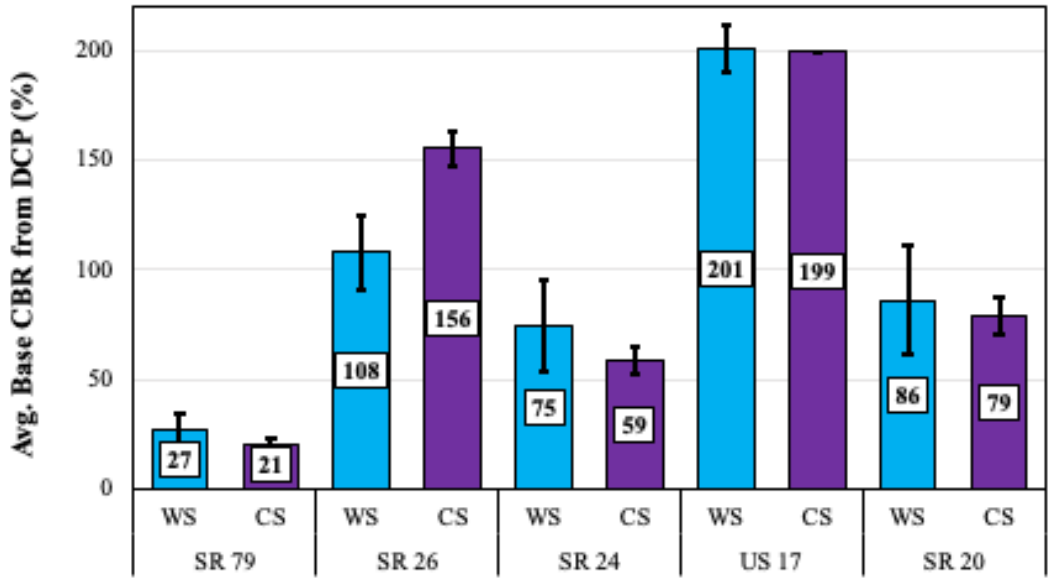

Figure 4-43. Average Base CBR from DCP

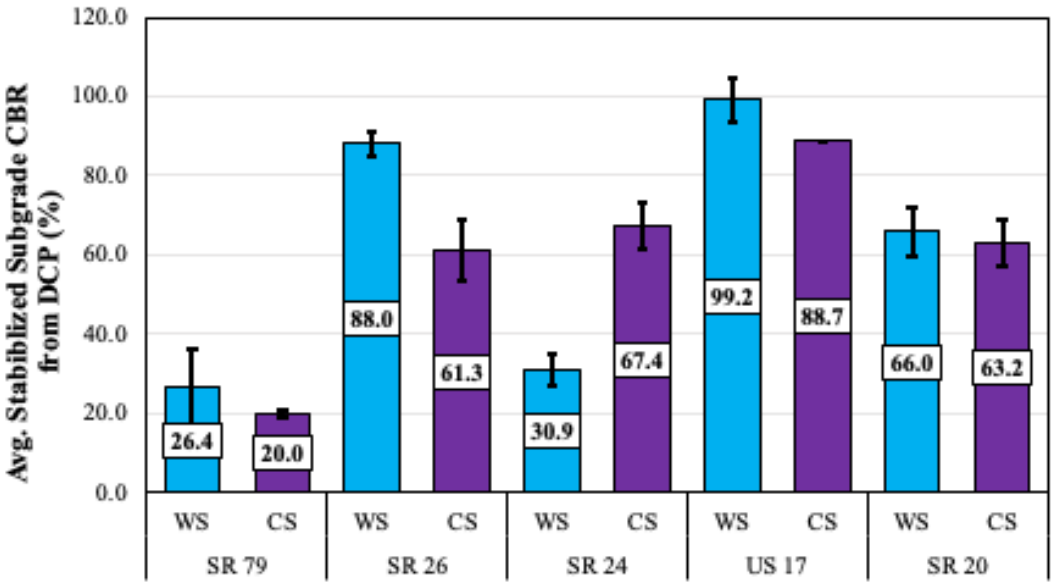

Figure 4-44. Average Stabilized Subgrade CBR from DCP

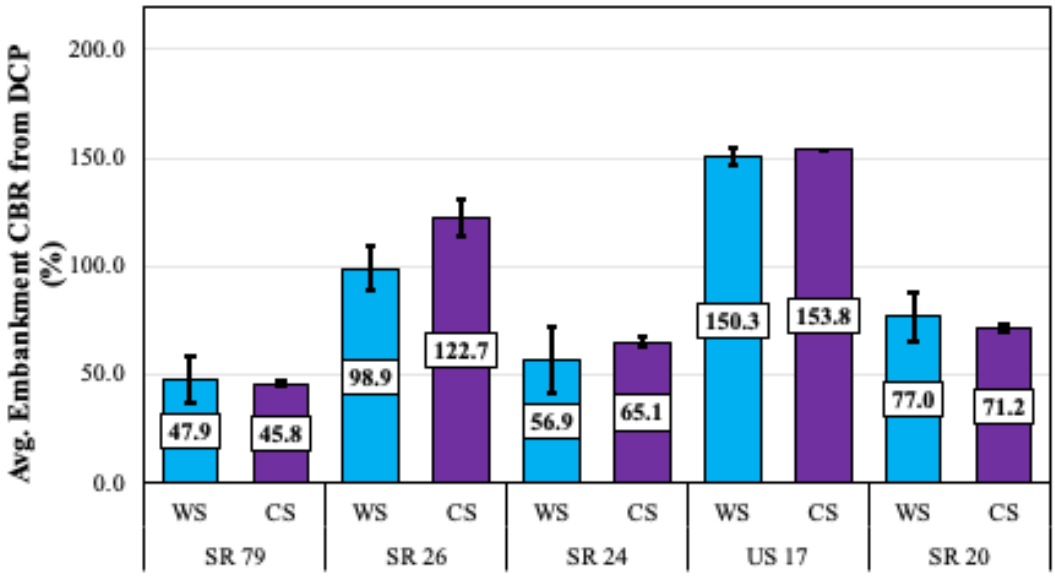

Figure 4-45. Average Embankment CBR from DCP

4.1.5. Portable Seismic Pavement Analyzer (PSPA)

Figure 4-46 shows a summary of the AC modulus obtained from PSPA testing. The PSPA data for SR 26 was not recoverable due to a corrupted database file. It should be noted that the AC modulus from PSPA is obtained at a significantly higher frequency than the FWD, and a direct comparison between the FWD and PSPA modulus may not always be reasonable. The PSPA modulus generally indicates that the AC modulus between the control and the worm sections did not exhibit a significant difference, with the exception of SR 79. The worm section of SR 79 showed a significant (i.e., approximately 58%) reduction in the AC modulus compared to the control section.

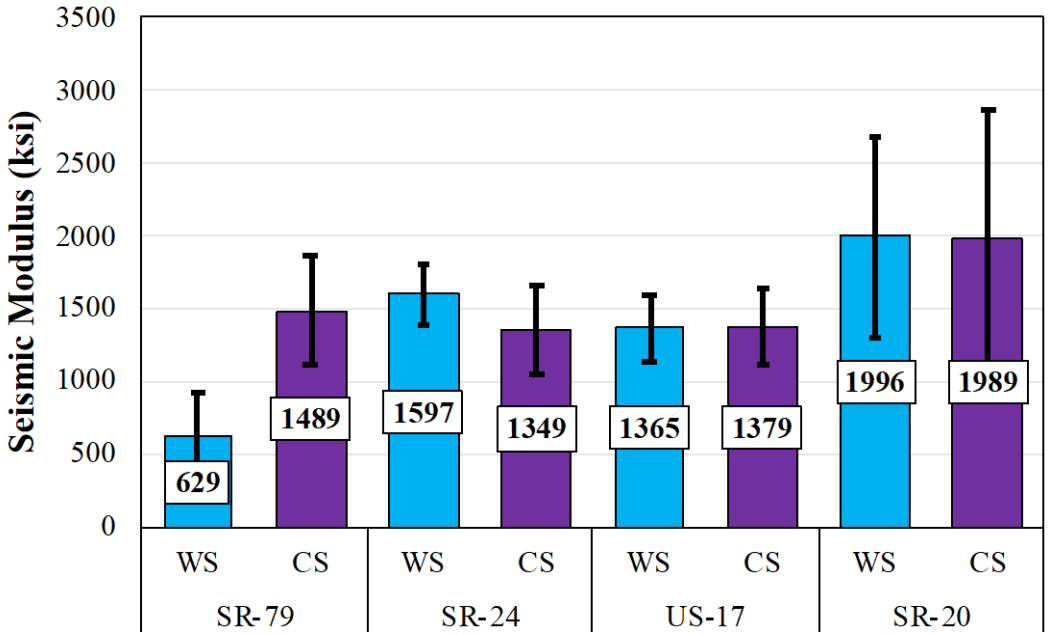

Figure 4-46. AC PSPA Moduli

4.2. AC Field Core Laboratory Test Results

4.2.1. Observation of Field Cores

Physical observations of the AC field cores are provided in the following sections. In general, interface delamination/deterioration and air voids were common. The concentration of air voids was generally greater along the interface of the top DGA layer and underlying layer. With the exception of SR 20, the composite thickness of AC in each worm section was greater than control sections.

4.2.1.1. Site 1 – FL SR 79

All cores collected from SR 79 were intact. Typical field cores are presented in Figure 4-47 through Figure 4-50. Delamination between the bottom two structural asphalt layers was observed more frequently in worm section cores. Some segregation of aggregate was evident on the bottom AC lift. AC layer thicknesses were consistent between the worm and control sections. The overall AC layer thickness and individual lift thicknesses are presented in Figure 4-51.

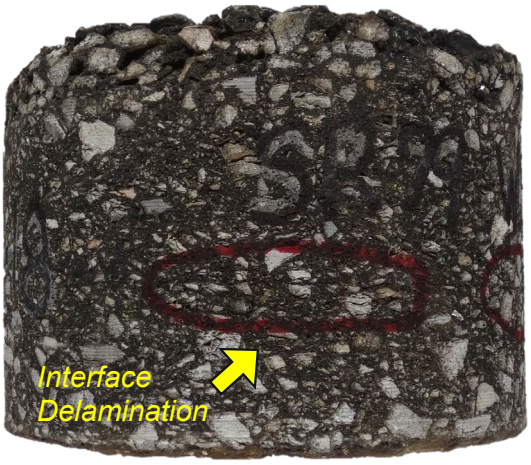

Figure 4-47. SR 79 MP 0.427 Worm Section Core – Structural AC Layer Delamination

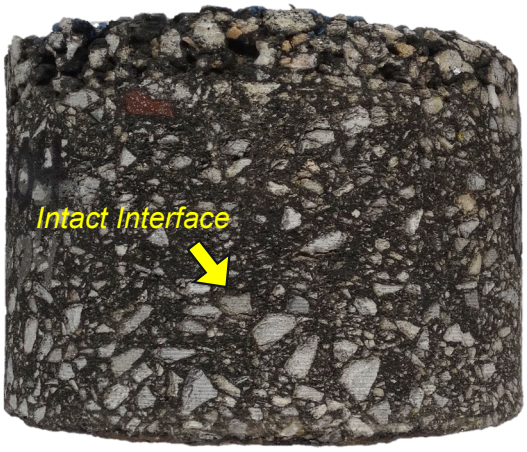

Figure 4-48. SR 79 MP 0.391 Control Section Core – Typical Core

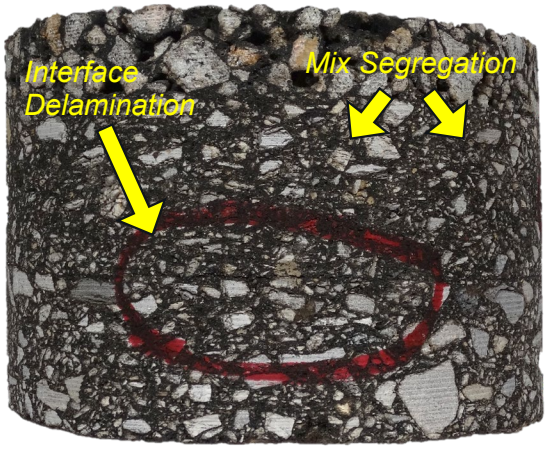

Figure 4-49. SR 79 MP 0.321 Worm Section Core – Structural AC Layer Delamination and Segregation

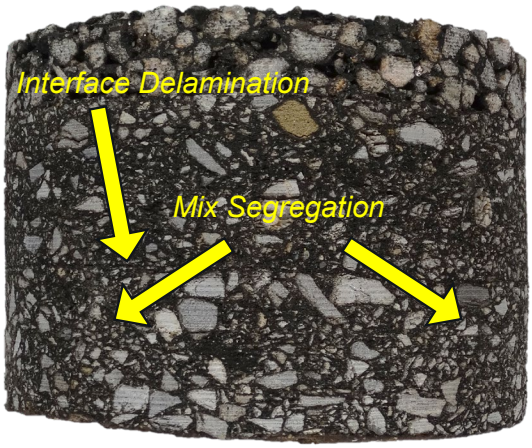

Figure 4-50. SR 79 MP 0.357 Control Section – Structural AC Layer Delamination and Segregation

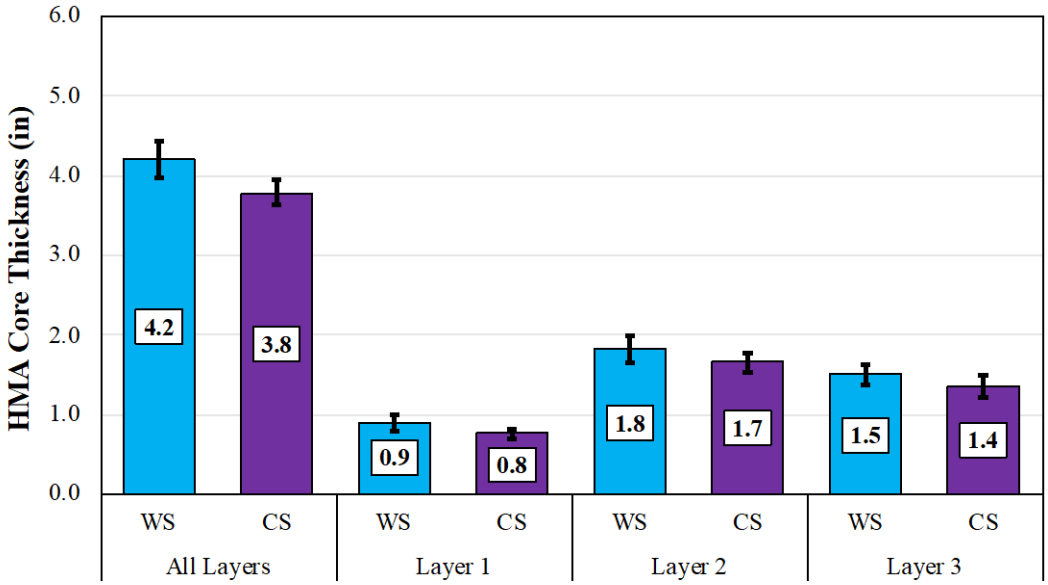

Figure 4-51. SR 79 AC Field Core Thickness

4.2.1.2. Site 2 – FL SR 26

All cores collected from SR 26 were intact. Typical field cores are presented in Figure 4-52 through Figure 4-55. Voids in the pavement structure were noted in both the top two DGA layers for control and worm section cores. The greatest concentration of voids was at the interface of these two layers in the worm section, especially at the bottom of the surface course. The stripped aggregate at this subject interface, shown in Figure 4-52, could be indicative of water traveling along the interface. SR 26 AC layer thicknesses are presented in Figure 4-56. Surface mix lift thicknesses were within 0.1-in agreement on average. The bottom lift AC was 0.6-in thicker in the worm section.

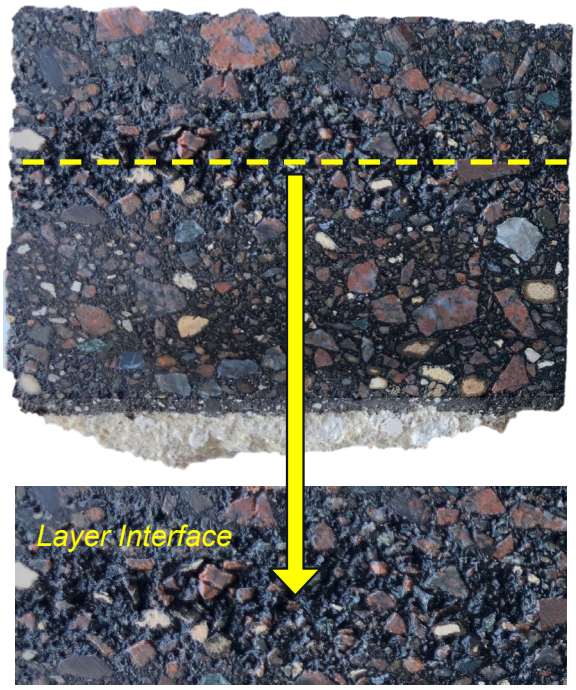

Figure 4-52. SR 26 MP 8.837 Worm Core Cross-Section – Stripping/Voids at Layer Interface

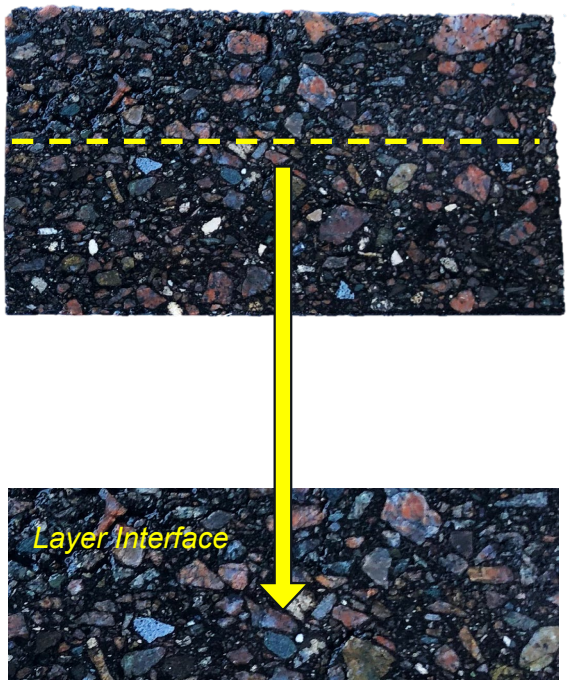

Figure 4-53. SR 26 MP 8.809 Control Core Cross-Section – Typical Core

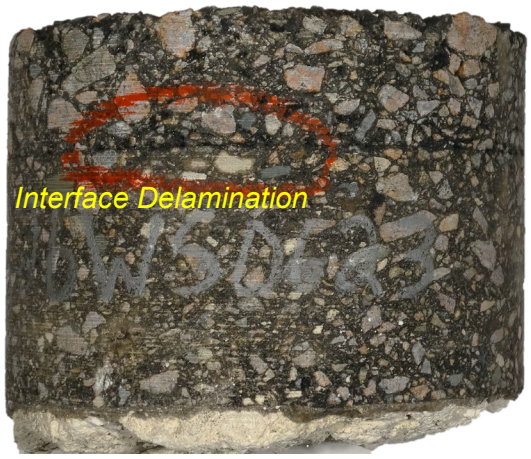

Figure 4-54. SR 26 MP 8.879 Worm Section Core – Upper Layer Delamination

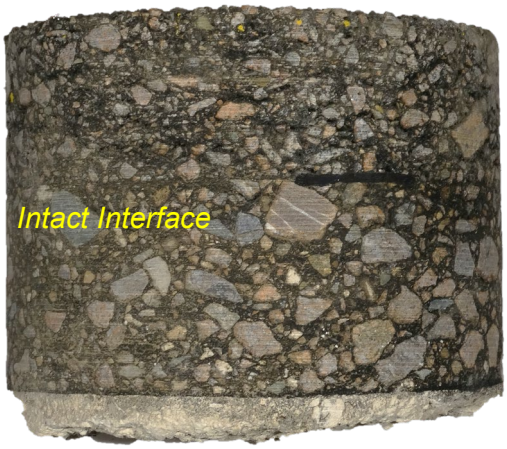

Figure 4-55. SR 26 MP 8.813 Control Core – Typical Core

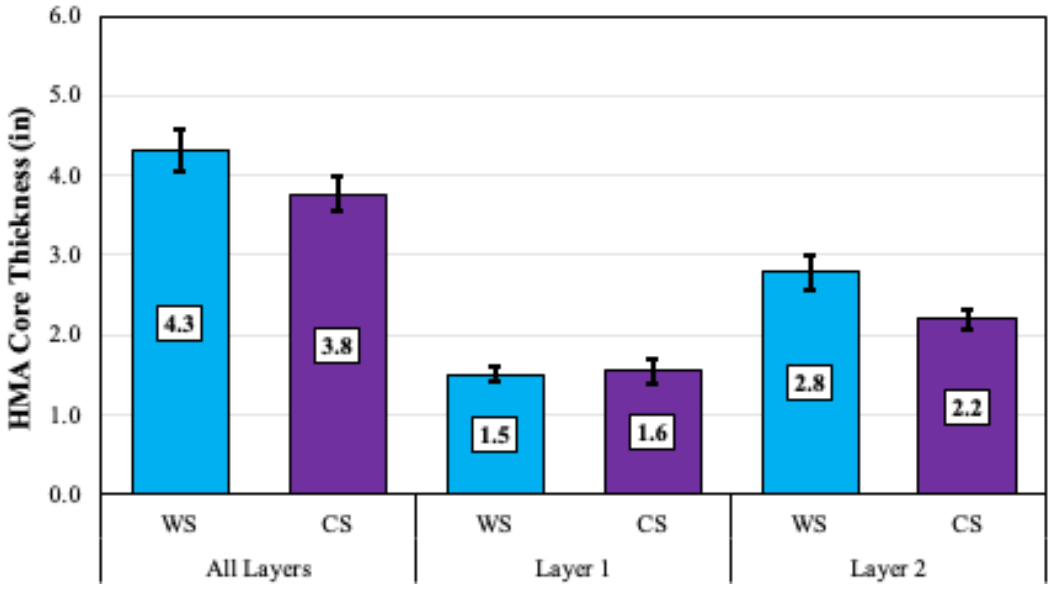

Figure 4-56. SR 26 AC Field Core Thickness

4.2.1.3. Site 3 – FL SR 24

All cores collected from SR 24 were intact. Typical field cores are presented in Figure 4-57 through Figure 4-60. Like the SR 26 cores, the SR 24 cores exhibit considerable voids at the interface of the surface course and underlying layer. These voids are primarily at the bottom of the top layer, but it appears water may have entered the pavement structure and weathered material on both sides of the interface over time. SR 26 AC layer thicknesses are presented in Figure 4-61. Layer thicknesses between worm and control groups are in good agreement.

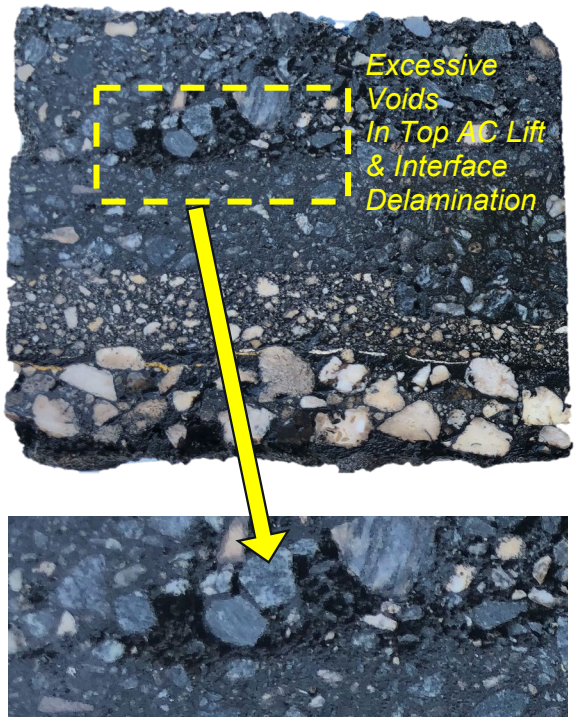

Figure 4-57. SR 24 MP 31.207 Worm Core Cross Section – Paving Lane Joint with Voids at Bottom of Friction Course

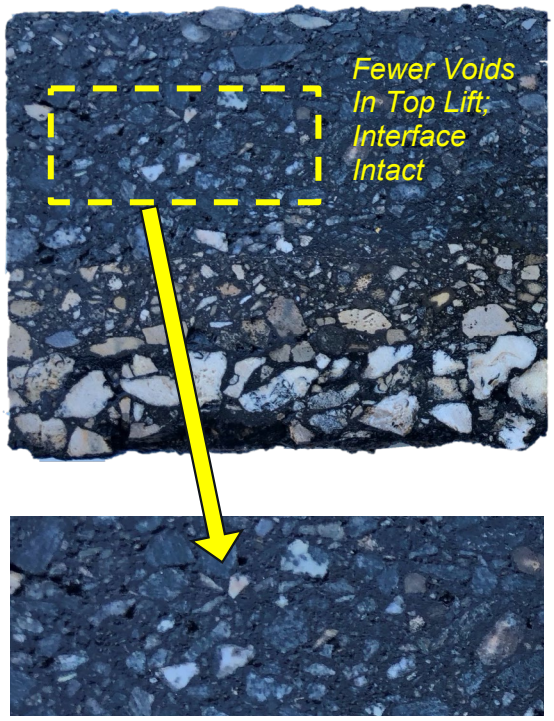

Figure 4-58. SR 24 MP 22.473 – Typical Control Core Cross-Section

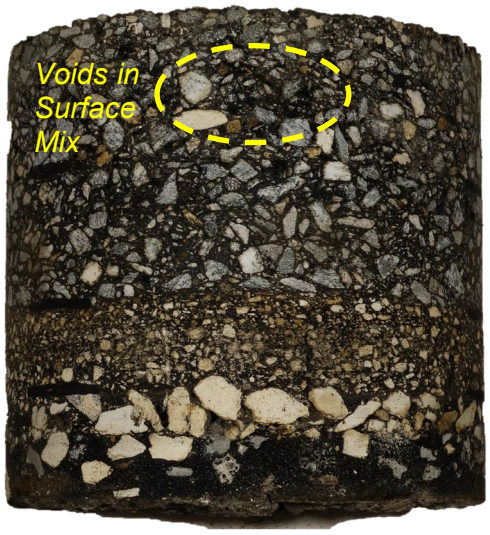

Figure 4-59. SR 24 Typical Worm Section Core at MP 31.185

Figure 4-60. SR 24 Typical Control Section Core at MP 22.489

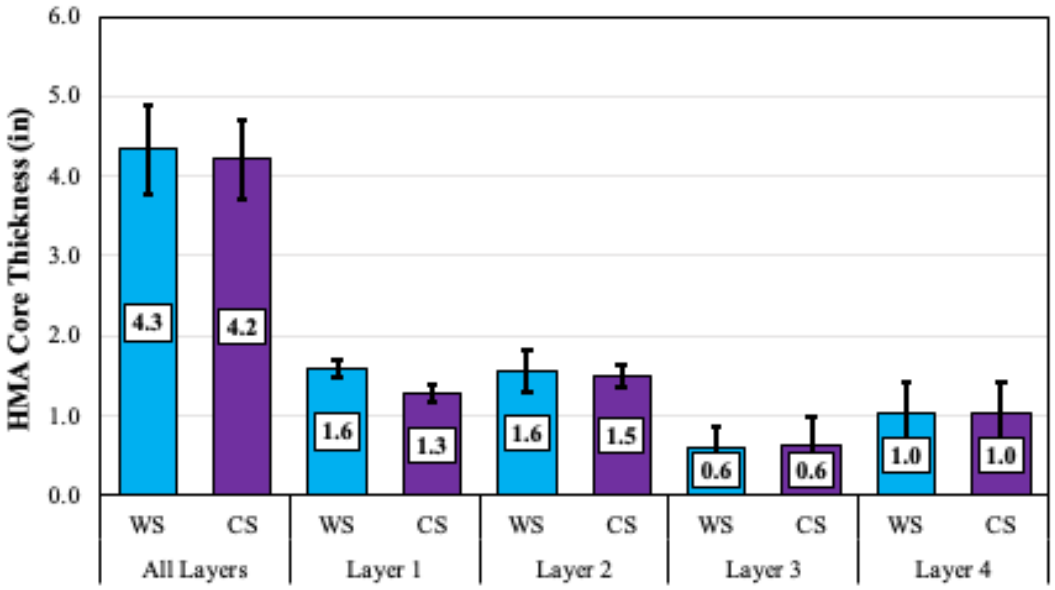

Figure 4-61. SR 24 AC Field Core Thickness

4.2.1.4. Site 4 – FL US 17

All cores collected from US 17 were intact. Typical field cores are presented in Figure 4-62 through Figure 4-65. Voids, segregation, and cracking were observed in the top DGA layer of worm section cores. Discoloration and pitting were also observed in both control and worm section layers. These defects are mostly concentrated in the top DGA layer. Figure 4-62 presents the cross section of a worm distress that was cored and sectioned, showing a crescent shaped fracture pattern consistent with the profile of a worm distress. The AC layer interfaces appear to be undamaged/not delaminated. US 17 AC layer thicknesses are presented in Figure 4-66. The composite asphalt structure is 1-in thicker than the control asphalt, on average.

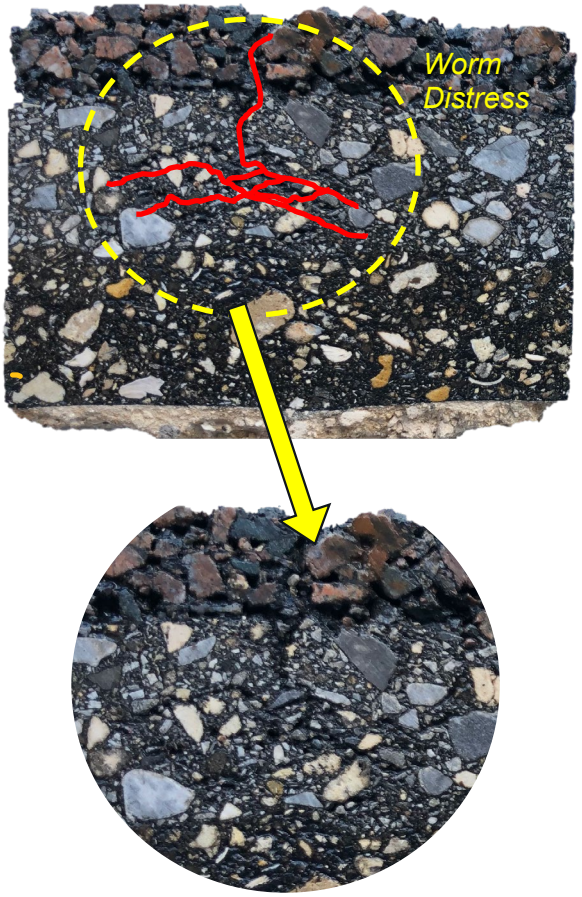

Figure 4-62. US 17 MP 17.762 Worm Distress Cross-Section Showing Crack Pattern in Upper Structural AC Layer

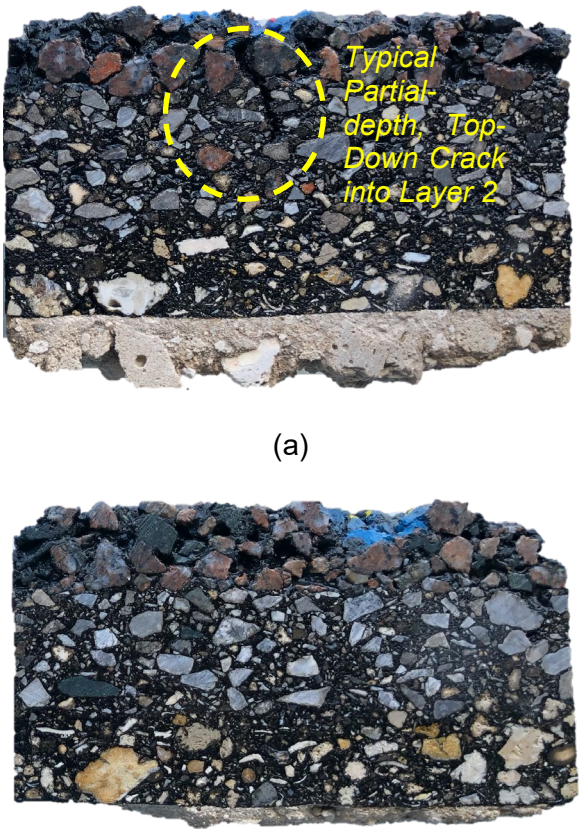

Figure 4-63. US 17 Typical Control AC Cross-Sections at (a) 17 MP 17.740 with Partial Depth Crack and (b) MP 17.406

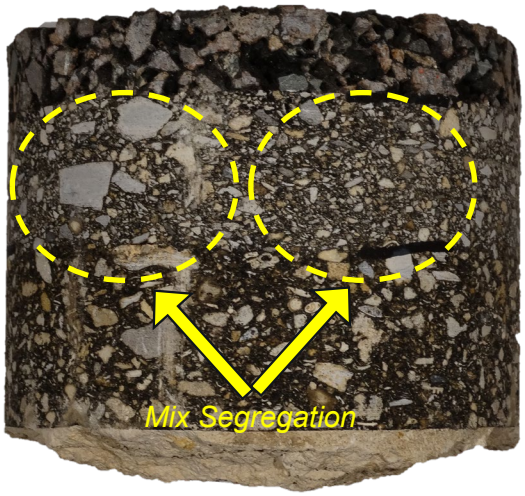

Figure 4-64. US 17 Worm Core at MP 17.795 – Layer 2 Segregation

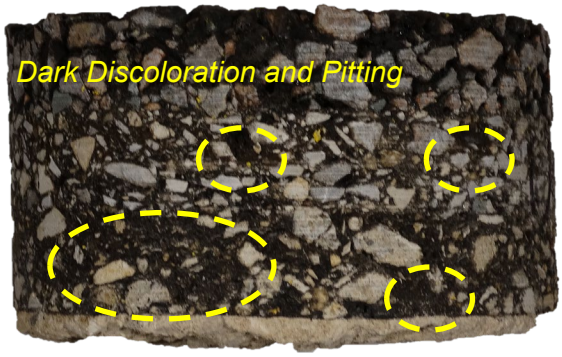

Figure 4-65. US 17 Control Core at MP 17.432 – High Air Voids in All Layers

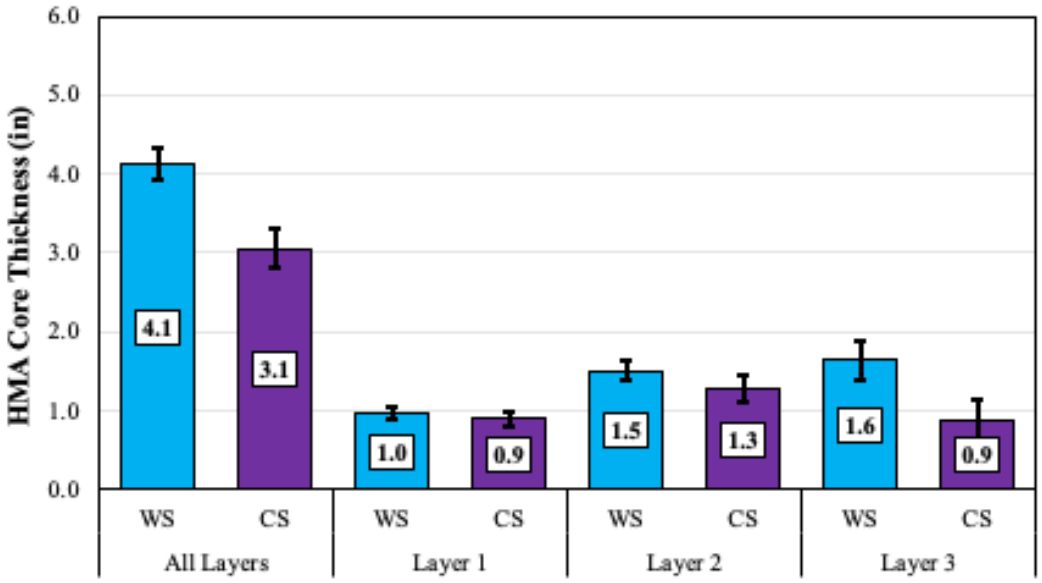

Figure 4-66. US 17 AC Field Core Thickness

4.2.1.5. Site 5 – FL SR 20

One worm section core broke at the interface during drilling/extraction in the field. The remainder of the 59 cores were collected intact. Typical field cores are presented Figure 4-67 through Figure 4-70. Voids were concentrated around the layer interface in both worm and control sections; however, these voids were more severe in the worm cores. The overall AC layer thickness and individual lift thicknesses are similar for the worm and control cores and are presented in Figure 4-71.

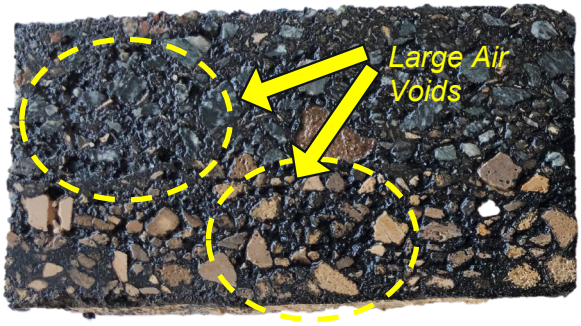

Figure 4-67. SR 20 MP 2.511 Worm Section Paving Lane Joint Cross-Section Showing Large Air Voids in Both AC Layers

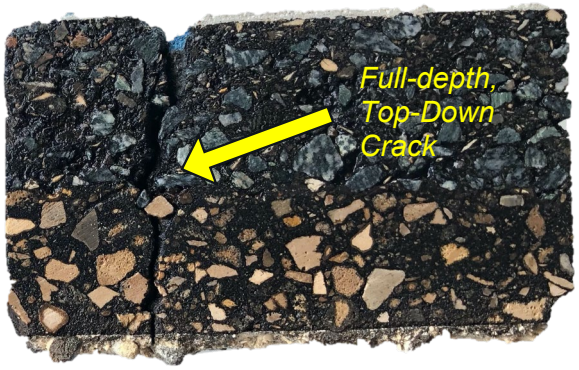

Figure 4-68. SR 20 MP 2.973 Control Section Paving Lane Joint Cross-Section Showing Top-Down Crack

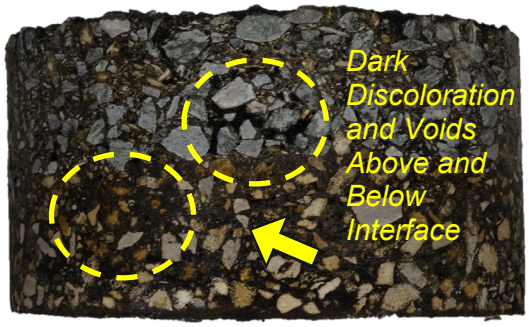

Figure 4-69. SR 20 Worm Section Paving Lane Core with Large Air Voids at MP 2.442

Figure 4-70. SR 24 Typical Control Section Core at MP 2.931

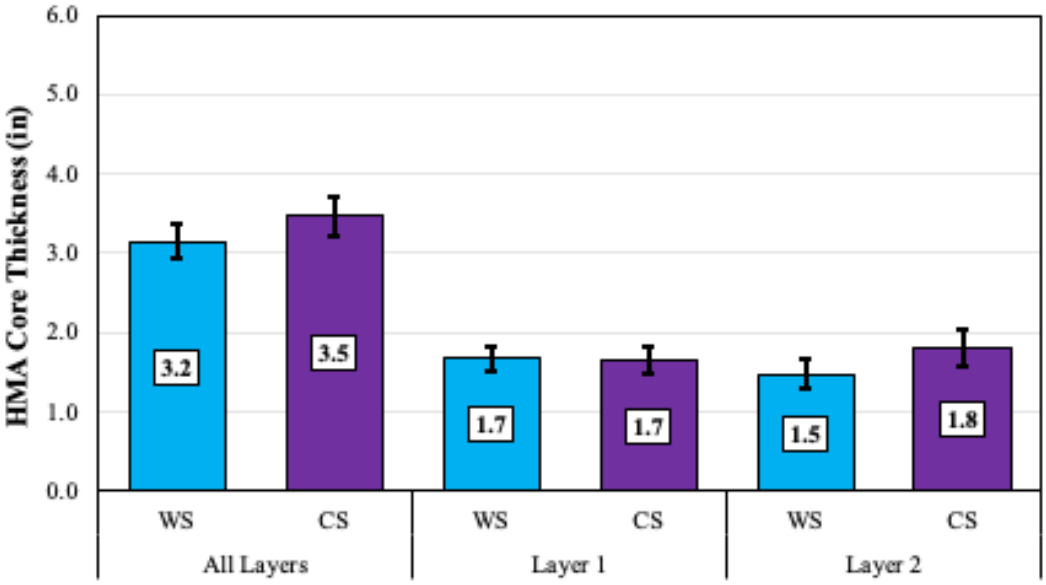

Figure 4-71. SR 20 AC Field Core Thickness

4.2.2. Gradation and Binder Content

A comparison of binder contents determined by solvent extraction for AC sampled from worm and control sections is presented in Figure 4-72. Seven of 11 comparisons showed the worm section mixtures contained lower AC than the control section. Binder contents ranged from 4.53% to 6.83% across all projects. Differences in binder content ranged from 0.1% to 1.1% for dense-graded AC. Mixture gradations were plotted on an FHWA 0.45 power gradation chart with control points from AASHTO M323-07. Control points, as well as the primary control sieve (PCS) control point from AASHTO M323-07, were used to characterize mixtures. Aggregate gradations for the dense-graded mixtures are presented in Figure 4-73 through Figure 4-82. Three of the roadways featured one 9.5-mm nominal maximum aggregate size (NMAS) layer. The remainder of the mixtures were 12.5-mm NMAS. With the exception of the bottom AC lift in the worm section of SR 20, all AC mixes were fine graded. All of the 12.5-mm NMAS AC sampled featured either worm or control section material passing the 3/8-in (9.5-mm) sieve outside of the AASHTO tolerance. The general shape of the partial size distributions with respect to the maximum density lines was similar between worm and control sections. No recurring bias was observed between worm and control aggregate particle size distributions.

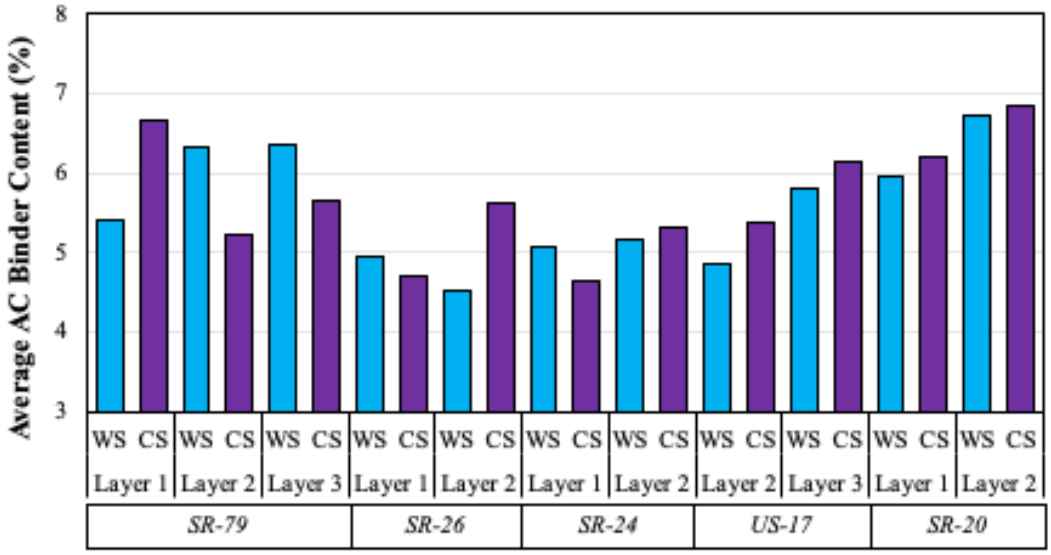

Figure 4-72. AC Binder Content

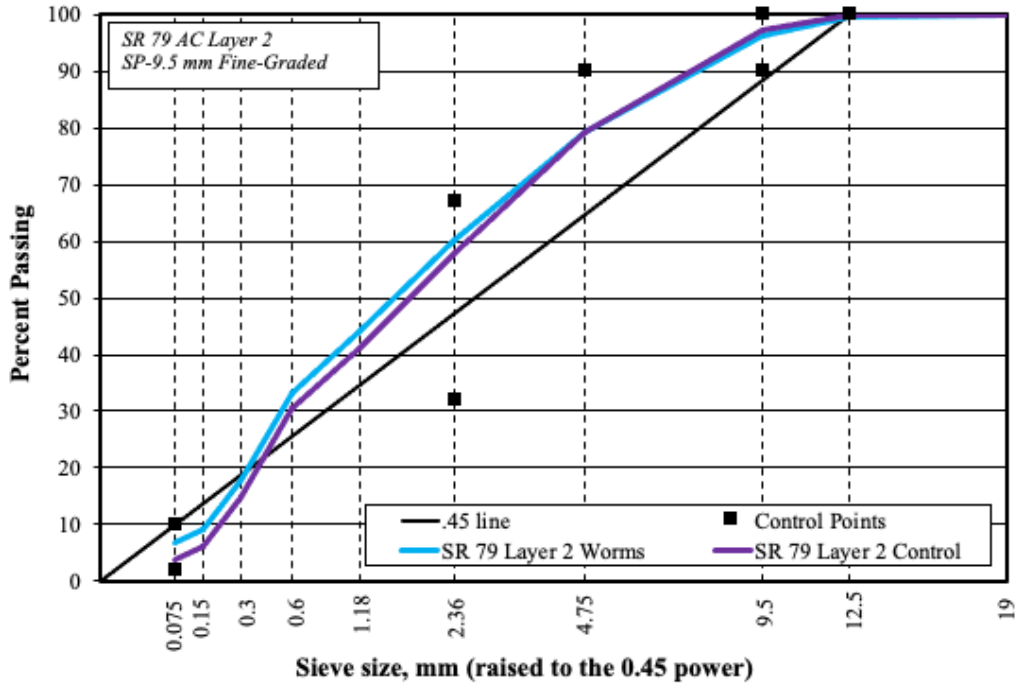

Figure 4-73. SR 79 Layer 2 SP-9.5 Fine-Graded AC Gradations

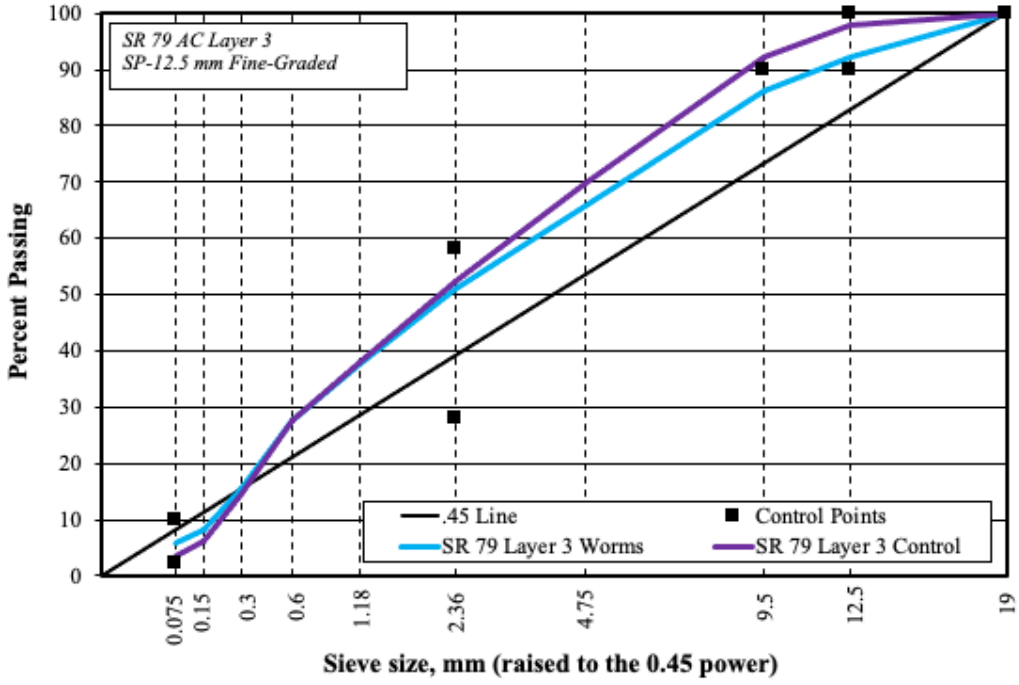

Figure 4-74. SR 79 Layer 3 SP-12.5 Fine-Graded AC Gradations

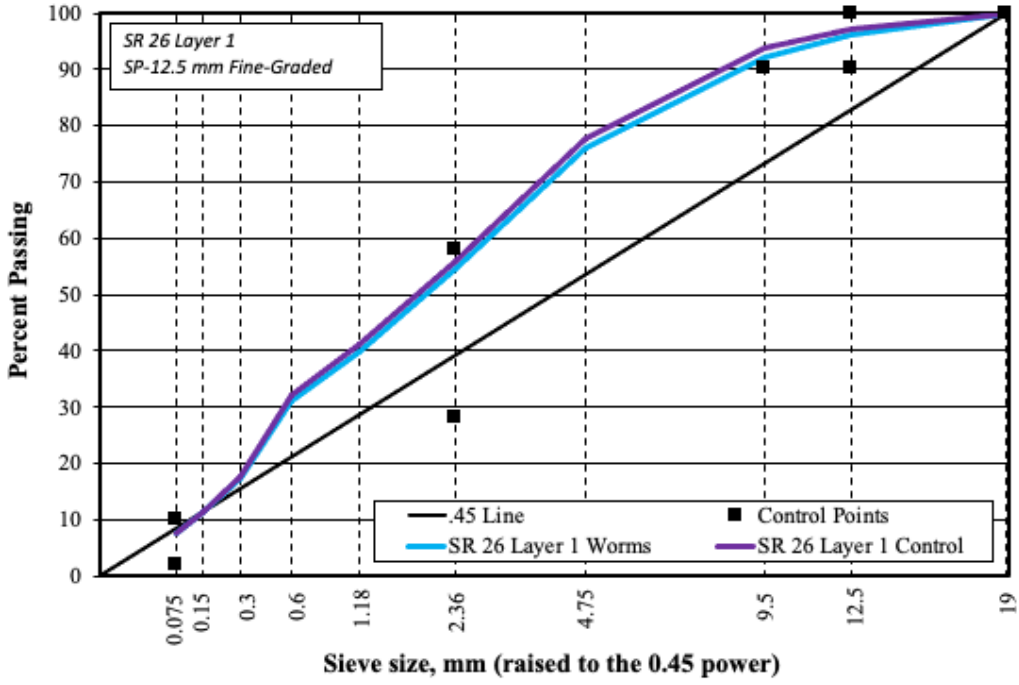

Figure 4-75. SR 26 Layer 1 SP-12.5 Fine-Graded AC Gradations

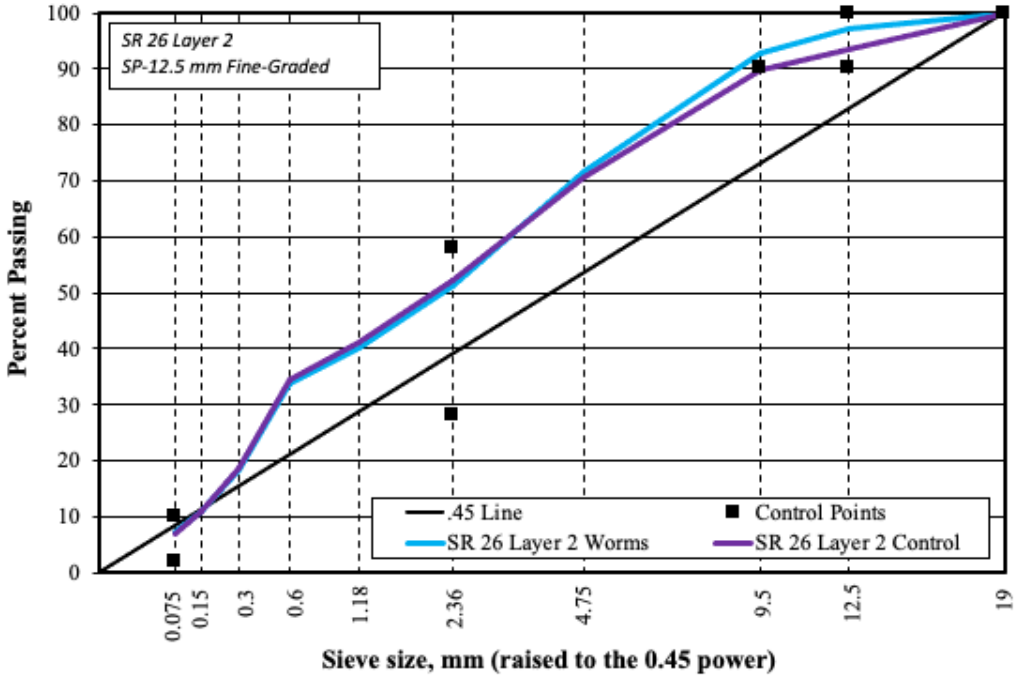

Figure 4-76. SR 26 Layer 2 SP-12.5 Fine-Graded AC Gradations

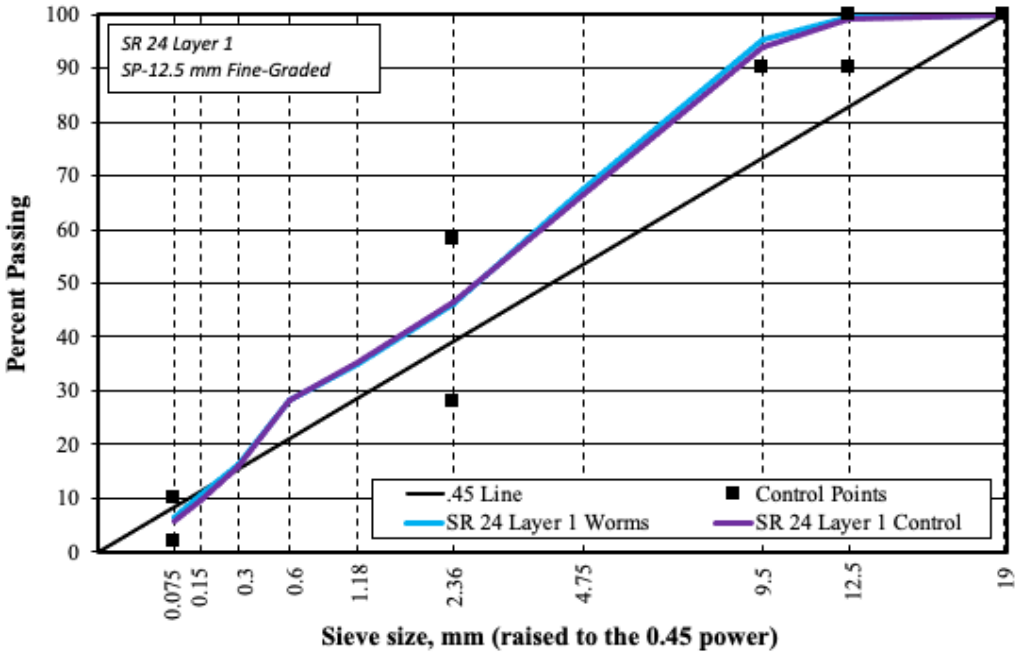

Figure 4-77. SR 24 Layer 1 SP-12.5 mm Fine-Graded AC Gradations

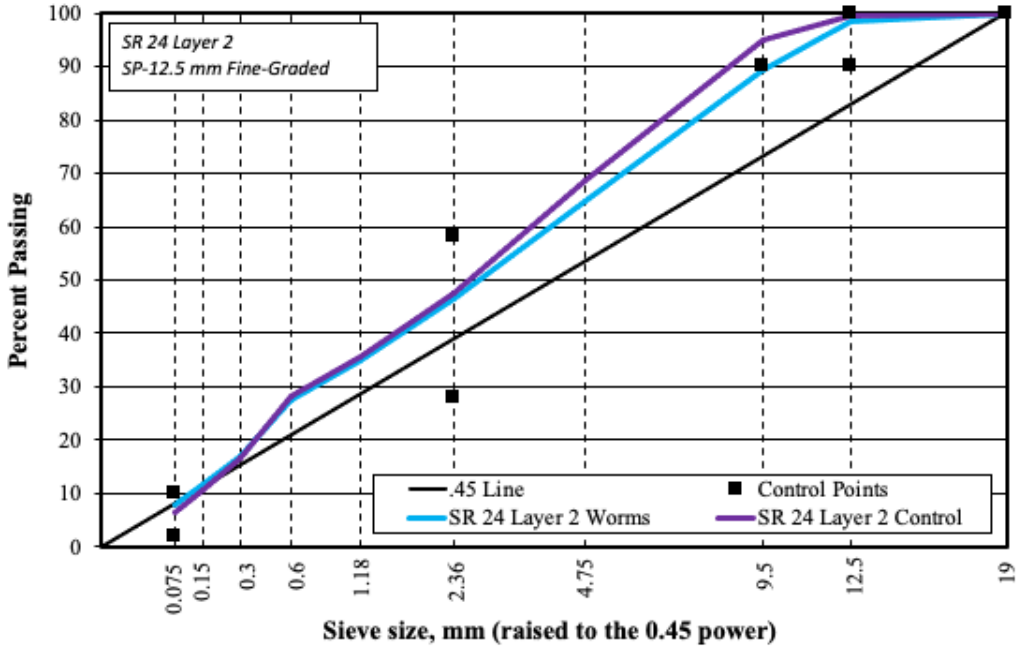

Figure 4-78. SR 24 Layer 2 SP-12.5 mm Fine-Graded AC Gradations

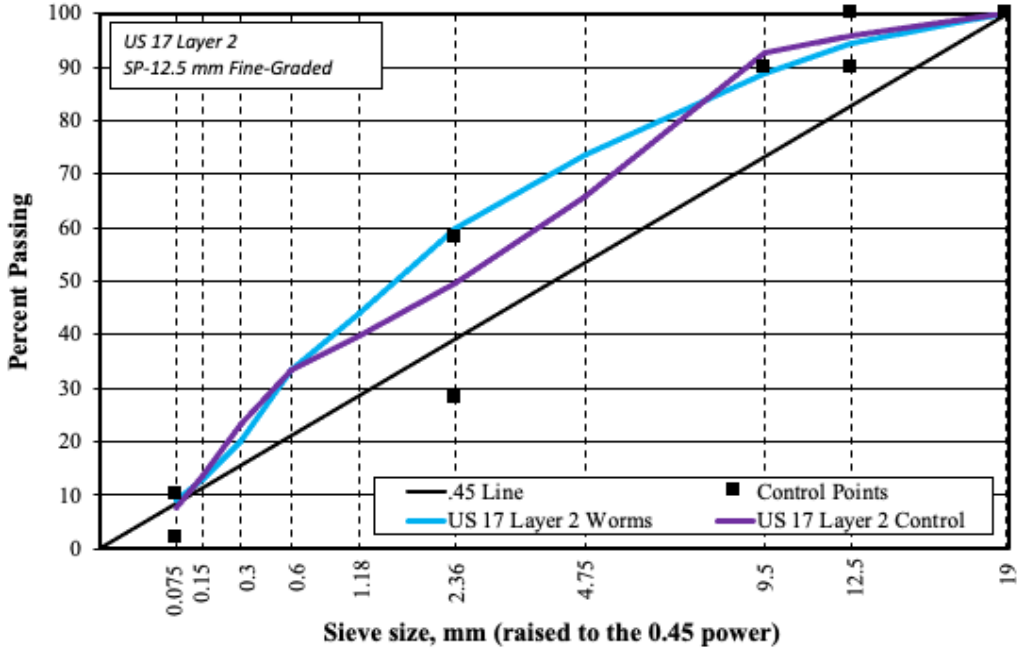

Figure 4-79. US 17 Layer 2 SP-12.5 mm Fine-Graded AC Gradations

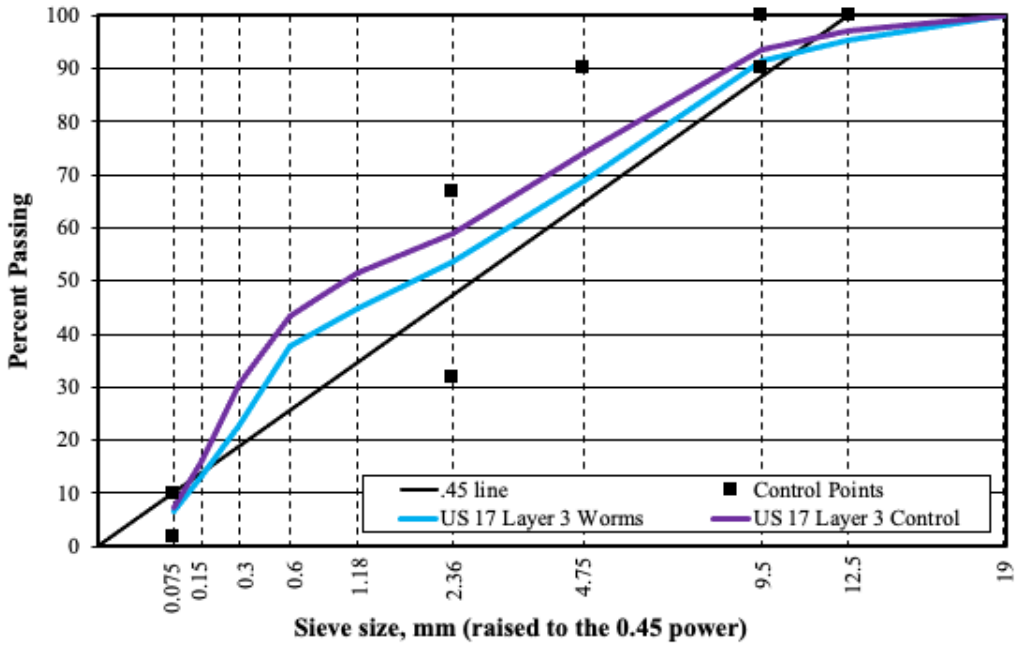

Figure 4-80. US 17 Layer 3 SP-9.5 mm Fine-Graded AC Gradations

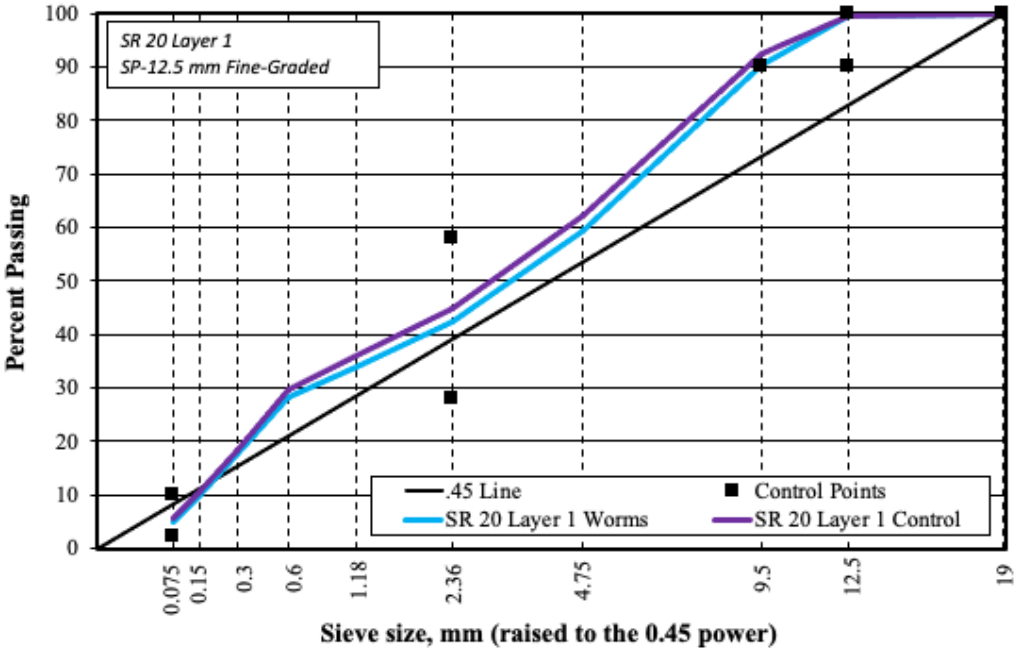

Figure 4-81. SR 20 Layer 1 SP-12.5 mm Fine-Graded AC Gradations

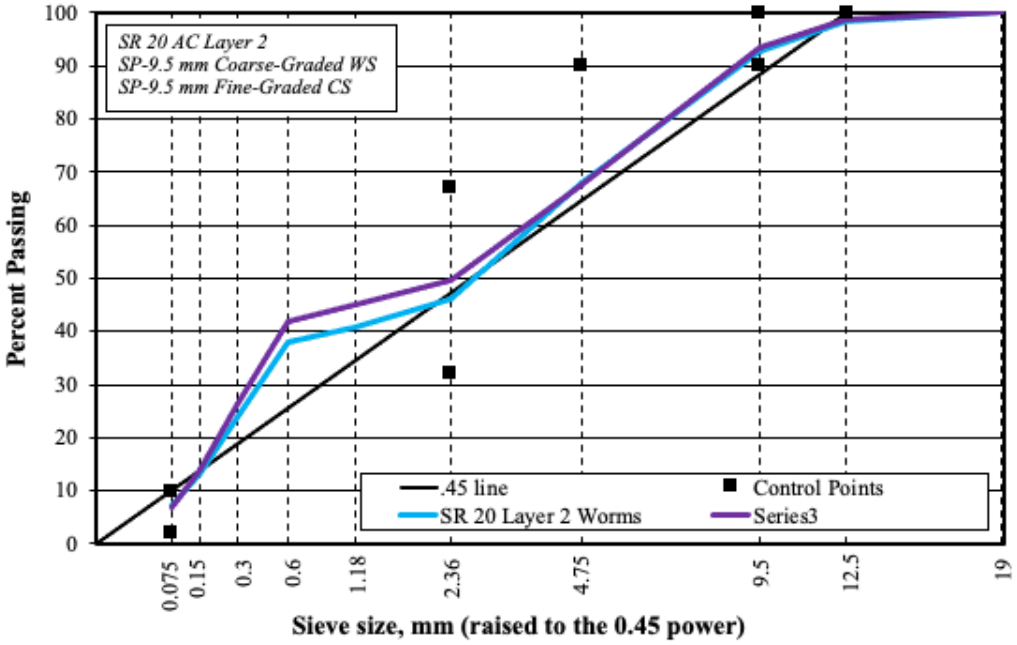

Figure 4-82. SR 20 Layer 2 SP-9.5 Coarse- and Fine-Graded AC Gradations

4.2.3. Core Density

Figure 4-83 through Figure 4-87 present the average air void content for field cores. It was determined after testing the first site (SR 79) that OGFC was likely not a contributing factor to the development of worm distresses; therefore, the US 17 OGFC was not tested. The air void content of DGA materials ranged from 3.63% to 14.13%. In the upper two DGA layers of each project, 90% of the AC tested on the five projects exhibited air voids in excess of the 4% target. The worm section AC contained greater air voids than the control section in 7 of the 10 subject layers.

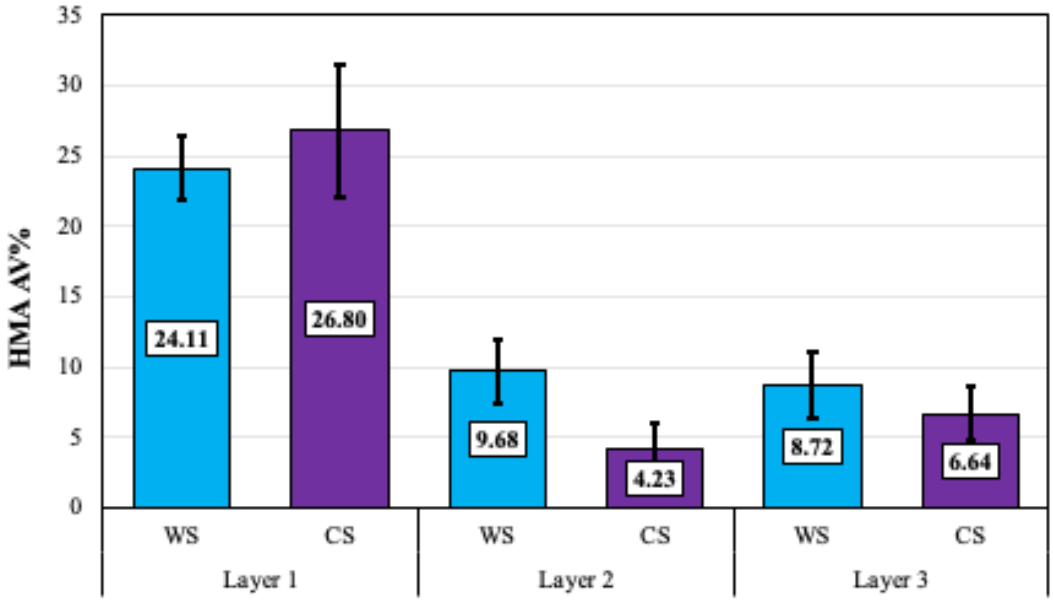

Figure 4-83. SR 79 AC Field Core Air Voids

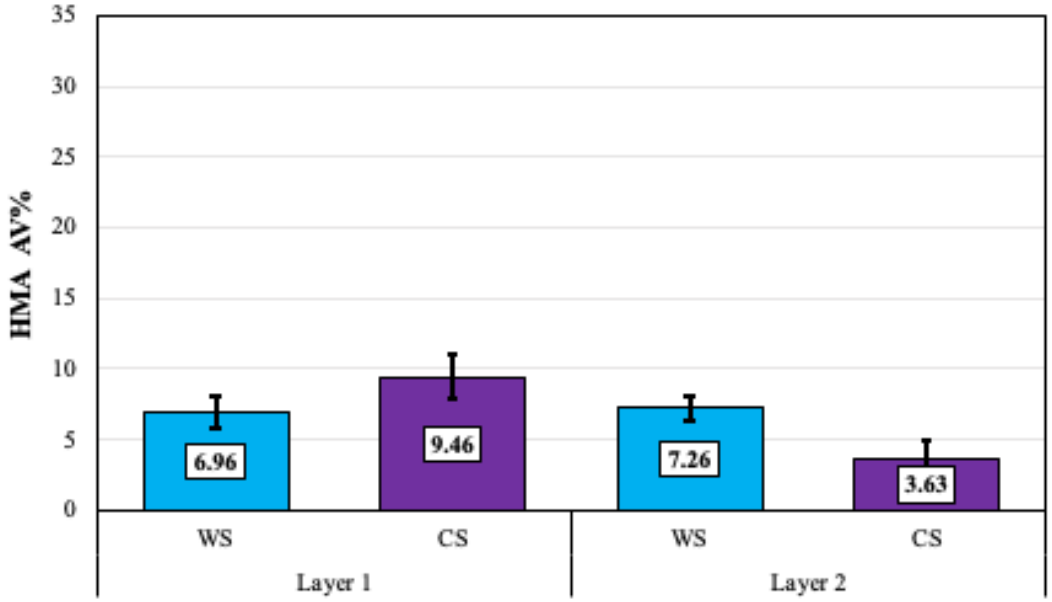

Figure 4-84. SR 26 AC Field Core Air Voids

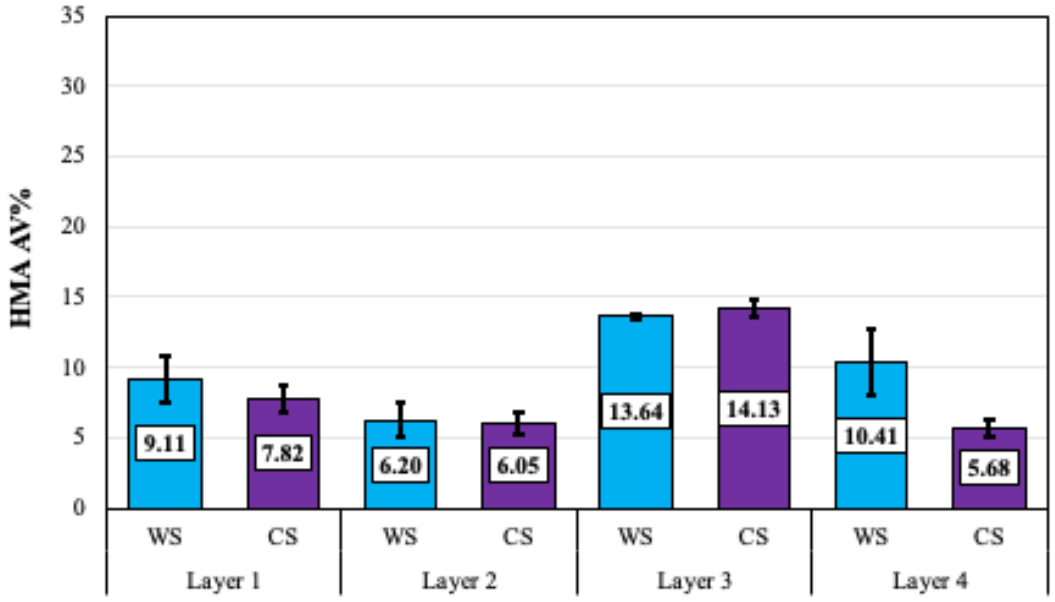

Figure 4-85. SR 24 AC Field Core Air Voids

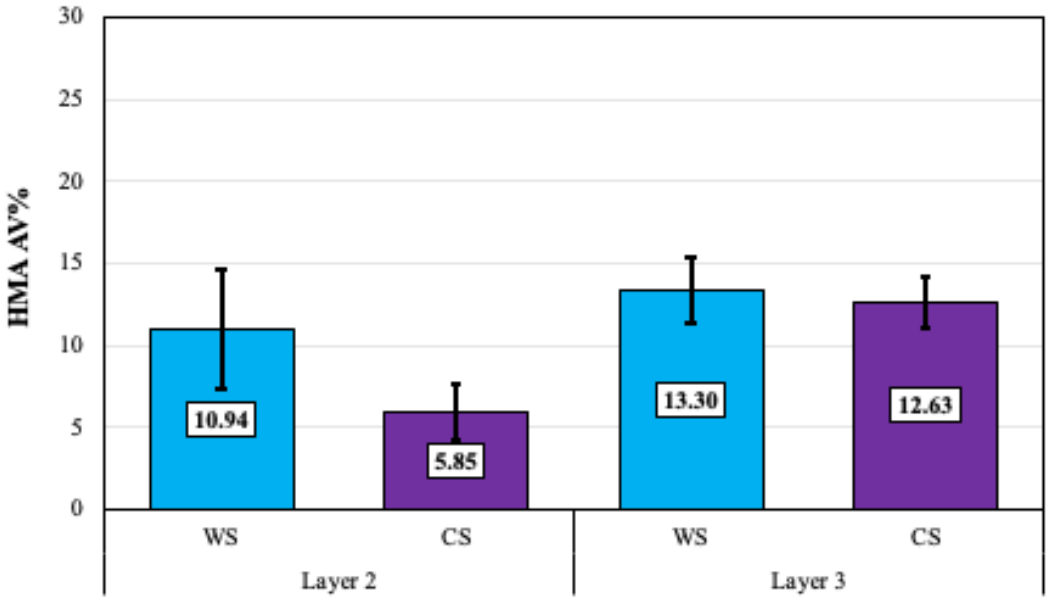

Figure 4-86. US 17 AC Field Core Air Voids

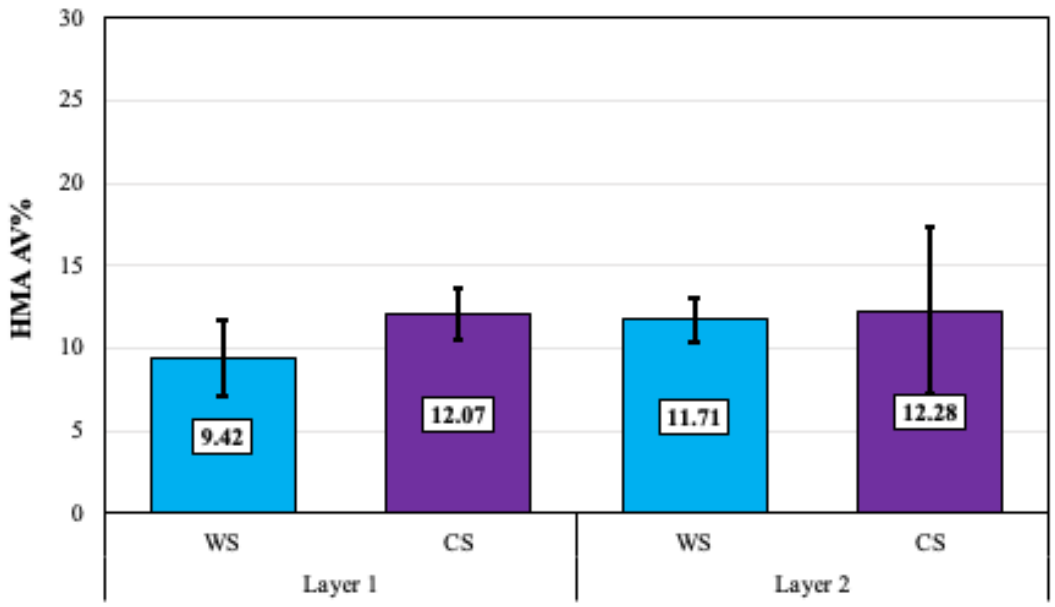

Figure 4-87. SR 20 AC Field Core Air Voids

4.2.4. Permeability

Results from AC permeability tests are provided in Table 4-15 through Figure 4-19. The corresponding percent air void content for each core tested is also provided in each table for reference. The permeability results indicate the subject AC mixtures are generally impermeable, even with high air void contents. These results were surprising, considering the excessive air voids in these mixtures. After further study of the core samples, the research team presumes air void content is greater along the friction/binder course interface, as indicated in Section 4.2.1. The other extreme boundaries of these layers appear to be sound, with tighter texture and presumably less permeability. Therefore, a possible interpretation of this finding is that the localized air voids in the fine-graded mixtures are generally not interconnected. Overall, the permeability findings are not generalizable to suggest highly permeable layers in the AC structure are a prerequisite for worm distress.

Table 4-15. SR 79 AC Permeability

		k, (E-5 cm/s)			Air Voids, (%)		
Section Type	Field Core Milepost	Layer 1	Layer 2	Layer 3	Layer 1	Layer 2	Layer 3
Worm	0.423	3000	4	0	21.5	8.0	6.3
	0.403	731	1	1	19.6	9.3	6.9
	0.396	1695	4	0	25.9	11.4	6.6
Control	0.389	1040	0	1	9.8	4.0	5.8
	0.387	4135	0	3	28.4	4.3	9.2
	0.351	1910	0	3	23.9	4.4	6.0

Table 4-16. SR 26 AC Permeability

Section Type	Field Core Milepost	k, (E-5 cm/s)		Air Voids, (%)	
		Layer 1	Layer 2	Layer 1	Layer 2
Worm	8.818	0	DS[1]	6.3	DS[1]
	8.854	6	0	10.0	8.9
	8.871	1	0	6.8	7.3
	8.882	0	0	5.9	5.9
	8.896	0	0	6.3	6.9
Control	8.770	59	0	11.5	6.3
	8.777	14	0	5.9	3.3
	8.789	2	0	10.1	4.8
	8.795	1	0	9.3	1.8
	8.815	8	0	8.5	4.6

[1]Damaged Sample (DS)

Table 4-17. SR 24 AC Permeability

Section Type	Field Core Milepost	k, (E-5 cm/s)				Air Voids, (%)			
		Layer 1	Layer 2	Layer 3	Layer 4	Layer 1	Layer 2	Layer 3	Layer 4
Worm	31.146	0	0	NP[1]	DS[2]	7.4	4.9	NP[1]	12.1
	31.182	0	29	NP[1]	19	7.5	7.0	NP[1]	7.9
	31.196	49	2	NP[1]	2	11.8	7.4	NP[1]	7.7
	31.210	11	16	8	24	10.0	7.2	13.4	13.9
	31.218	4	0	40	14	8.9	4.6	13.7	10.5
Control	22.414	13	0	NP[1]	5	7.6	4.6	NP[1]	6.7
	22.448	73	0	171	1	9.4	5.9	14.7	5.6
	22.458	13	0	17	1	8.1	6.7	13.3	4.6
	22.463	6	0	NP[1]	0	7.6	6.9	NP[1]	5.9
	22.518	0	0	NP[1]	0	6.5	6.2	NP[1]	5.6

[1]Layer Not Present (NP), presumably due to past mill and overlay
[2]Damaged Sample (DS)

Table 4-18. US 17 AC Permeability

Section Type	Field Core Milepost	k, (E-5 cm/s)		Air Voids, (%)	
		Layer 2	Layer 3	Layer 2	Layer 3
Worm	17.716	11	0	15.3	15.2
	17.727	0	0	4.3	10.2
	17.777	4	2	11.4	14.7
	17.788	2	7	11.3	14.5
	17.820	3	0	12.4	11.6
Control	17.349	269	7	16.3	9.2
	17.363	2	20	11.7	16.4
	17.410	1	22	11.8	12.8
	17.421	3	35	10.4	13.4
	17.453	0	3	7.2	10.5

Table 4-19. SR 20 AC Permeability

Section Type	Field Core Milepost	k, (E-5 cm/s)		Air Voids, (%)	
		Layer 1	Layer 2	Layer 1	Layer 2
Worm	2.421	4	0	12.2	11.7
	2.439	1	0	9.6	11.3
	2.468	0	0	7.6	10.1
	2.493	5	3	11.5	10.7
	2.525	1	812	6.3	11.6
Control	2.892	3	0	14.3	15.9
	2.908	1	0	10.2	6.9
	2.947	3	3	13.2	17.1
	2.970	19	0	10.7	5.4
	2.986	2	0	11.8	16.1

4.2.5. Interlayer Bond Strength

A total of 58 bond strength tests were performed to assess the interlayer bond strength of the top two dense-graded AC layers of each project. Bond test results are presented in Figure 4-88. The test results show the presence of worm distress is consistent with a reduction in interlayer bond strength. Overall, a total of 31 cores could not be tested due to material failure and not necessarily bond failure. During the initial testing of cores retrieved from SR 79, five consecutive cores failed in the AC material outside of the interface (within the AC mixture itself), resulting in invalid tests. The material failures occurred both in cores sampled from the control and worm-distressed sections. It was observed that the cores did not have interfaces that were truly in plane with the surface of the roadway. To account for this skew, the gap between the shear and reaction frames was increased from 0.25 to 0.375 in to promote better layer interface alignment within the gap. The 0.375-in gap spacing was maintained for all interlayer bond strength tests. Failures in the AC mix continued to occur on cores sampled from all five sites,

possibly indicating a loss of durability, stiffness, and strength of the AC at the subject interface. Of the 58 tests performed, 14 failures were observed in the top AC layer, 8 failures were observed in the bottom layer, 30 cores sheared at the interface, and 5 cores exhibited fractures in both the upper and lower AC layers. No core samples from US 17 fractured along the interface. Both AC layers at the interface were considerably deteriorated; however, the lower layer exhibited the most severe pitting and voids. A close-up of these distresses along the interface are shown on a typical worm section core in Figure 4-89.

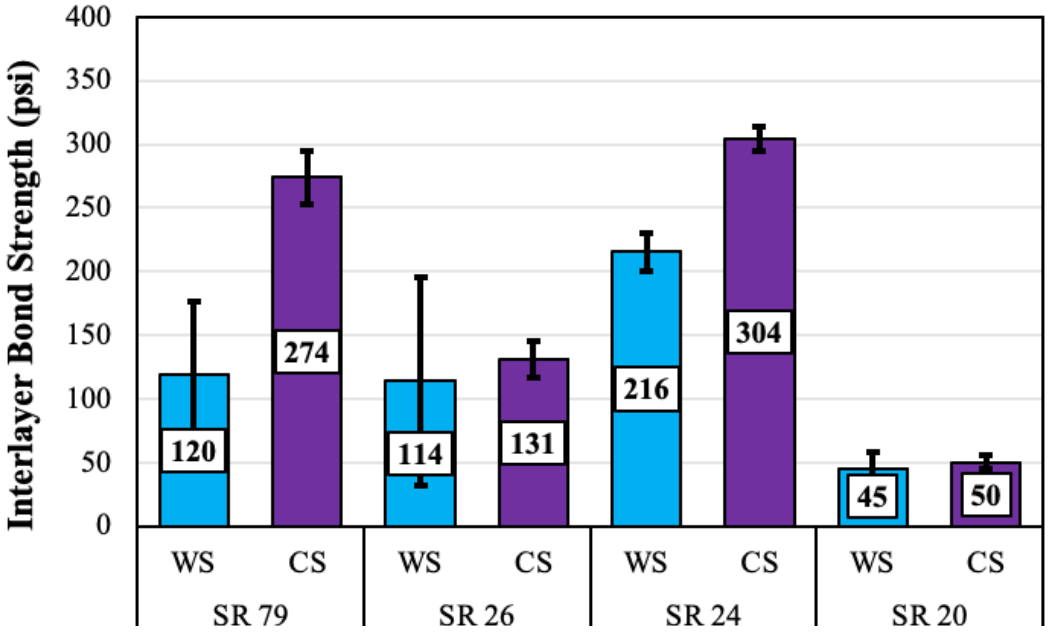

Figure 4-88. Interlayer Bond Strength Results

Figure 4-89. Close-up of Air Voids at US 17 Worm Core Layer Interface

Layer interfaces were photographed after the conclusion of bond testing. Photographs of the resulting interfaces are shown in Figure 4-90 through Figure 4-98. General observations of the appearance (not a determinative assessment of tack coat uniformity) of the cores include:

- SR 79
  - Control Section: Uniform tack coat on interfaces.
  - Worm Section: Inconsistent tack coat coverage; approximately 30% to 40% of tack material missing or has brown color that resembles an unbroken or re-emulsified tack coat.
- SR 26
  - Control Section: Tack coat is not uniform; dirt present on interface presumably from construction traffic.
  - Worm Section: Similar in appearance to control section. Impregnated dirt in surface of texture of the AC may be a factor in lower bond strength but does not explain worm distress.
- SR 24
  - Control Section: Uniform tack coat on interfaces.
  - Worm Section: Missing tack coat; appearance may indicate trapped water between layers has stripped tack in areas and left behind white stains.
- US 17
  - Control Section: Light brown discoloration over approximately 10% of core interfaces and some evidence of dirt contamination; however, bond between layers appears to generally be stronger than cohesion of the asphalt mixture.
  - Worm Section: Similar to control section; however, more dirt contamination and small traces of whitish reside that may be staining from water.
- SR 20
  - Control Section: No evidence of tack coat; voids in the surface texture may be a product of the movement of water in the interface.
  - Worm Section: No evidence of tack material; significant pitting and voids could be a product of the movement of water in the interface.

Control Section MP 0.391

Worm Section MP 0.398

Control Section MP 0.359

Worm Section MP 0.313

Figure 4-90. SR 79 Example AC Layer Interfaces

Control Section MP 0.392

Worm Section MP 8.818

Control Section MP 0.366

Worm Section MP 8.8180

Figure 4-91. SR 26 Example AC Layer Interfaces

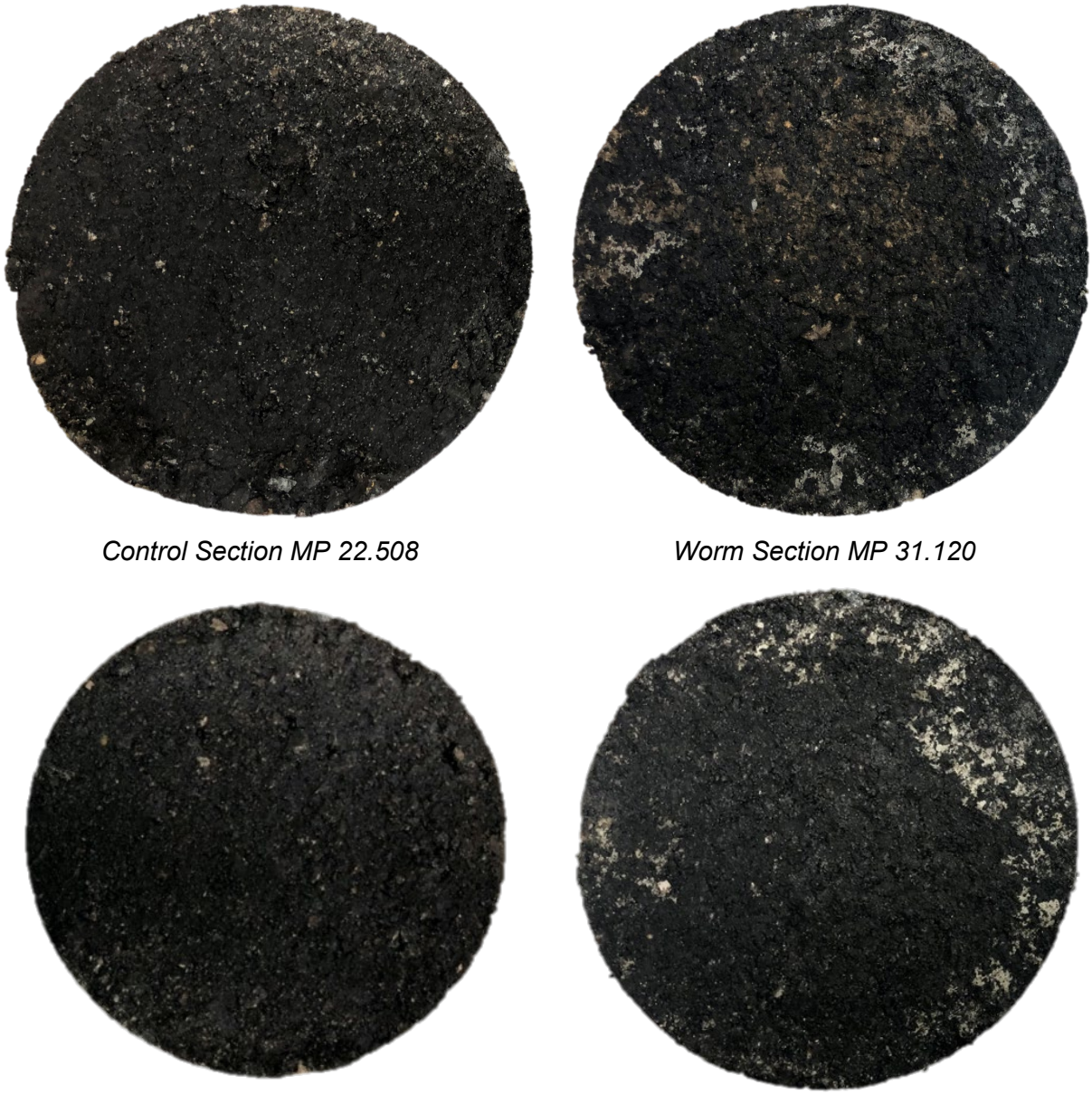

Control Section MP 22.508 | *Worm Section MP 31.120*

Control Section MP 22.547 | *Worm Section MP 31.192*

Figure 4-92. SR 24 Example AC Layer Interfaces

Figure 4-93. US 17 Control Section MP 17.403 Bond Test Failure Outside of Interface

Figure 4-94. US 17 Control Section MP 17.401 Bond Test Failure Outside of Interface

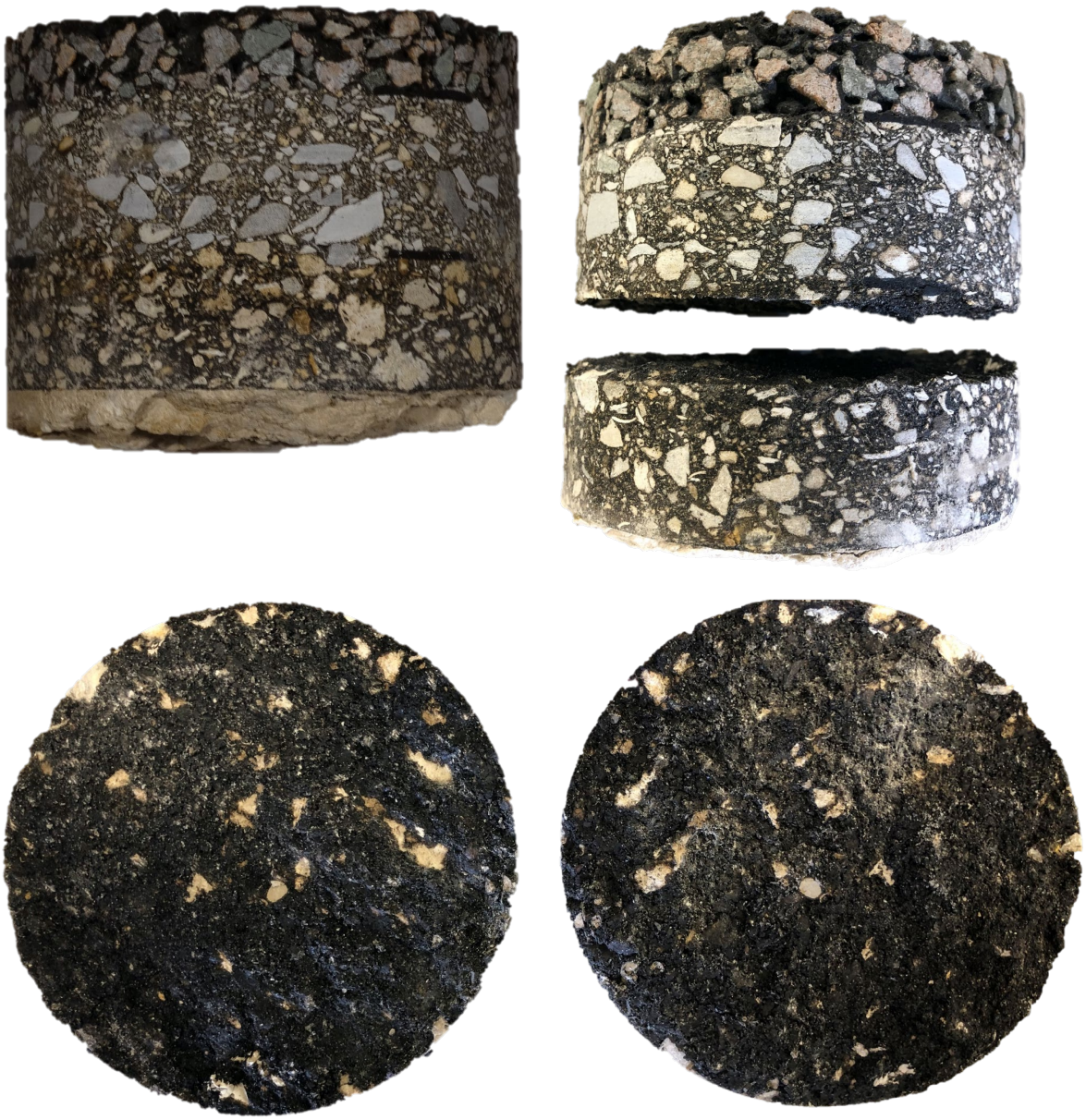

Figure 4-95. US 17 Worm Section MP 31.130 Bond Test Failure Outside of Interface

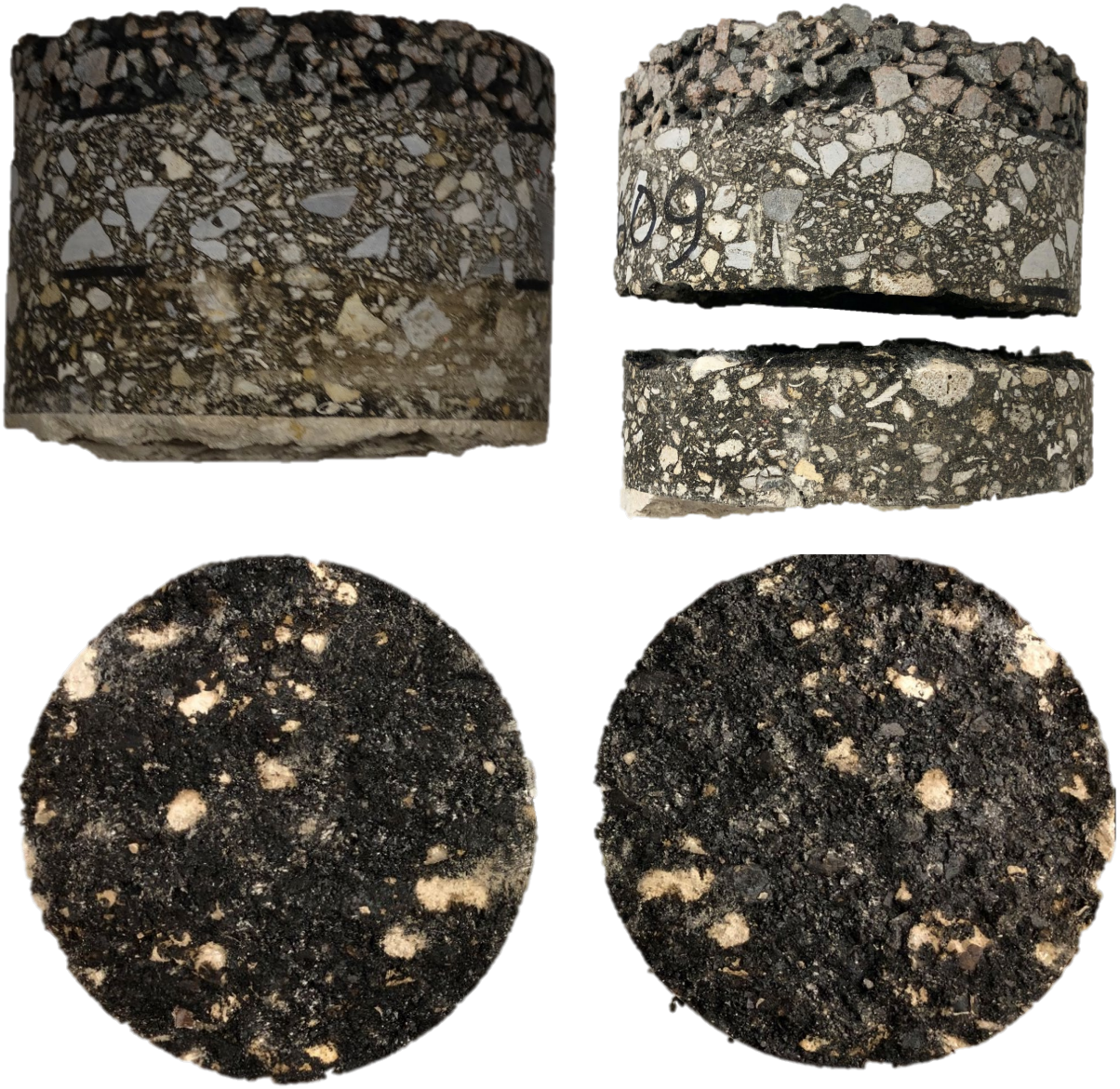

Figure 4-96. US 17 Worm Section MP 31.146 Bond Test Failure Outside of Interface

Control Section MP 2.940

Worm Section MP 2.471

Control Section MP 2.953

Worm Section MP 2.489

Figure 4-97. SR 20 Example AC Layer Interfaces

Figure 4-98. Additional Examples of Failures outside of Interface on Roadway

4.2.6. Indirect Tensile Resilient Modulus Test

As discussed in Section 4.1.3.1, the FWD data was not used for backcalculating the dynamic modulus of AC layers for SR 79, due to the malfunction of the FWD temperature sensor. As such, it was necessary to test the field cores in the laboratory to obtain the dynamic modulus needed for pavement response simulation and performance prediction.

AASHTO T 342 specifies that the dynamic modulus testing of AC mixtures be tested on cylindrical specimens having a diameter of 4.0 in and a height of 6.0 in. However, the field cores obtained from SR 79 were mostly less than 4.0-in thick and, hence, the cylindrical specimens required by AASHTO T 342 could not be obtained. As such, it was decided to conduct the resilient modulus test in the indirect tensile test (IDT) mode and backcalculate the dynamic modulus from the resilient modulus test data using the procedures developed by Lee and Kim [30].

The field cores obtained from both the control and the worm sections of SR 79 were carefully cut to separate the top (SP 9.5 mix) and the bottom (SP 12.5 mix) layers of AC. A minimum of three replicate specimens were obtained for each section (i.e., control vs. worm) and for each layer (i.e., top and bottom). The IDT resilient modulus was conducted at the following three

temperatures: 32 °F (0ºC), 50ºF (10ºC), and 68ºF (20ºC). For each temperature, the replicate specimens were placed in the target temperature for at least 4 hours prior to the IDT tests. After the specimens had been equilibrated with the specified testing temperature, the resilient modulus test was conducted for five cycles in which each cycle consisted of a 0.1-sec haversine loading followed by a 0.9-sec rest period. The maximum horizontal strain in the resilient modulus test under the IDT testing mode was kept below 100 με. A picture of the IDT testing setup is shown in Figure 4-99.

Figure 4-99. Indirect Tensile Test Setup

The backcalculation approach developed by Lee and Kim [30] first involves backcalculation of the creep compliance using a least squares approach and then converting the creep compliance to dynamic modulus. In order to backcalculate the creep compliance using the least squares approach, it is necessary to identify a function that represents the creep compliance of viscoelastic materials. Because of the nature of least squares, it is also important that the function have a simple form with the least number of coefficients to minimize the computation time and effort. The power function, which has been well accepted as an analytical representation of the creep compliance of viscoelastic materials, was used for this purpose. The power function is expressed as follows:

$$D(t) = D_0 + D_1 \cdot t^m \quad \textbf{(2)}$$

As an example, Figure 4-100 and Figure 4-101 show the measured horizontal and vertical strains from the IDT testing, respectively, of SP 12.5 mixture at 50ºF. The figures also show the respective strains predicted from backcalculation of the creep compliance, which are in excellent agreement with the measured strains.

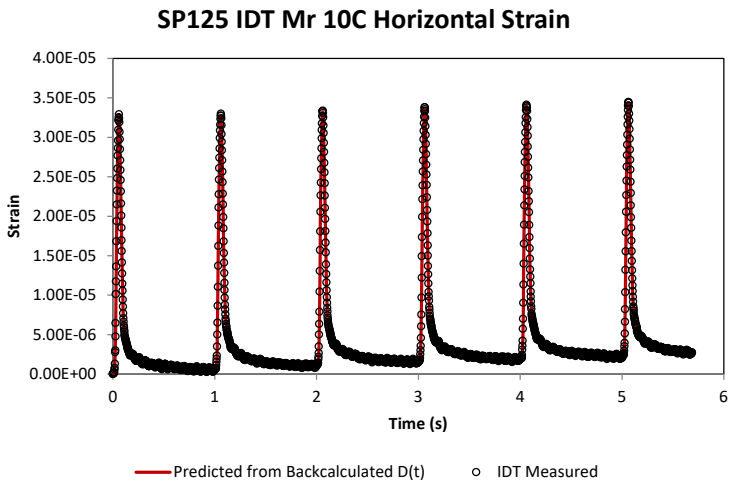

Figure 4-100. Measured and Predicted IDT Horizontal Strain for SP 12.5 at 50ºF

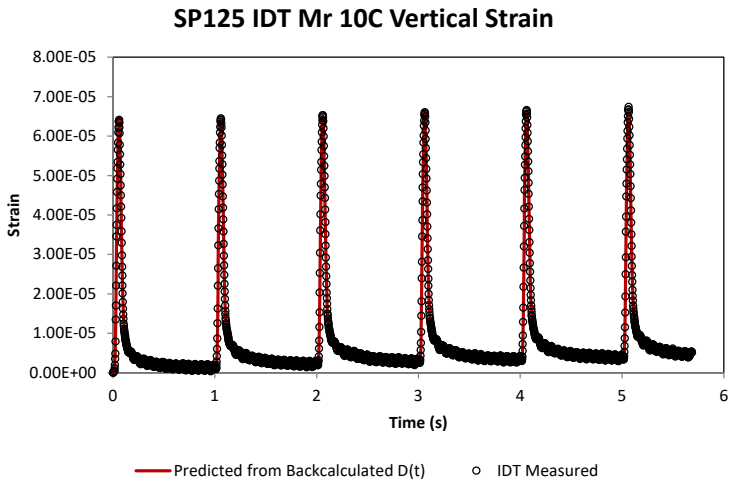

Figure 4-101. Measured and Predicted IDT Vertical Strain for SP 12.5 at 50ºF

The backcalculated creep compliance functions were then first converted to the complex compliance functions using the equation shown below.

$$D^*(\omega) = i\omega \cdot L\left[D(t)\right]_{s=i\omega} = D'(\omega) - D''(\varpi) \qquad (3)$$

where $L[f(t)] = \hat{f}(s) = \int_0^\infty e^{-st} f(t)dt$ is the Laplace transform of the function $f(t)$, *s* is the Laplace variable, ω is the angular frequency, and *D'* and *D"* are the real and imaginary parts of the complex compliance. Once the real and imaginary parts of the complex compliance are determined, the dynamic modulus is simply obtained as the reciprocal of the complex compliance magnitude, as shown in the equation below:

$$|E^*(\omega)| = \frac{1}{|D^*(\omega)|} = \frac{1}{\sqrt{D'(\omega)^2 + D''(\omega)^2}} \quad (4)$$

Using the above methodology, the power function parameters for the creep compliance were backcalculated from the resilient modulus test data and converted to the dynamic modulus values corresponding to five distinct frequencies of 0.1, 0.5, 1.0, 5.0, and 10.0 Hz. The dynamic modulus values at the respective temperatures were then shifted in accordance to the time-temperature superposition principle to obtain the dynamic modulus master curve. An example of the backcalculated dynamic modulus values at the respective temperatures are shown in Figure 4-102 for the SP 12.5 mix from the control section, while the constructed master curve is shown in Figure 4-103.

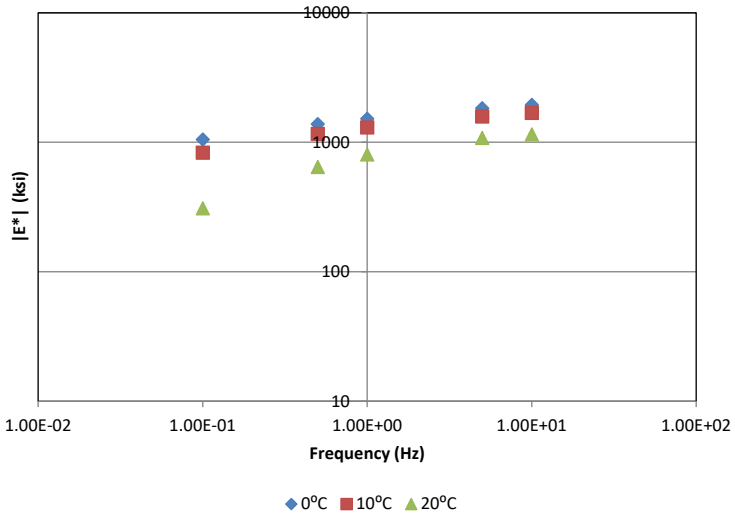

Figure 4-102. Backcalculated Dynamic Modulus Values for SP 12.5 at Three Different Temperatures

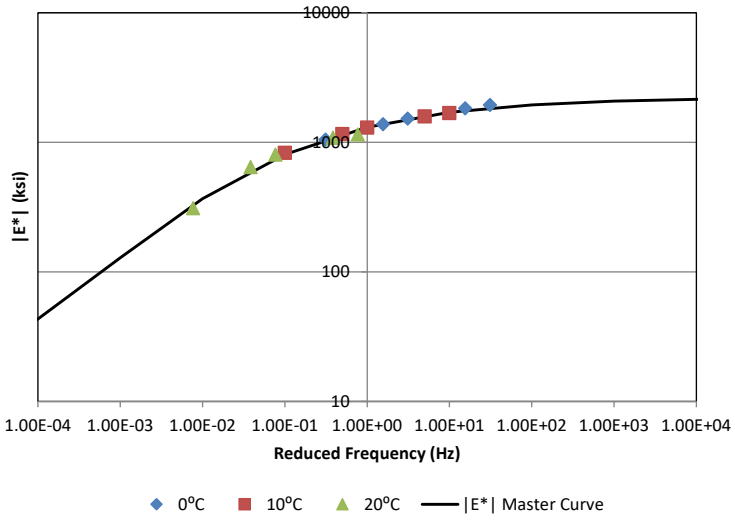

Figure 4-103. Dynamic Modulus Master Curve for SP 12.5 at a Reference Temperature of 50ºF

Figure 4-104 and Figure 4-105 show the AC dynamic modulus master curves for SR 79 at a reference temperature of 50ºF (10ºC) for the top and the bottom AC lifts, respectively. Similar to the trends of the FWD backcalculated dynamic modulus master curves, the worm section shows significantly lower modulus for the top lift AC (Figure 4-104). More specifically, the top lift AC modulus was found to be 1,323 ksi and 618 ksi for the control and worm sections, respectively. This corresponds to a 53% reduction in AC modulus for the worm section, which is in agreement with the PSPA data discussed previously (Figure 4-46). The bottom lift AC from the worm section is also showing lower modulus compared to the control section (Figure 4-105), although the difference is not as significant—approximately 26% reduction from control section modulus of 1,703 ksi to worm section modulus of 1,257 ksi.

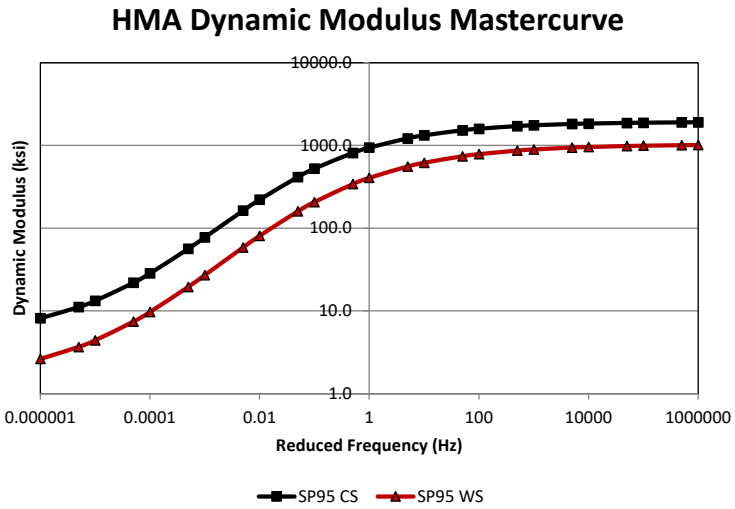

Figure 4-104. Dynamic Modulus Master Curves for the Top Lift of SR 79 AC (SP 9.5) at a Reference Temperature of 50 ºF

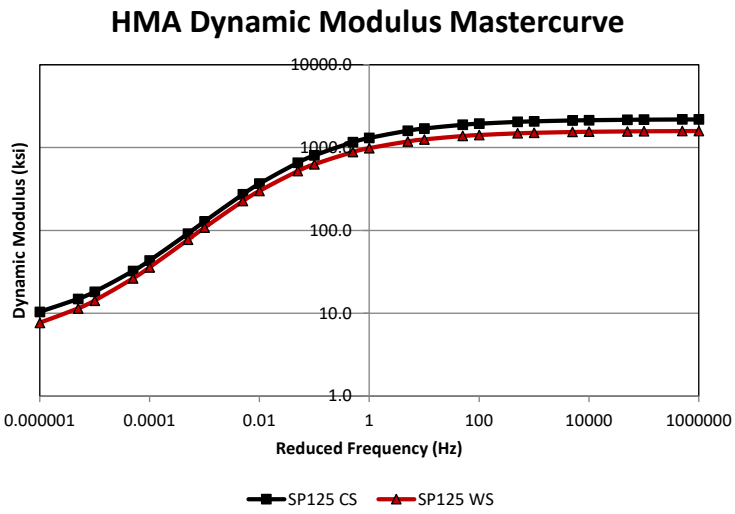

Figure 4-105. Dynamic Modulus Master Curves for the Bottom Lift of SR 79 AC (SP 12.5) at a Reference Temperature of 50ºF

4.3. Aggregate Base Materials

The base materials sampled from each roadway were all non-plastic and primarily granular. One exception included a single sample from the center of the SR 26 worm section that contained a greater fraction of fines and was classified as a silt in accordance with AASHTO M 145, *Standard Specification for Classification of Soils and Soil-Aggregate Mixtures for Highway Construction Purposes*. No distinct difference was observed between base materials sampled from worm and control section groups. Base thicknesses ranged from 8.8 in to 17.2 in across the five roadways and are presented in Figure 4-106. Base classifications include subsets of A-1, A-2, and A-4 mixtures and are provided in Table 4-20. To enable a comparison of moisture content of the base materials at each site, the in-situ moisture content was subtracted from the optimum moisture content (OMC) determined for each base material. The difference between these quantities are plotted as the moisture content relative to OMC in Figure 4-107. Base materials sampled from SR 79 contained the highest moisture contents, up to 5.6% above OMC in the worm section. The average moisture content of base materials on the remaining sites ranged between -1.7 OMC to +1.0% OMC. No trend is apparent in the data that indicate base material or moisture condition is associated with the occurrence of worm distress.

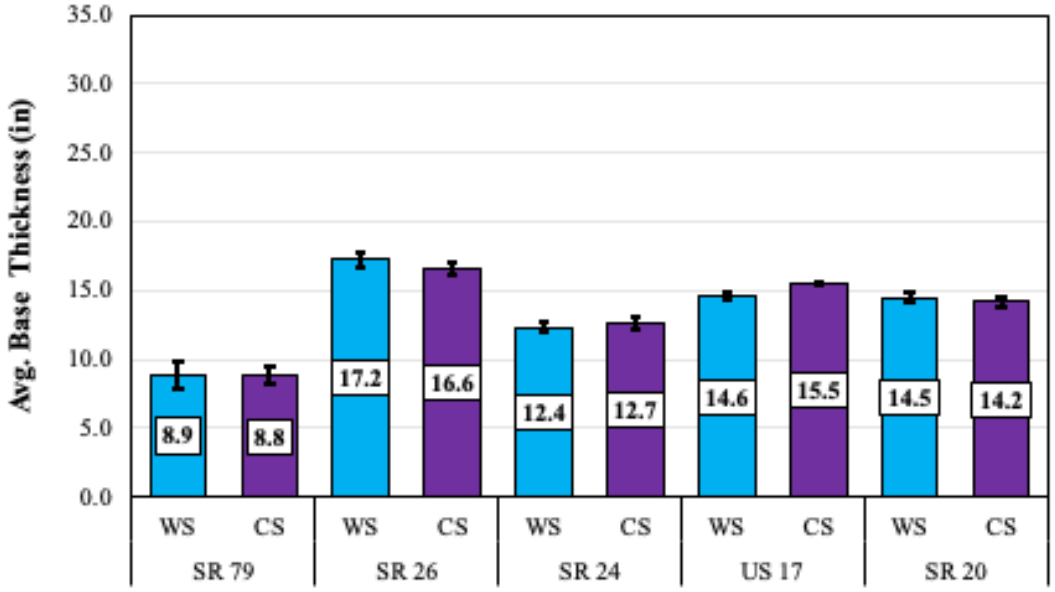

Figure 4-106. Average Base Thickness

Table 4-20. AASHTO Base Classifications

Section	Roadway				
	SR 79	SR 26	SR 24	US 17	SR 20
Control	A-2-4	A-2-4 & A-4	A-1-b	A-1-b	A-1-b
Worm	A-2-4	A-2-4	A-2-4	A-1-b & A-2-4	A-1-b & A-2-4

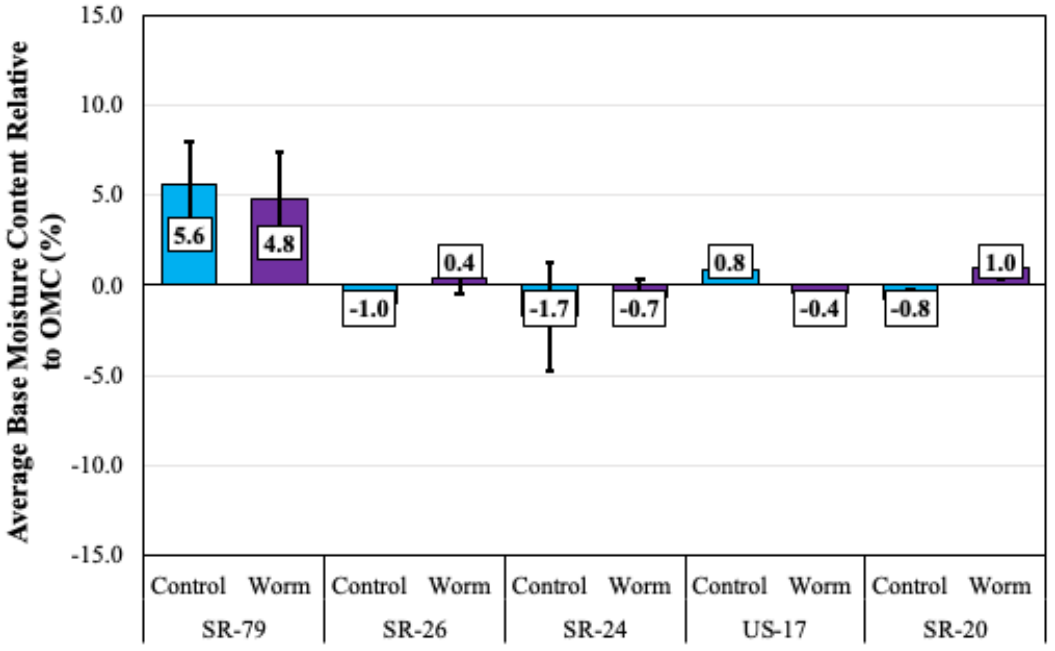

Figure 4-107. Base Course Moisture Content Relative to OMC

All base materials exhibited LBR above the 100 LBR minimum FDOT requirement for general use base course. Due to limitations of sampling through the 12-in core holes, an insufficient quantity of base was available from the SR 79 project for conducting individual LBR tests for both worm and control sections; therefore, worm and control materials were evaluated in a combined sample. SR 79 base course exhibited the lowest LBR of 114.0. SR 26 and SR 20 worm section base courses exhibited LBR values of approximately 40 to 50 percentage points greater than the respective control section; however, no distinct pattern in LBR was observed between the groups. Laboratory LBR results are presented in Figure 4-108.

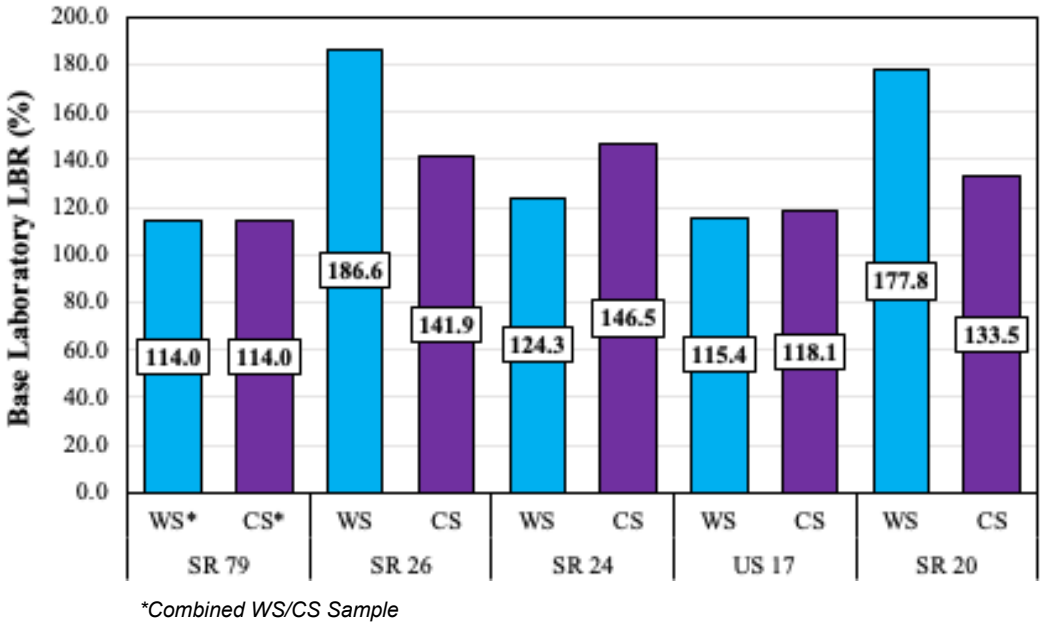

*Combined WS/CS Sample

Figure 4-108. Laboratory Base Course LBR Results

Maximum density of base course materials from the proctor test is presented in Figure 4-109. Insufficient materials were available from the 12-in core holes on the SR 79 project for conducting individual proctor tests from worm and control sections; therefore, worm and control materials were evaluated in a combined sample. The maximum density of all materials ranged from 112.5 pcf to 123.6 pcf. No distinguishable trend between maximum density is observed between worm distress and control groups.

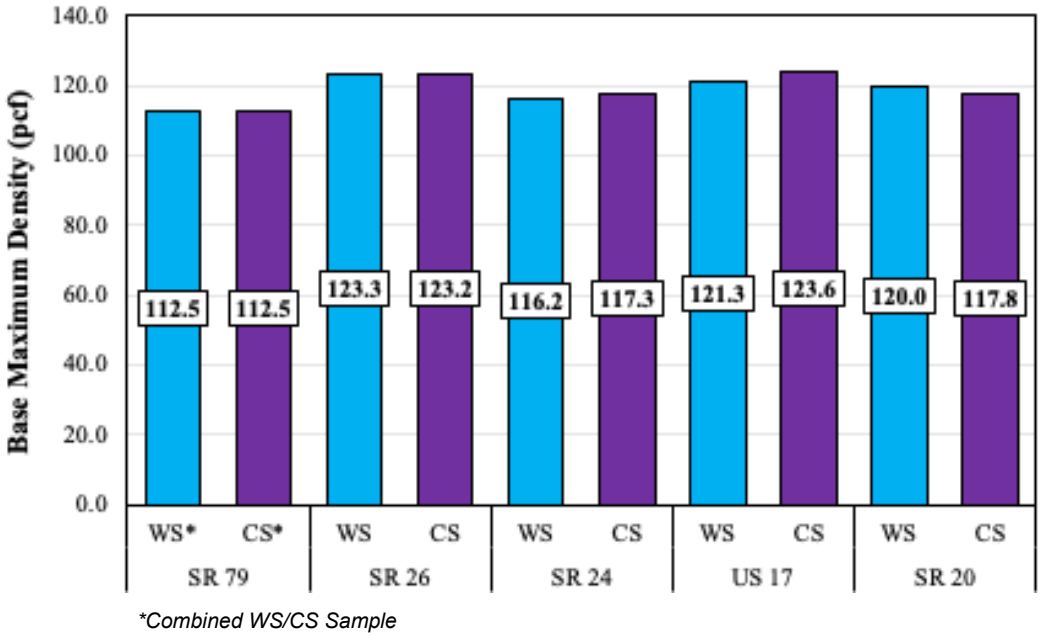

Figure 4-109. Laboratory Base Course Maximum Density Results

4.4. Subgrade Materials

The subgrade sampled from each roadway are typical A-3 and A-2-4 granular materials used in Florida. Classifications are provided in Table 4-21. The worm- and control-sampled subgrades shared the same classification(s) for four of the five roadways. The control section subgrade sampled from US 17 was consistently an A-2-4. Subgrade sampled on the south side of the worm section (A-3) contained a slightly larger fraction of sand. The remainder of the worm section subgrade was consistent with the control section subgrade.

Subgrade thicknesses for the subject projects are presented in Figure 4-110. Four of the five roadways included subgrades with layer thicknesses ranging between 22.6 and 32.9 in. The subgrade layer beneath SR 79 was approximately half the thickness of the other sites. SR 79 was also the only site with subgrade moisture above OMC. Moisture content relative to OMC is shown in Figure 4-112. Base materials sampled from SR 79 contained the highest moisture contents, up to 5.6% above OMC in the worm section. The average moisture content of the subgrade layers ranged between -5.0 OMC to +8.9% OMC. The average subgrade moisture content was greater in the worm section for three of the sites but not consistent for all roadways.

Maximum density of subgrade materials from the proctor test is presented in Figure 4-112 and range from 107.0 pcf to 120.6 pcf. No distinguishable trend between maximum density was observed between groups.

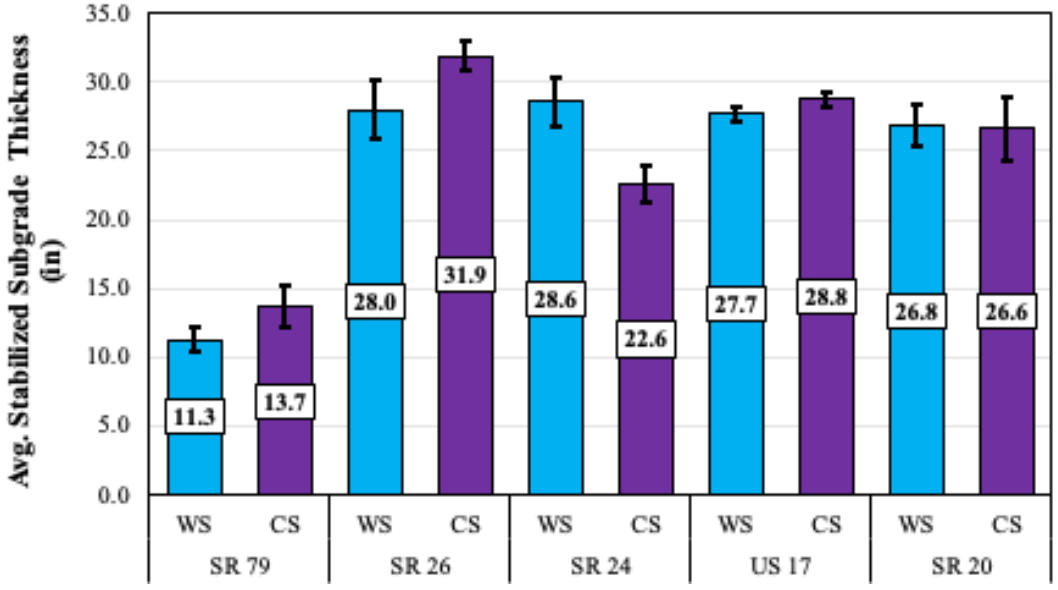

Figure 4-110. Average Stabilized Subgrade Thickness

Table 4-21. AASHTO Subgrade Classifications

Section	Roadway				
	SR 79	SR 26	SR 24	US 17	SR 20
Control	A-2-4	A-2-4	A-3 & A-2-4	A-3 & A-2-4	A-3 & A-2-4
Worm	A-2-4	A-2-4	A-3 & A-2-4	A-2-4	A-3 & A-2-4

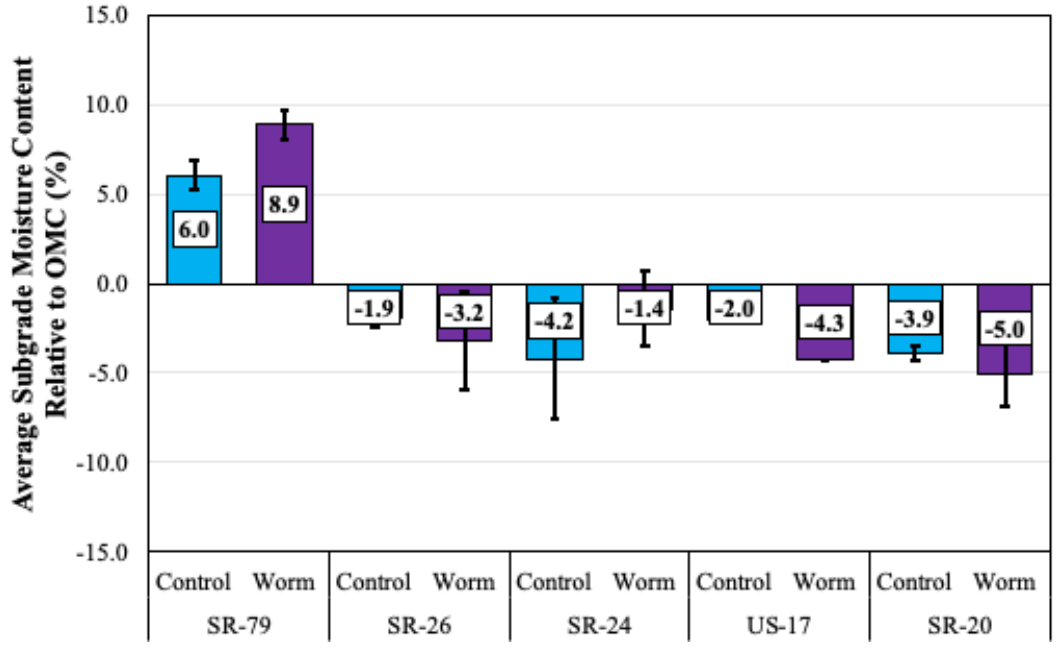

Figure 4-111. Subgrade Moisture Content Relative to OMC

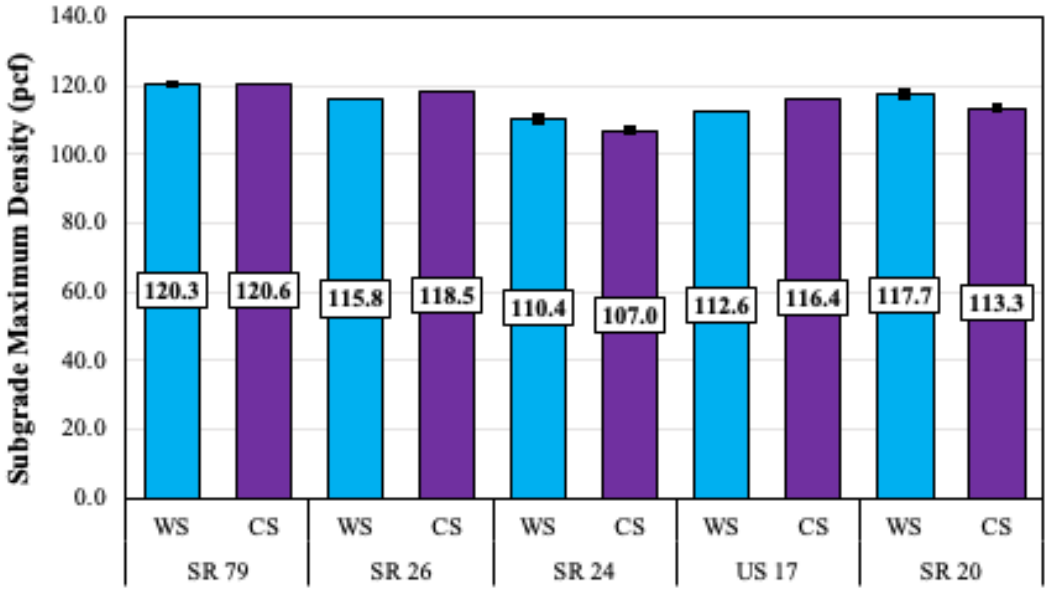

Figure 4-112. Laboratory Subgrade Maximum Density Results

4.5. Embankment Materials

The embankment materials sampled from each project were non-plastic silty and sandy soils. No distinct difference was observed between embankment sampled from worm and control section groups. Embankment classifications include subsets of A-3, A-2, and A-4 mixtures and are provided in Table 4-22. Moisture content relative to OMC in Figure 4-113. The embankment moisture was above OMC for three of the five projects. The moisture content of the embankment from worm sections was higher than the control sections for SR 79, SR 26, and US 17. No association between worm distress and embankment moisture is apparent from these data.

Maximum density of embankment materials from the proctor test are presented in Figure 4-114. The average maximum density of all materials ranged from 105.3 pcf to 119.3 pcf. No bias in the data was observed between worm and control groups.

Table 4-22. AASHTO Embankment Classifications

	Roadway				
Section	**SR 79**	**SR 26**	**SR 24**	**US 17**	**SR 20**
Control	A-2-4	A-2-4 & A-4	A-3	A-3 & A-2-4	A-3
Worm	A-2-4	A-2-4	A-3 & A-4	A-3 & A-2-4	A-3

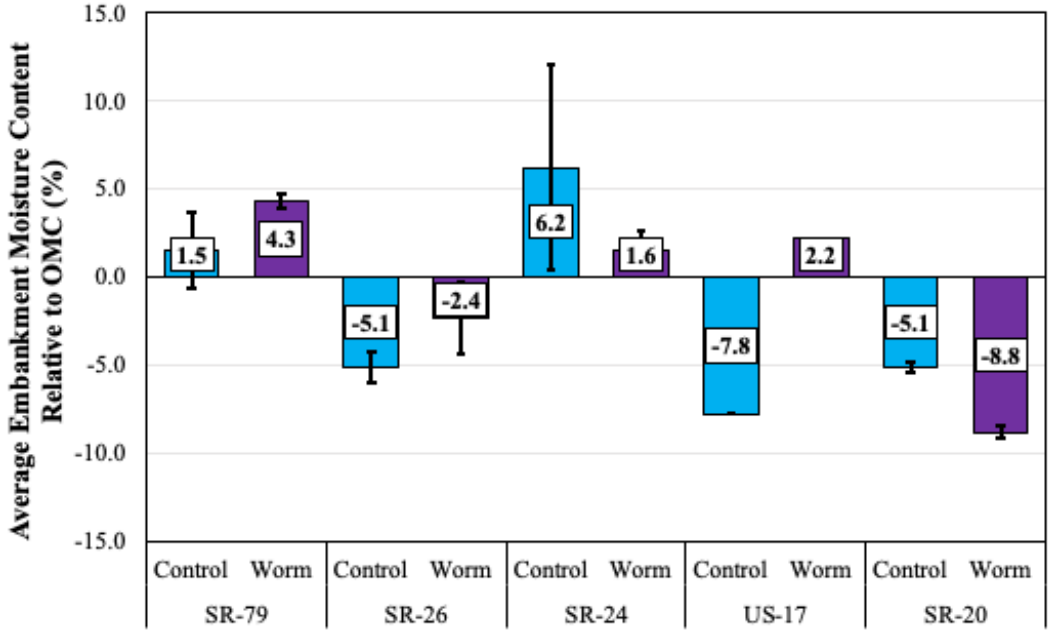

Figure 4-113. Embankment Moisture Content Relative to OMC

Figure 4-114. Laboratory Embankment Maximum Density Results

4.6. Pavement Service Life Analysis

Roque et al. [31] indicated that 90% of pavements scheduled for rehabilitation in Florida have been determined to be deficient based on crack rating. More importantly, the researchers pointed out that almost all of these pavements have failed due to top-down cracking, the major form of pavement distress in Florida. It is well understood that top-down cracking is initiated by tensile stresses and strains at the pavement surface, and the cracks propagate downward with repeated load applications. However, such understanding is only valid if all AC layers within the pavement structure are intact (i.e., fully bonded).

If the top lift/layer of AC is debonded from the lower layers, it is possible for cracks to initiate at the bottom of the top AC lift and propagate upwards. An illustration of tensile cracks due to debonding of the upper AC is shown in Figure 4-115 [32]. Since the top lift is relatively thin (typically 1.0 to 1.5 in), these cracks may appear at the pavement surface much sooner than the traditional bottom-up cracking from intact pavements. As such, these cracks are frequently categorized as top-down cracking by the time they become visible at the pavement surface.

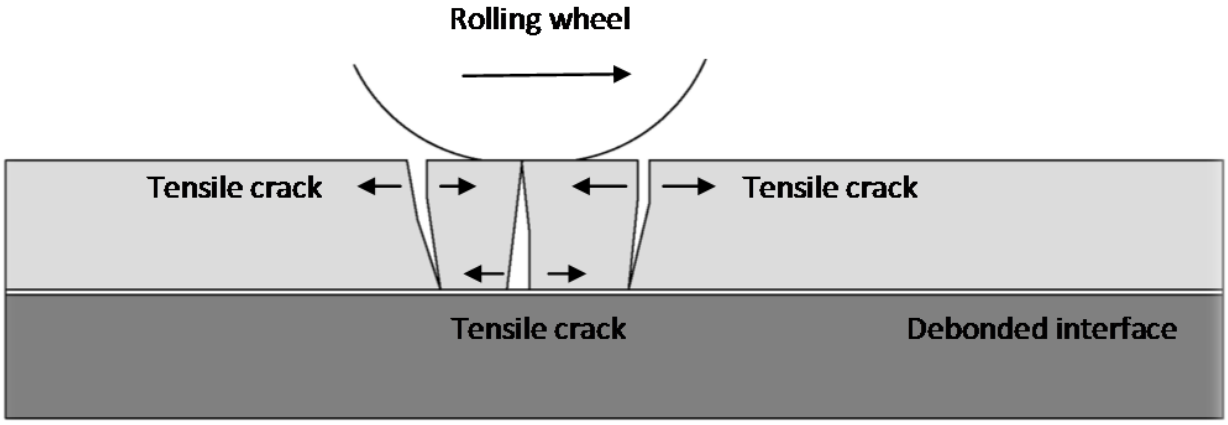

Figure 4-115. Illustration of Tensile Cracks in the Debonded Surface Layer [32]

In reference to the above discussion, the following four different crack initiation and propagation mechanisms were considered in this study:

1. Cracks starting from the pavement surface and propagating downwards (i.e., traditional top-down cracking).
2. Cracks starting at the debonded interface and propagating upwards.
3. Cracks starting at the debonded interface and propagating downwards.
4. Cracks starting at the bottom of the entire AC layer and propagating upwards (i.e., traditional bottom-up cracking).

In this study, the cracking models developed as part of the Mechanistic-Empirical Pavement Design Guide (MEPDG) methodology were used to study the effect of debonding [33]. The necessary procedure for cracking performance analysis is outlined below; note that the rutting performance can be evaluated in a similar manner.

FDOT has not fully implemented the MEPDG for asphalt pavements [34]; hence, local calibration factors for MEPDG flexible pavement models are not available. However, the MEPDG models with global calibration factors are sufficient to predict relative performance, i.e., development of distresses over time. Such an analysis can be refined by estimating site-specific calibration factors, provided the cracking history is available.

The MEPDG model [35] for the allowable number of axle load applications for both bottom-up (alligator) and top-down (longitudinal) cracking is:

$$N_f = 0.007566 \cdot 10^{M} \cdot C_H \cdot \left(\varepsilon_t\right)^{-3.9492} \cdot \left(E_{AC}\right)^{-1.281} \quad \textbf{(5)}$$

where N_f is the allowable number of axle load repetitions for flexible pavements, ε_t is the tensile strain at critical locations calculated using a structural response model, and E_{AC} is the dynamic modulus of asphalt measured in compression, pounds per square inch (psi). The terms M and C_H in the above equation are given as the following:

$$M = 4.84 \cdot \left(\frac{V_{be}}{V_a + V_{be}} - 0.69 \right) \quad (6)$$

$$C_H \begin{cases} = \dfrac{1}{0.000398 + \dfrac{0.003602}{1 + e^{(11.02 - 3.49 H_{AC})}}} & \text{(for bottom – up or alligator cracking)} \\ = \dfrac{1}{0.01 + \dfrac{12.00}{1 + e^{(15.676 - 2.8186 H_{AC})}}} & \text{(for top – down or longitudinal cracking)} \end{cases} \quad (7)$$

where V_{be} is the percent effective asphalt content by volume, V_a is the percent air voids in the asphalt mixture, and H_{AC} is the total asphalt thickness in inches.

The above MEPDG equations for cracking require strain inputs that must be calculated from a structural response model. The MEPDG uses a layered elastic analysis program, or more specifically, the Jacob Ozan Layered Elastic Analysis (JULEA) for calculating the pavement responses. However, JULEA (and hence the MEPDG) model is limited to simulating fully bonded or fully debonded layers and does not allow for simulating any partial bond that may be observed in the field. Therefore, to study the effect of varying levels of bond, ViscoWave software was used for simulating the structural responses in this study.

The same pavement structures used for FWD backcalculation (see Section 4.1.3) were used for simulating the pavement response under a moving load with ViscoWave. The load was modeled as a single tire with 9,000 lbs uniformly distributed over a circular, 8-in diameter contact area. The speed of the moving load was fixed at 50 mph. As an example of the ViscoWave simulation results, Figure 4-116 shows the pavement deflection simulated at the bottom of SR 24 AC. Similarly, Figure 4-117, Figure 4-118, and Figure 4-119 show the longitudinal, transverse, and vertical strains simulated at the bottom of the AC layer, respectively. Clearly, these figures show that the lower AC modulus and the lower bond modulus in the worm section contributed to the increased pavement response (deflection and strains).

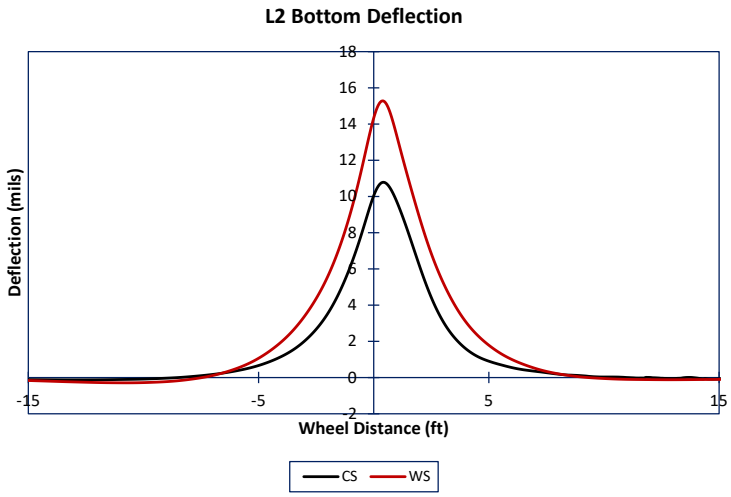

Figure 4-116. ViscoWave Simulated SR 24 Deflection at the Bottom of AC

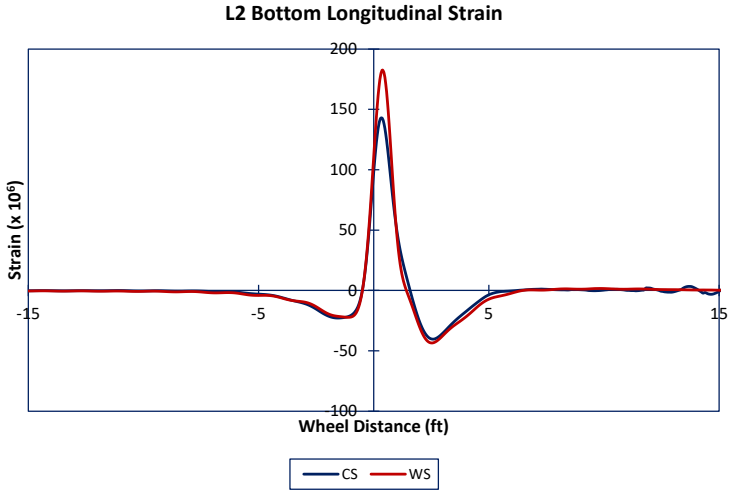

Figure 4-117. ViscoWave Simulated SR 24 Longitudinal Strain at the Bottom of AC

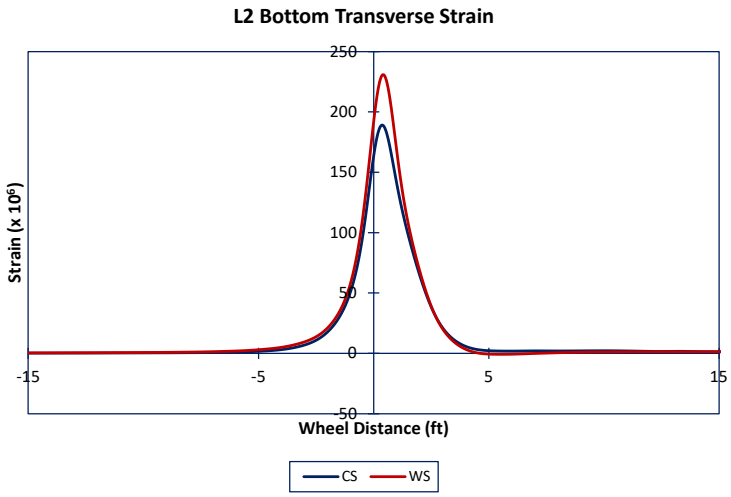

Figure 4-118. ViscoWave Simulated SR 24 Transverse Strain at the Bottom of AC

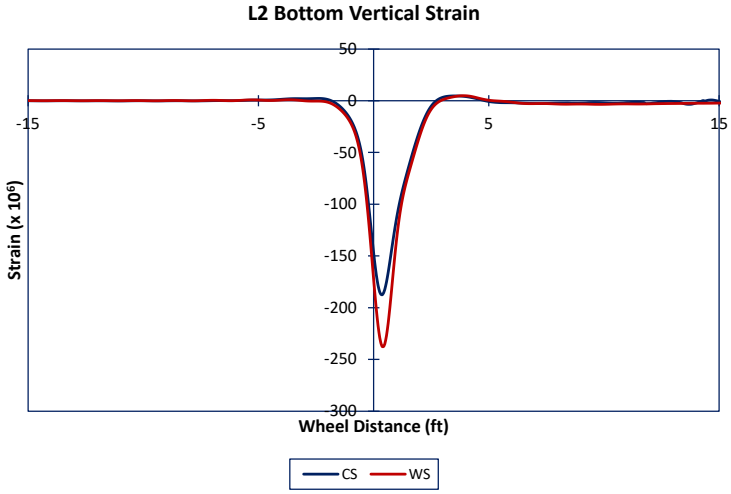

Figure 4-119. ViscoWave Simulated SR 24 Vertical Strain at the Bottom of AC

Using the MEPDG and ViscoWave models, the allowable number of axle load repetitions (N_f) were computed, as summarized in Table 4-23 for all four cracking mechanisms discussed above. The highlighted cells indicate the lowest N_f value obtained for a particular section. The table shows that the control section of SR 26 and both control and worm sections of SR 20 exhibit the lowest N_f values at the bottom of the top lift AC (i.e., cracks may initiate at the interface and propagate upwards). The remaining sections showed the lowest N_f values at the bottom of the bottom lift AC (i.e., cracks initiating at the bottom of the entire AC and propagating upwards). However, it should be emphasized that these N_f values were obtained using the global transfer function coefficients of MEPDG. In other words, the cracking model was not calibrated for Florida conditions. As such, these N_f values should only be used for relative comparison purposes.

Table 4-23. Summary of Allowable Number of Load Repetitions (× 10^6) for Cracking

Site	Section	Top Lift		Bottom Lift	
		Top	Bottom	Top	Bottom
SR 79	Control	749	51,883	165,952	5
	Worm	62	73,948	99,057	2
SR 24	Control	50,376	72,211	137,558	24
	Worm	21,502	2,195	13,185	10
SR 26	Control	571	238	288,036	259
	Worm	3,110	1,006,176	2,142	11
US 17	Control	218	119	364	16
	Worm	77	46	667	15
SR 20	Control	72	8	3,128	45
	Worm	13	2	3,472	144

As discussed, top-down cracking is the primary failure mode for Florida's pavements. As such, the minimum N_f values for the top lift were used for calculating the percent reduction [(N_f control – N_f worm)/(N_f control)] in pavement life. In addition, the percent life reduction was also calculated using the minimum N_f values from all four cracking modes (for comparison purposes). These results are summarized in Table 4-24.

Table 4-24. Summary of Predicted Cracking Life Reduction

Site	Section	Considering Top Lift Only		Considering Top and Bottom Lifts	
		Min. Nf (× 10^6)	% Life Reduction	Min. Nf (× 10^6)	% Life Reduction
SR 79	Control	749	91.7	5	60.0
	Worm	62		2	
SR 24	Control	50,376	57.3	24	58.3
	Worm	21,502		10	
SR 26	Control	571	-444.7	238	95.4
	Worm	3,110		11	
US 17	Control	218	64.7	16	6.3
	Worm	77		15	
SR 20	Control	72	81.9	8	75.0
	Worm	13		2	

The above table clearly shows that under top-down cracking, the worm sections generally show a significant life reduction ranging from 57% to 92%. The exception to this is SR 26, which showed higher N_f value for the worm section. Nevertheless, when all four cracking modes are considered, SR 26 also showed a 95% reduction in predicted pavement life, which was higher than any other sites.

To explain the extremely high N_f value of the SR 26 worm section top lift AC, it is noted again that SR 26 was the only site that the worm section exhibited a significantly higher modulus for

the bottom lift AC compared to the control section. Furthermore, the SR 26 worm section was the only section in which the top lift AC exhibited significantly lower (i.e., almost five times lower) modulus compared to the bottom lift (see Figure 4-38 and Figure 4-39). The outcome of such a drastic difference in AC modulus is that the bottom lift AC does not undergo a significant amount of "bending" and most of the strains occur within the weaker, top lift AC. As an example, Figure 4-120 and Figure 4-121 show the simulated vertical and transverse (i.e., horizontal) strains for the bottom of the SR 26 top lift AC. For all three strains, tension is positive and compression is negative in the charts. These figures clearly show that while the vertical, compressive strain increased significantly, the tensile strain almost diminished within the worm section (i.e., no bending).

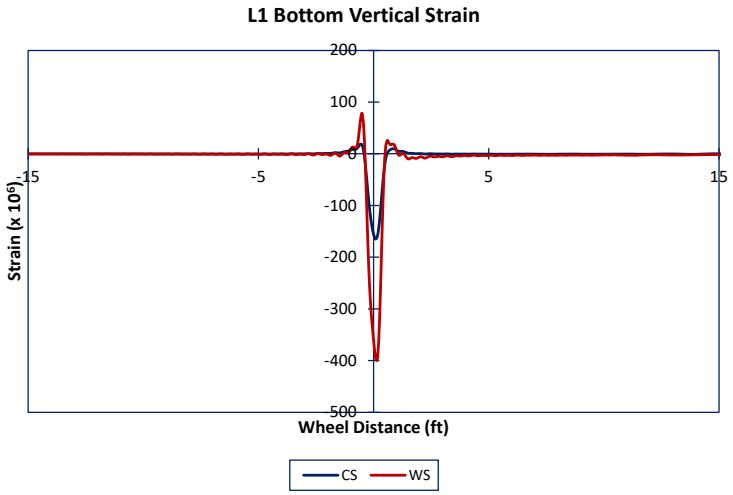

Figure 4-120. ViscoWave Simulated SR 26 Vertical Strain at Bottom of Top Lift AC

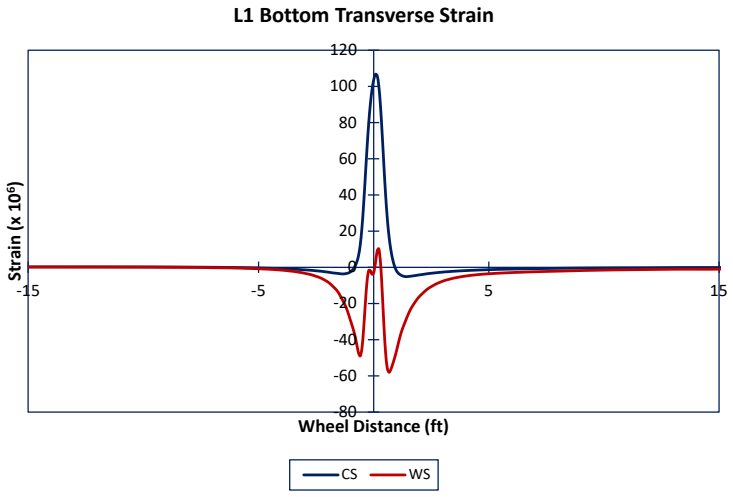

Figure 4-121. ViscoWave Simulated SR 26 Transverse Strain at Bottom of Top Lift AC

As seen from the above, the negligible amount of tensile strain observed within the top lift AC of the SR 26 worm section is responsible for the higher amount of N_f value shown in Table 4-24. On the other hand, it is believed that the increased vertical strain within the top lift AC may cause increased rutting within the AC layer. As such, the vertical strain at the mid-depth of each AC lift was simulated and the rut depth progression was predicted using the MEPDG methodology. Figure 4-122 and Figure 4-123 show, as an example, the predicted rut depth for the SR 26 control and worm sections, respectively. Figure 4-122 shows that the rutting within the control section is relatively minimal and most of the rutting is contributed to the bottom lift AC. Conversely, Figure 4-123 shows that the rut depth within the worm section grows relatively rapidly, and the rutting is mostly confined to the top lift AC (i.e., the weaker AC layer).

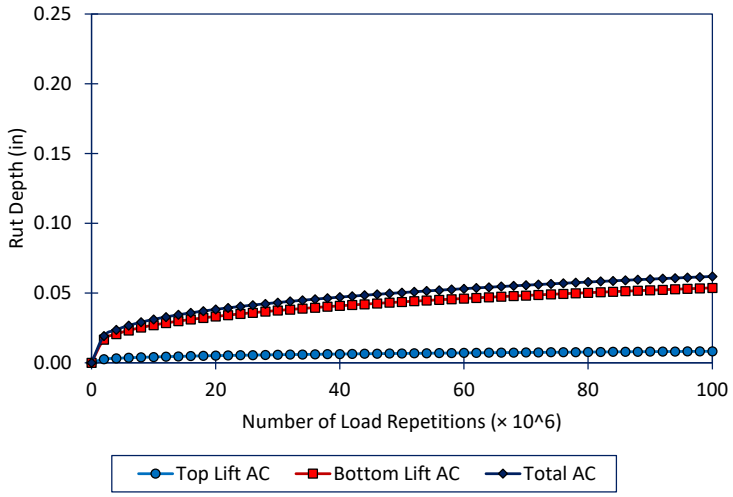

Figure 4-122. Rut Depth Predicted for SR 26 Control Section

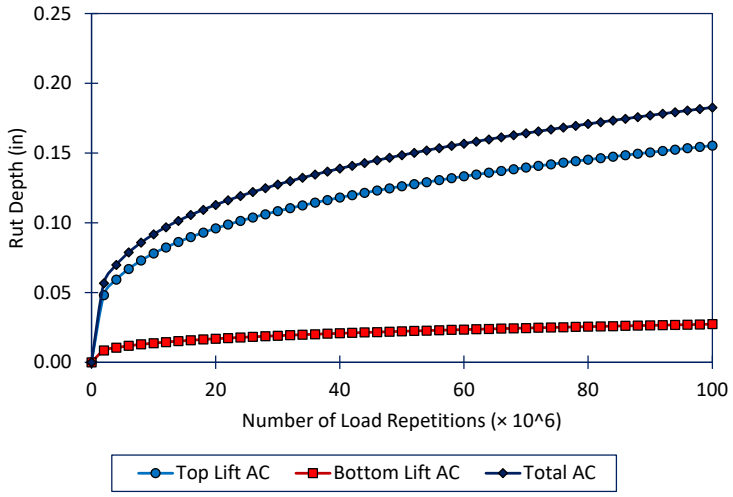

Figure 4-123. Rut Depth Predicted for SR 26 Worm Section

From the rut depth progression curves (such as those shown above), the pavement life under rutting was obtained for each of the sites. The rutting pavement life was defined as the number of load repetitions (N_f) until a total AC rut depth of 0.25 in is achieved. Table 4-25 summarizes these N_f values as well as the estimated life reduction for the worm sections.

Table 4-25. Summary of Predicted Rutting Life Reduction

Site	Section	Nf (× 10^6)	% Life Reduction
SR 79	Control	1,965	30.8
	Worm	1,359	
SR 24	Control	22,805	6.9
	Worm	21,221	
SR 26	Control	10,663	97.3
	Worm	286	
US 17	Control	17,946	58.8
	Worm	7,398	
SR 20	Control	6,811	10.0
	Worm	6,130	

The above table clearly shows that the worm distress may have a significant effect on pavement life based on rutting, which ranges from a 7% to 97% reduction. The most significant life reduction was observed from SR 26.

It should be noted that the above performance predictions for each section were carried out based on the backcalculated modulus values, with exception of SR 79 sections that used resilient modulus, from the respective pavement structure and without a calibrated set of transfer function coefficients. In other words, the uncertainties associated with the backcalculated modulus along with the lack of calibrated transfer function coefficients for Florida's conditions may cause significant differences between the predicted life (and its reduction) and the actual pavement life observed. Some discrepancies exist between the trend of predicted versus measured distresses. For example, field rutting is similar for SR 79 control and worm sections, but the prediction indicates the worm section has 30% life reduction. Field rutting is higher for the control section of SR 20, but the prediction indicates that the control section has better rutting performance. As such, it is recommended that the predicted pavement life and life reduction be used for relative comparison purposes.

5. SUMMARY OF FINDINGS

FDOT has experienced roadway worms, which become visible at the AC pavement surface as small bubbles or major bulges, for several decades. Several past studies indicated that the roadway worms (also referred to as ripples and blisters) generally occur when moisture or other gas-forming substances trapped in between the two lifts of AC layer. This moisture or gas may vaporize and expand in volume under a hot environment. Nevertheless, no literature was identified that examined the effect of roadway worms on cracking and rutting pavement performance and service life.

The primary objectives of this study were to identify the causes and contributing factors of roadway worms and to assess the impact of the worm distress on pavement performance. To accomplish these objectives, field and laboratory investigations were conducted on five roadway sections that exhibited the particular distress. At each section, a test area containing representative worm distresses was selected for study along with an adjacent section of the same age, same construction, and same traffic but with no worm distresses. The investigations included field tests and observations, sampling of pavement layers, and laboratory tests on the samples. A summary of key findings is presented below.

1. Careful inspection of the field-retrieved cores generally indicated that the presence of the roadway worms is associated with deterioration within the AC layers and at the interface of the upper two AC lifts. The deterioration of AC was more pronounced for the upper dense-graded AC layer and included segregation, excessive air voids, and debonding of the adjacent AC layers, as confirmed by laboratory test results. Delamination between the top DGA lift and underlying layer was observed in the AC field cores collected from each roadway. The cores collected from pavements with worm distress exhibited both (1) a greater occurrence of delamination and (2) air voids concentrated at the bottom of the uppermost DGA layer and/or the top of the second uppermost DGA layer. In cores exhibiting a more advanced state of deterioration, the air voids develop into deeper pitting where binder is stripped away from aggregate along the interlayer.
2. The laboratory shear test results conducted on the field cores indicated that the worm sections generally exhibited lower bond strength, although the actual strength and the degree of bond deterioration varied substantially between projects and within each project. Furthermore, many of the field cores (41%) tested for bond shear did not produce any useful results due to crumbling and failing within the AC mixture itself (rather than the interface), indicating severe loss of durability, stiffness, and strength of the AC materials. Significant degradation in AC modulus due to the worm distress was also confirmed by the backcalculated dynamic modulus from field FWD testing and laboratory resilient modulus testing. Based on the bond test results, the worm sections exhibited weaker bond strength than control sections. Visual inspection of the AC layer interfaces indicate (1) erosion of tack coat and (2) stripping of asphalt binder due to the presence of water between the top two DGA layers in the pavement structure. It is possible the decreased bond may be a result of worm distress and not a cause. This is difficult to discern without bond strength data before the worm distress occurs.
3. The AC field cores exhibited air void contents that are significantly higher than the typical target air void content of a dense-graded mixture. The higher air voids were observed in both the control and the worm-distressed sections of all five field sites studied. Air void content is likely greater along the friction/binder course interface where deterioration was observed in core samples. Permeability test results indicate the subject dense-graded

AC mixtures are generally impermeable, even with high air void contents. Localized air voids in the fine-graded mixtures are not interconnected. Overall, the permeability findings are not generalizable to suggest highly permeable layers in the AC structure are a prerequisite for worm distress.

4. Laboratory characterization of the unbound roadway layers showed general uniformity between base, subgrade, and embankment materials sampled from worm and control sections, indicating the cause of worm distress is not from the roadway foundation for the subject sites. One of the five sites investigated (SR 79) exhibited saturation in each support layer; however, moisture contents in the remaining four sites were quite variable and did not exhibit any pattern as related to the worms. Similar materials with different in-situ properties or elevations could result in different results.

5. The PaveScan GPR results generally showed that the dielectrics of the worm-distressed pavement surface exhibited significantly higher variability. While these results alone are inconclusive, they do relate to lower density or higher air voids of the AC layer which may allow intrusion of moisture into the pavement.

6. Backcalculation of FWD data as well as laboratory resilient modulus testing of AC cores indicated that the worm sections resulted in a significantly lower AC modulus compared to the control sections. Although the modulus degradation was more pronounced for the top lift, it was observed in both the top and the bottom lift AC, with the modulus reduction ranging from 16% to 72% (based on the dynamic modulus obtained at 10 Hz and at 50 ºF). In addition, simulation of pavement response and performance showed that the worm-distressed sections exhibit an increased level of pavement response (i.e., deflections and strains). The increase in pavement response, combined with reduced modulus, resulted in a significant reduction in predicted pavement life. More specifically when top-down cracking (which is the primary failure mode for Florida's pavements) was considered, the predicted life reduction ranged from 57% to 92%. Although rutting is not the primary failure mode, it was also found that worm distress may significantly affect the rutting performance of Florida's pavements. The reduction in pavement life due to rutting was estimated to be between 7% and 97%.

6. CONCLUSIONS AND RECOMMENDATIONS

The research discussed herein answers each of the stated objectives as provided below.

6.1. Determine Contributing Cause(s) for Roadway Worms

The field and laboratory investigations, along with information found in the literature from other similar investigations, suggest the causes (and contributing factors) of the worm distresses may be:

1. Moisture entering the AC layer during construction and getting trapped within the material and/or at the layer interface. The trapped moisture may cause severe bulging, stripping, and a large increase in air voids within the AC layer (which once had adequate air void content). The sources of moisture may include the following:
    a. Paving on top of a wet pavement surface (although not completely wet or saturated). The existing moisture may get trapped within or in between impervious AC layers.
    b. Excess moisture on the compaction roller (i.e., the moisture is not necessarily trapped at the interface, but within the AC layer being compacted).
    c. Intrusion through cracks at the pavement surface and trapped due to further compaction of AC by the driving traffic (more pronounced for mixtures having high air void content or segregation).
    d. The use of excessively wet aggregate stockpiles or insufficient drying procedures during the production of hot-mix asphalt.
2. Construction on top of an AC layer that has already experienced worm distress, as evidenced by the excessive air void content observed on many of the AC lifts directly above the unbound layer.
    a. The increase in temperature within the bottom lift AC may not be as significant as the layer that is exposed to the sun. As such, it is speculated that the higher air voids observed in these lower layers could be due to the worms that occurred before they were overlaid by another lift of AC. The moisture trapped between the AC and unbound base may cause worms. It is also possible that the subject layers were originally constructed with low density, and the excessive air-void contents are not caused by worms.
    b. Once this layer has experienced worms and exhibits higher air voids, it provides more room to store moisture prior to being overlaid.

6.2. Identify the Impact on Pavement Lifespan of Roadway Worms

The findings from this study support the following impact worm distress may have on pavement life.

1. The consequences of worm distresses can be severe. Although the modulus degradation is more pronounced for the top lift, it was observed in both the top and the bottom lift AC, with the modulus reduction ranging from 16% to 72% (based on the dynamic modulus obtained at 10 Hz and at 50 ºF). Worm-affected pavements exhibit an increased level of pavement response, as evidenced by simulation of pavement response and performance. The increase in pavement response, combined with reduced

modulus, indicate a significant reduction in predicted pavement life (i.e., 62% to 92% reduction under top-down cracking mode).

6.3. Develop Rehabilitation Strategies to Prevent Roadway Worms from Occurring

The findings from this study support the following strategies for preventing the occurrence of worm distress during construction:

1. Prohibit AC paving over a wet substrate, including prime or tack material that has not sufficiently cured.
2. Follow best practices for limiting HMA aggregate stockpile moisture, such as constructing stockpiles on slopes and sampling a foot above ground. Consider exploring a moisture content check of produced mix.
3. Minimize the water output from compactor drum water spray systems during rolling to the minimum volume needed for preventing asphalt pick-up on the drum.
4. Ensure asphalt surfaces are free from dirt, dust, and other deleterious materials before applying tack materials.
5. Confirm tack materials are adequately cured before applying AC overlays. Employ best practices to obtain adequate densification of AC.

The findings presented in this study support the following strategies for rehabilitating pavements with worm distress:

1. The extents of worm distress on a project may be identifiable with a PaveScan GPR survey. Variability (i.e., standard deviation/COV) of dielectric constants collected continuously on the site may be consistent with worm distress.
2. Extract a minimum of 10 AC core samples from the affected pavement and inspect for delamination and air voids along the interface of dense-graded lifts. If possible, dry-cut cores and inspect core holes for evidence of water ingress from unbound layers. If delamination, pitting, or large voids are apparent in the AC; consider the following remediation procedures:
    a. Completely remove the affected layers by milling, then overlay the pavement.
    b. After a minimum of 6 weeks of no precipitation, roll the pavement during warm weather to promote re-bonding of the distorted, detached layer. Seal joints and cracks to prevent ingress of water that may lead to blistering or other distress modes. This could be followed by the application of a fog seal (where allowable).
    c. Localized patching of worm-distressed areas in cases where there is only a small occurrence of isolated worm distress. This may not be practical where ruptured blisters are plentiful.
3. If evidence indicates water is entering the pavement structure from the unbound layers:
    a. Improve drainage on the site, then mill and overlay worm-distressed areas. This could include field drain retrofits along the edges of the pavement or localized reconstruction with a more permeable, open-graded base and or subgrade tied into a subsurface drainage system.

The findings of this study do not support any recommended design changes.

7. REFERENCES

[1] J. H. Tenison and D. I. Hanson, "Pre-Overlay Treatment of Existing Pavements - A Synthesis of Highway Practice," NCHRP Synthesis 388 ed., National Cooperative Highway Research Program, Washington, D.C., 2009, p. 143.

[2] Florida Department of Transportation, "Highway Mileage Report: State Highway System," Transportation Statistics Office, Tallahassee, FL, 2017.

[3] M. Acott and C. Crawford, "Blistering in Asphalt Pavements: Causes & Cures," National Asphalt Pavement Association, Lanham, MD, 1987.

[4] J. S. Lai, "Investigation of Causes and Development of Solutions to Blistering of Asphalt Layers," Georgia Institute of Technology, Atlanta, GA, 1987.

[5] C. F. Potts, "Surface Distortion Investigation, Research Report 172," Florida Department of Transportation, Tallahassee, FL, 1972.

[6] G. M. H. Beijers, "Research to the Formation of Blisters Which Occur by Application of Waterproofing Layers on Concrete Bridges," in *Proceedings of the Association of Asphalt Paving Technologists*, New Orleans, LA, pp. 552-576 Vol. 45, 1976.

[7] F. Netterberg and R. A. Bennet, "Blistering and Cracking of Airport Runway Surfacing Due to Salt Crystallization," in Proceedings of *8th Conference on Asphalt Pavements for Southern Africa*, Sun City, South Africa, pp. 1-19, 2004.

[8] J. J. Emery, "New Uses of Metallurgical Slags," *Canadian Mining and Metallurgical Bulletin,* Canadian Insitute of Mining, Metallurgy and Petroleum, Westmount, QC, vol. 68, no. No. 764, pp. 60-68, 1975.

[9] J. J. Emery, "Steel Slag Utilization in Asphalt Mixes," Proceedings of Canada Technical Asphalt Association, *National Slag Association, MF 186-1,* pp.1-11, 1984.

[10] S. J. Burgess, "Action of microorganisms on petroleum-asphalt fractions," *Highway Research Board Bulletin 118, pp. 27-48,* 1956.

[11] J. O. Harris, R. M. Kline and C. F. Crumpton, "A Study of the Presence of Hydrocarbon Utilizing Bacteria at the Soil-Asphalt Interface of Kansas Highways," *Transactions of Kansas Academy of Sciences, Topeka, KS,* vol. 59, no. 4, pp. 459-499, 1956.

[12] R. W. Traxler, "Microbial Degradation of Asphalt," *Biotechnology and Bioengineering,* American Society for Microbology, Kansas City, MO, vol. IV, pp. 235-238, 1962.

[13] J. O. Harris, "Pipeline Protective Coating Materials as Growth Substrates for Soil Microorganisms," *Transactions of Kansas Academy of Science*, Kansas Academy of of Science, Topeka, KS, vol. 62, no. No. 1, pp. 42-46, 1959.

[14] T. K. Jones, "The Effect of Bacteria and Fungi on Asphalt," *Materials Protection,* vol. 4, no. 12, pp. 39-43, 1965.

[15] L. R. Brown and T. R. Darnell, "Factors Affecting the Microbial Deterioration of Asphalt Overlays," Mississippi State Highway Department, Jackson, MS, 1986.

[16] J. G. Croll, "A new hypothesis for the development of blisters in asphalt pavements," *International Journal of Pavement Engineering,* vol. 9, no. 1, pp. 59-67, 2008.

[17] M. Celaya, S. Nazarian, C. Rao and H. Von Quintus, "Delamination Detection of Asphalt Pavements with Nondestructive Testing Device," in *90th Annual Transportation Research Board Meeting*, Washington, D.C., 2011.

[18] P. Jaskula and D. Rys, "Effect of Interlayer Bonding Quality of Asphalt Layers on Pavement Performance," in *IOP Conference Series: Materials Science and Engineering, Volume 236*, Gdansk, Poland, 2017.

[19] M. H. Sutanto, Assessment of Bond Between Asphalt Layers (Ph.D. Thesis), Nottingham, UK: University of Nottingham, 2009.

[20] ASTM International, *Standard Test Method for Tensile Strength of Concrete Surfaces and Bond Strength or Tensile Strength of Concrete Repair and Overlay Materials by Direct Tension (Pull-off Method). ASTM C1583,* West Conshohocken, PA: ASTM International, 2013.

[21] C. C. Ferraro, "Investigation of Concrete Repair Materials," Florida Department of Transportation, Gainesville, FL, 2008.

[22] M. Celaya, D. Mejia, S. Ertem, S. Nazarian, C. Rao, H. Von Quintus and P. Shokouhi, "Evaluation of NDT Technologies to Assess Presence and Extent of Delamination of HMA Airfield Pavements, Volume I: Technical Report, Project 06-04," Airfield Asphalt Pavement Technology Program, Auburn, AL, 2010.

[23] H. P. Bell, "Operating the Portable Seismic Pavement Analyzer," U.S. Army Engineer Research and Development Center, Vicksburg, MS, 2006.

[24] R. Evans, M. Frost, M. Stonecliffe-Jones and N. Dixon, "A Review of Pavement Assessment Using Ground Penetrating Radar (GPR)," in *12th International Conference on Ground Penetrating Radar*, Birmingham, UK, 2008.

[25] C. Holzschuher, H. S. Lee and J. Greene, "Accuracy and Repeatability of Ground Penetrating Radar for Surface Layer Thickness Estimation of Florida Roadways," Florida Department of Transportation, Gainesville, Florida, 2007.

[26] L. F. Walubita, W. Liu and T. Scullion, "The Texas Perpetual Pavements: Experience Overview and the Way Forward," Texas Transportation Institute, College Station, Texas, 2010.

[27] B. Al Hakim, L. W. Cheung and R. J. Armitage, "Use of FWD Data for Prediction of Bonding Between Pavement Layers," *International Journal of Pavement Engineering,* vol. 1, no. 1, pp. 49-59, 1999.

[28] International, ASTM, "Standard Test Method for Use of the Dynamic Cone Penetrometer in Shallow Pavement Applications," ASTM International, West Conshohocken, PA, 2018.

[29] H. S. Lee, "ViscoWave - A New Solution for Viscoelastic Wave Propagation of Layered Structures Subjected to an Impact Load," *International Journal of Pavement Engineering,* vol. 15, no. 6, pp. 542-557, 2014.

[30] H. S. Lee and J. Kim, "Backcalculation of dynamic modulus from resilient modulus test data," *Canadian Journal of Civil Engineering,* vol. 38, no. 5, pp. 582-592, 2011.

[31] R. Roque, B. Birgisson, C. Drakos and B. Dietrich, "Development and Field Evaluation of Energy-Based Criteria for Top-Down Cracking Performance of Hot Mix Asphalt," *Journal of Association of Asphalt Paving Technologists,* vol. 73, 2004.

[32] Y. R. Kim, A. A. Tayebali, M. N. Guddati, A. Karshenas and S. H. Cho, "Surface Layer Bond Stresses and Strength," North Carolina Department of Transportation, Raleigh, N.C., 2015.

[33] L. T. Glover and J. Mallela, "Guidelines for Implementing NCHRP 1-37A M-E Design Procedures in Ohio: Volume 4 - MEPDG Models Validation & Recalibration," Ohio Department of Transportation, Columbus, Ohio, 2009.

[34] Office of Design, Pavement Management Section, *Flexible Pavement Design Manual,* Tallahassee, Florida: Florida Department of Transportation, 2018.

[35] ARA, Inc., ERES Division, *Guide for Mechanistic_Empirical Design of New and Rehabilitated Pavement Structures, Appendix II-1: Calibration of Fatigue Cracking Models for Flexible Pavements,* Washington, D.C.: National Cooperative Highway Research Program, 2004.